# DESIGN AND DEVELOPMENT OF MECHANICAL AMPLIFIER STRUCTURE FOR PIEZOELECTRIC HARVESTER IN HIGH FORCE ENVIRONMENT

LONG SU XIAN

FACULTY OF ENGINEERING
UNIVERSITI MALAYA
KUALA LUMPUR

2022

# DESIGN AND DEVELOPMENT OF MECHANICAL AMPLIFIER STRUCTURE FOR PIEZOELECTRIC HARVESTER IN HIGH FORCE ENVIRONMENT

## LONG SU XIAN

## THESIS SUBMITTED IN FULFILMENT OF THE REQUIREMENTS FOR THE DEGREE OF DOCTOR OF PHILOSOPHY

## FACULTY OF ENGINEERING
## UNIVERSITI MALAYA
## KUALA LUMPUR

## 2022

# UNIVERSITI MALAYA

## ORIGINAL LITERARY WORK DECLARATION

Name of Candidate: LONG SU XIAN

Registration/Matric No: 17156462/2 / KVA180064

Name of Degree: DOCTOR OF PHILOSOPHY

Title of Project Paper/Research Report/Dissertation/Thesis ("this Work"):

DESIGN AND DEVELOPMENT OF MECHANICAL AMPLIFIER STRUCTURE FOR PIEZOELECTRIC HARVESTER IN HIGH FORCE ENVIRONMENT

Field of Study: ENGINEERING DESIGN (MECHANICS AND METAL WORK)

I do solemnly and sincerely declare that:

(1) I am the sole author/writer of this Work;
(2) This Work is original;
(3) Any use of any work in which copyright exists was done by way of fair dealing and for permitted purposes and any excerpt or extract from, or reference to or reproduction of any copyright work has been disclosed expressly and sufficiently and the title of the Work and its authorship have been acknowledged in this Work;
(4) I do not have any actual knowledge nor do I ought reasonably to know that the making of this work constitutes an infringement of any copyright work;
(5) I hereby assign all and every rights in the copyright to this Work to the Universiti Malaya ("UM"), who henceforth shall be owner of the copyright in this Work and that any reproduction or use in any form or by any means whatsoever is prohibited without the written consent of UM having been first had and obtained;
(6) I am fully aware that if in the course of making this Work I have infringed any copyright whether intentionally or otherwise, I may be subject to legal action or any other action as may be determined by UM.

        Candidate's Signature                    Date    26.8.2022

Subscribed and solemnly declared before,

                                                Date    26.8.2022
        Witness's Signature
Name:
Designation:

**ABSTRACT**

In recent years, harvesting electrical energy from mechanical vibration by using piezoelectric material has become the main focus of many researchers in developing a sustainable energy harvester. This is useful for Wireless Sensor Network (WSN), where a replacement or replenishment of energy source, such as a battery is unpractical. From previous studies, the amount of energy generated by piezoelectric energy harvester (PEH) is very limited even in a high force environment. To solve this issue, a mechanical amplifier structure such as the Rectangular Cymbal structure is implemented to amplify the tensile loading force towards the piezoelectric. From the material strength perspective, this performance can be further enhanced by using a compressive-typed mechanical amplifier structure, as the compressive yield strength of piezoelectric material is 10 times higher than its tensile yield strength. In this study, a novel compressive Hull PEH is designed and developed. A coupled piezoelectric-circuit finite element model (CPC-FEM) is developed to evaluate the energy harvesting performance based on the power output and stress analysis. Parametric optimization has been carried out to further enhance the amplification effect and determine the relationship of each parameter on the power output. An improved FEA power output of 11.34 mW is obtained for the optimized Hull PEH under 1 kN of sinusoidal force at 2 Hz. It is 178% larger than the unoptimized Hull PEH and 308% larger than the benchmarking tensile-typed Rectangular Cymbal PEH. The developed Hull PEH has a volume power density of 1.817 kW/m$^3$. An analytical force amplification factor of 9.72 is proven based on the kinematic theorem and the deformation of the frame. In the experiment, it exhibits at least 5 times larger voltage output than the benchmark case and at least 14 times greater than the standalone piezoelectric plate under impact force from a range of 10 N to 1 kN, with less than 5.2% of deviation to the FEA result. A maximum peak power output of 7.16 W is produced across a 50 kΩ of optimum load resistance. It is 37.68 times higher than that of the

benchmark PEH under 1 kN of impact force. Meanwhile, 84.38% of energy conversion efficiency is achieved by the Hull PEH based on the average input and output energies. It shows a power output of 54 µW at 180 kΩ and 5.28 times higher voltage output than the Rectangular Cymbal structure under 10 N of sinusoidal force at 50 Hz. It has a slight deviation of 3.8% from the FEA result. Therefore, the reliability of the developed CPC-FEM has been proven. The Hull PEH is concluded to have better harvesting performance in both simulation and experiment despite the loading environment either in high or low force. Hence, a higher power output PEH with enhanced load capacity and amplification effect has been realized. It has a lower stress concentration and is more cost-effective than the benchmark case. The developed PEH holds great potential to act as a sustainable energy source for some microcontroller applications with an LTC-3588 energy harvesting circuit.


**Keywords**: Compressive Mechanical Amplifier Structure; Energy Harvesting Performance; Parametric Optimization; Piezoelectric Energy Harvester; Rectangular Cymbal Structure.

# ABSTRAK

Kebelakangan ini, penghasilan tenaga elektrik dari getaran mekanik dengan menggunakan bahan piezoelektrik telah menjadi tumpuan utama banyak penyelidik dalam mengembangkan penghasilan tenaga lestari. Kaedah ini amat sesuai untuk *Wireless Sensor Network* (WSN), di mana penggantian atau pengisian semula sumber tenaga seperti bateri adalah tidak praktikal. Daripada kajian dahulu, jumlah tenaga yang dihasilkan oleh penghasil tenaga piezoelektrik (PEH) sangat terhad walaupun dalam persekitaran kekuatan tinggi. Untuk menyelesaikan masalah ini, struktur penguat mekanikal seperti struktur *Rectangular Cymbal* dilaksanakan untuk menguatkan daya muat tegangan ke arah piezoelektrik. Dari perspektif kekuatan bahan, prestasi ini dapat dipertingkatkan lagi dengan menggunakan struktur penguat mekanik bertekanan mampatan, kerana kekuatan hasil mampatan bahan piezoelektrik adalah 10 kali lebih tinggi daripada kekuatan hasil tegangannya. Dalam kajian ini, *Hull* PEH telah dicadangkan dan direka. *Coupled piezoelectric-circuit finite element model* (CPC-FEM) telah digunakan untuk menilai prestasi penghasil tenaga berdasarkan output kuasa dan analisis tegasan. Pengoptimuman parametrik telah dijalankan untuk meningkatkan lagi kesan penguatan dan menentukan hubungan setiap parameter pada output kuasa. Output kuasa FEA yang dipertingkatkan sebanyak 11.34 mW telah diperolehi untuk *Hull* PEH yang dioptimumkan di bawah 1 kN daya sinusoidal pada 2 Hz. Ini adalah 178% lebih besar daripada *Hull* PEH yang tidak dioptimumkan dan 308% lebih besar daripada penanda aras *Rectangular Cymbal* PEH. *Hull* PEH yang dihasilkan mempunyai 1.817 kW/m$^3$ ketumpatan kuasa isipadu. Sebanyak 9.72 faktor penguatan daya telah dibuktikan berdasarkan teorem kinematik dan pengubahan bentuk. Dalam eksperimen, *Hull* PEH menujukkan sekurang-kurangnya 5 kali keluaran voltan lebih besar daripada bekas tanda aras dan sekurang-kurangnya 14 kali lebih besar daripada piezoelektrik kendiri di bawah daya hentaman dari julat 10 N hingga 1 kN, dengan kurang daripada 5.2% sisihan kepada

hasil FEA. 7.16 W output kuasa puncak maksimum telah dihasilkan merentasi 50 k$\Omega$ rintangan beban optimum. Output ini adalah 37.68 kali lebih tinggi daripada penanda aras PEH di bawah 1 kN daya hentaman. Sementara itu, 84.38% kecekapan penukaran tenaga telah dicapai oleh PEH Hull berdasarkan purata tenaga input dan output. *Hull* PEH juga menunjukkan keluaran kuasa sebanyak 54 µW pada 180 k$\Omega$ dan keluaran voltan sebanyak 5.28 kali lebih tinggi daripada struktur *Rectangular Cymbal* di bawah 10 N daya sinusoidal pada 50 Hz. Keputusan ini mempunyai sedikit sisihan sebanyak 3.8% daripada keputusan FEA. Oleh itu, kebolehpercayaan CPC-FEM yang dikembangkan telah terbukti. Kesimpulannya, *Hull* PEH mempunyai prestasi penghasial tenaga yang lebih baik dalam kedua-dua simulasi dan eksperimen sama ada dalam persekitaran pemuatan daya tinggi atau rendah. Oleh hal yang demikian, suatu PEH yang mempunyai keluaran kuasa yang lebih tinggi dengan kapasiti beban dan kesan penguatan yang dipertingkatkan telah direalisasikan. *Hull* PEH mempunyai kepekatan tekanan yang lebih rendah dan lebih kos efektif daripada kes penanda aras. *Hull* PEH yang dikembangkan mempunyai potensi besar untuk bertindak sebagai sumber tenaga mampan untuk beberapa aplikasi mikropengawal dengan litar penghasilan tenaga LTC-3588.


**Kata kunci**: Struktur Penguat Mekanikal Mampatan; Prestasi Penghasilan Tenaga; Pengoptimuman Parametrik; Penghasil Tenaga Piezoelektrik; Struktur *Rectangular Cymbal*.

# ACKNOWLEDGEMENTS

# TABLE OF CONTENTS

# LIST OF TABLES

## LIST OF SYMBOLS AND ABBREVIATIONS

**Symbols:**

$\Delta l_b$      Deformation of the linkage

$\Delta x_{pzt}$      Deformation of PZT plate in x-axis

$\Delta y_b$      Perpendicular deflection of the beam

$<$      Less than

$>$      More than

$A$      Surface area

$C$      Stiffness constant $(N/m^2)$

$C_p$      Capacitance of the PZT plate (F)

$D$      Charge displacement tensor

$d$      Piezoelectric strain constant (C/N)

$E$      External electric field

$e$      Piezoelectric stress constant $(C/m^2)$

$E$      Young's modulus

$E_{in}$      Input mechanical energy (J)

$E_{out}$      Output electrical energy (J)

$E_s$      Stored energy (J)

| | |
|---|---|
| $F$ | Force (N) |
| $f$ | Frequency (Hz) |
| $F_a$ | Axial force |
| $F_n$ | Normal force |
| $F_{tx}$ | Total tensile force |
| $F_x$ | Horizontal output force |
| $F_{xp}$ | Tensile force along $x$-axis |
| $F_y$ | Vertical input force |
| $g$ | Acceleration of gravity |
| $g_{3i}$ | Piezoelectric voltage constant of PZT |
| $G_{actual}$ | Actual displacement amplification ratio |
| $G_{ideal}$ | Ideal displacement amplification ratio |
| $h$ or $H$ | Cavity height |
| $I$ | Area moment of inertia |
| $i$ | Direction of the stress |
| $k$ | Electromechanical coupling factor |
| k | Kilo |
| $ķ$ | Stiffness |

| $k_{amp}$ | Force amplification ratio |
|---|---|
| $K_l$ | Translational stiffness |
| $K_\theta$ | Bending stiffness |
| $l$ | Length |
| $l_b$ | Linkage length |
| $l_e$ | Extended base length |
| $l_h$ | Horizontal linkage length |
| $l_j$ | Joint length |
| $l_p$ or $l_{PZT}$ | PZT length |
| $l_s$ | Base length |
| M | Mega |
| m | Milli |
| $m$ | Polarization direction |
| $M_z$ | Moment equilibrium |
| $\eta$ | Force transmission coefficient |
| $\acute{N}$ | Total force amplification ratio |
| Ø | Diameter |
| $Ø_c$ | Cavity diameter |

| $P$ | Output power (W) |
|---|---|
| p | Pico |
| $P_3$ | Polarisation in z-axis |
| $P_{avg}$ | Average power |
| $Q$ | Accumulated charge on the electrode |
| $Q_s$ | Electric charge in short circuit condition |
| R | Load resistance ($\Omega$) |
| $r$ | Localized length function for the beam |
| $R_{amp}$ | Displacement amplification ratio |
| $R_{opt}$ | Optimal load resistance ($\Omega$) |
| $s$ | Displacement |
| $S$ | Elastic constant (m$^2$/N) |
| S/s | Sample per second |
| $T$ | Period (s) |
| $t$ | Thickness |
| $T_i$ | Stress tensor |
| $t_b$ | Linkage thickness |
| $t_p$ or $t_{PZT}$ | PZT thickness |

| $t_s$ | Base thickness |
|---|---|
| $U$ | Total converted electric energy (J) |
| $U_E$ | Electrical energy stored (J) |
| $V_3$ | Voltage caused by the polarisation change in z-direction (V) |
| $V_{oc}$ | Electric potential in open circuit condition (V) |
| $V_p$ | Peak voltage (V) |
| $V_{rms}$ | Root-mean-square voltage (V) |
| $w$ | Width |
| $W$ | Work done (J) |
| $\alpha$ | Amplification factor |
| $\varepsilon$ | Dielectric permittivity |
| $\varepsilon_0$ | Free space permittivity constant |
| $\varepsilon_{33}$ | Relative permittivity constant |
| $\varepsilon_{33}^T$ | Relative dielectric constant in z-direction |
| $\varepsilon^S$ | Clamp dielectric constant |
| $\varepsilon^T$ | Free dielectric constant |
| $\theta$ | Internal angle (°) |
| $\lambda_{max}$ | Energy transmission coefficient |

μ          Micro

$\rho$         Density (kg/m$^3$)

$\sigma$         Loaded stress (Pa)

η         Energy conversion efficiency

ξ         Dummy variable

**Abbreviations:**

AC                Alternative current

Al                 Aluminium

APDL            ANSYS Parametric Design Language

CANDLE        CANtilever Driving Low frequency Energy harvester

COPMS         Curved Outer Piezoelectric Multilayer Stack

CPC-FEM      Coupled piezoelectric-circuit finite element model

Cu                Copper

DAQ             Data Acquisition

DC                Direct current

DOF              Degree-of-freedom

FEA              Finite element analysis

HYBATS        Hybrid actuation/transduction system

HYPEHT       Hybrid Piezoelectric Energy Harvesting Transducer

IC                 Integrated circuit

IoT                Internet of Things

ISI                Institute for Scientific Information

LED              Light-emitting diode

| | |
|---|---|
| MEMS | Micro-electro-mechanic sensor |
| NASA | National Aeronautics and Space Administration |
| NI | National Instrument |
| PC | Personal computer |
| PEH | Piezoelectric energy harvester |
| PM | Primary magnets |
| PVDF | Polyvinylidene fluoride |
| PZT | Lead zirconate titanate |
| RAINBOW | Reduced and Internally Biased Oxide Wafer |
| SHM | Structural health monitoring |
| SIPMS | Straight Inner Piezoelectric Multilayer Stack |
| SL | Selectivity lever |
| SM | Secondary magnets |
| THUNDER | Thin Layer Unimorph Driver |
| Ti | Titanium |
| UVLO | Undervoltage lockout |
| WIM | Weight-in-motion |
| WSN | Wireless sensor network |

# CHAPTER 1: INTRODUCTION

## 1.1 Background Study

In recent years, harvesting energy from ambient energy sources such as solar energy, wind energy, and mechanical vibration energy has become a main, yet challenging focus of many researchers in developing a sustainable energy harvester; especially in those applications where a replacement or replenishment of energy source such as the battery is unpractical. For example, sensors that are deployed in remote places, inconveniently accessible places, or even inside the human body require a consistent energy supply from an ambient energy harvester (Sezer & Koç, 2021). The same goes for those electronic devices which are getting smaller physically as technology advances. To make it worst, the power consumption of the numerous electronic devices that are connected through the Internet of Things (IoT) has been increased tremendously, which increases the demand for a renewable energy source (Salazar, Serrano, & Abdelkefi, 2020). Among all the available energy sources, mechanical vibration energy is the most reliable energy source, as it is not affected by weather or environmental conditions, unlike other energy sources. The high force roadway with millions of vehicles passing on daily is a significant vibration source. Other examples of high force environments include railways, street floors, bridges, and shoes (L. Li, Xu, Liu, & Gao, 2018).

A piezoelectric harvester is believed to have great potential in harvesting useful electrical energy from mechanical vibration energy since it has high energy density, long lifetime, low cost, and small size. The generated electricity can be used to power up traffic lights, streetlamp posts, structural health monitoring system (SHM) systems, micro-electro-mechanic sensor (MEMS), and wireless sensor network (WSN) along the roadside or even in the industrial production line (Yang, Zhou, Zu, & Inman, 2018). However, a conventional piezoelectric energy harvester (PEH) has a low loading capacity which cannot withstand the excessive stress under a high force environment. Therefore,

a well-designed mechanical amplification structure is essential to protect the PEH from overloading as well as increase the power output. In short, high efficiency PEH with the additional design of mechanical amplification structure has a high potential to achieve a self-powered wireless sensing system. Hence, an environmental-friendly energy source is aimed to be realized to secure a green environment through this study.

## 1.2 Problem Statement

As mentioned in the background study, the development of a high performance PEH is essential to provide sufficient power for MEMS or WNS in remote places. Hence, to further improve the amount of harvested energy, the PEH is aimed to harvest energy from a high force mechanical vibration environment. However, the existing PEH design has low load capacity, leading to mechanical failure and low efficiency which cause it not suitable to implement in a high force environment (Zhao, Ling, & Yu, 2012). This is because most of the researchers focus on tensile-typed mechanical amplification structures such as Cymbal which converts the external compressive loading force acting on the harvester into internal tensile loading on the piezoelectric plate. In fact, piezoelectric material has a contrast strength property from metal where its compressive yield strength is much higher than its tensile yield strength. Hence, a tensile type of structure will not only limit its load capacity but also restrict the power output.

Many methods have been developed to compress the piezoelectric plate using the tensile-typed structure, such as opposing the direction of loading force (Feenstra, Granstrom, & Sodano, 2008), reallocating the location of piezoelectric (Xiaotian Li, Guo, & Dong, 2011), or applying multistage combination with two or more tensile-typed structure (T. B. Xu, 2016). To achieve this, the developed harvester will have a larger size which occupies more space and increase the installation difficulty. Therefore, there is a significant need to remain the external compressive force direction with magnified

loading amount acting on the piezoelectric plate. In recent years, some researchers try to develop a compressive-typed structure named as Flexcompressive structure for the application of shoe energy harvesters. But there are still some drawbacks of the current design, such as the limited loading area of the amplifier structure which will limit its application area. For example, the Flexcompressive structure is only suitable for small size devices and lower force environment which is below 1.5 kN (Matthew Evans, Tang, Tao, & Aw, 2019). Thus, a proper compressive mechanical amplification structure including the structural parameter has to be studied, designed, and developed for the PEH.

Other than the structural design, previous research (Feenstra et al., 2008; Feng Qian, Xu, & Zuo, 2019; Y. Wang, Chen, & Guzman, 2016) more focused on the experimental amplification factor of the PEH (i.e., in terms of power, voltage, and displacement), instead of the analytical force amplification factor of the mechanical amplifier structure. The experimental amplification factor is obtained by directly taking the output ratio between the PEH and a standalone PZT plate. Hence, lack of focus on the analytical modeling of the structure to predict the force amplification factor. The experiment must be carried out for both PEH and standalone PZT in order to know the amplification ratio, which is more time-consuming and costly. In fact, the analytical model of the structure could serve as a useful cross-reference to determine the performance of the proposed structure and ease the parametric optimization process.

Besides, another issue rises in the FEA performance optimization where previously the researchers only focus on the maximum design stress limit and the total strain energy transmission efficiency. There is a huge possibility that the PZT material has not been fully utilized and reduces the power output. This will lead to material wastage and low-efficiency issues for the PEH. On the other hand, the total strain energy transmission efficiency is not a comprehensive performance indicator of a PEH as it is not linearly

correlated with the power output. A new performance indicator should be proposed to solve this issue, such as by considering the PZT's average nodal stress.

## 1.3 Objectives

The objectives of this study are listed below:

1. To design a novel compressive mechanical amplifier structure (i.e., Hull structure) for a piezoelectric energy harvester (PEH) in a high force environment. Note that a compressive-typed structure could have a higher loading capacity to withstand a higher stress and overcome the drawbacks of the conventional designs.

2. To examine the effect of each structural parameter on the performance optimization of the PEH through Finite Element Analysis (FEA). Note that the performance optimization could boost the power output of the PEH by fully utilizing the PZT material, indicated by the higher value of PZT's average nodal stress.

3. To evaluate the energy harvesting performance of the proposed PEH in terms of power output, amplification effect, and efficiency under harmonic and impact loading forces by using FEA, analytical and experimental approaches. Note that the evaluation is important to validate the actual energy harvesting performance, force amplification factor, and experimental energy conversion efficiency of the proposed PEH.

4. To compare the performance of the proposed PEH with a benchmark tensile-typed PEH (i.e., Rectangular Cymbal structure) via FEA and experimental verification. Note that the proposed PEH has outstanding harvesting performance and more cost-effective than the conventional design under the same boundary conditions to serve as a sustainable power source.

**1.4     Scope of Study**

A deep study on the characteristics of the existing mechanical amplifier structure is important to understand their working principles. It helps in the concept generation of the novel compressive structure by analyzing and classifying the good feature to be implemented. Meanwhile, the vital structural parameter can be identified to ease the performance optimization process. Unlike the conventional PEH that aims at low force vibration source (i.e., <10 N), this study focuses on high force environments such as 1 kN of impact force to demonstrate the human foot strike or vehicular excitation.

An analytical model for the proposed structure is developed by considering the deformation of beam. A coupled piezoelectric-circuit finite element model (CPC-FEM) is developed to evaluate the Hull PEH based on the stress distribution and power output. A safety factor of 2 is implemented during the FEA stress analysis to ensure the durability and longevity of the developed structure. Therefore, with a high load capacity, mechanical failure such as cracking or fatigue issue can be avoided. This study also presents the experimental approaches to evaluate the energy harvesting performance of the proposed PEH using an impact hammer and permanent magnet shaker.

Among all the existing amplifier structures, a conventional tensile-typed Rectangular Cymbal structure is selected as the benchmark structure in this research since it has been well studied. Under the same boundary condition, a compressive structure with better energy harvesting performance is expected to be developed from this study. Since the developed structure has been compared with the benchmark structure, a high reliability research study can be proven by achieving the all the objectives.

**1.5     Thesis Outline**

The thesis presents a novel compressive mechanical amplifier structure for PEH with high efficiency and better energy harvesting performance under a high force environment. The

thesis is divided into five chapters, which begin with Chapter 1, the introduction to research background, problem statement, objectives, scope of study, and thesis outline.

Chapter 2 presents a comprehensive literature review that covers an overview of related studies regarding the piezoelectric energy harvesting techniques, especially on the various types of mechanical amplifier structures. Chapter 3 contains the research methodology starting from the background study, concept generation and selection of the novel structure, FEA modeling, fabrication of the prototype, and lastly the experiment. The development of CPC-FEM and experimental techniques are described in detail in this chapter. It includes the impact loading test and compression loading test used to examine the energy harvesting performance of the developed PEH.

Chapter 4 is the result and discussion that covers the findings from each sub-section of the research methodologies done. For instance, the concept generation on the novel amplifier structure, FEA parametric optimization, fabrication, and experimental result are discussed here. It consists of the validation of FEA results, an analytical model for the developed structure, experimental verification, and comparison of the energy harvesting performance with the existing PEHs. Lastly, the conclusion and novelty of the present work is drawn in Chapter 5 based on the research findings. Some recommendations for future work are summarized in this section.

**CHAPTER 2: LITERATURE REVIEW**

## 2.1    Introduction on Piezoelectric Transducer

There are three main categories of the transducer which are capable of converting mechanical vibration energy into electrical energy by utilizing different working principles, namely electromagnetic, electrostatic and piezoelectric transducer.

### 2.1.1    Electrostatic, Electromagnetic, and Piezoelectric Transducer

The working principle of an electrostatic transducer is based on the theory of attraction and repulsion of electric charges as shown in Figure 2.1 (a). It is generally constructed with three electrodes, where the middle electrode is free to move between the two outer static electrodes which are fixed in place. Through the built-in variable capacitor, electric charges can be generated from a relative movement between the moving and fixed electrodes. However, the electrostatic transducer has a very low capacitance and cannot convert mechanical energy to electrical energy directly for electret-free converters when compared with the other two types of transducers.

On the other hand, the working principle of an electromagnetic transducer is based on Lenz's law, where relative motion between a coil and a magnet is utilized in generating an electromagnetic induction as shown in Figure 2.1 (b). It is also named as a voice coil which is free to move in the uniform magnetic flux produced by the permanent magnet. Although it has been proven that this type of transducer has a longer lifetime than other types of transducers, it has a low output voltage and is less effective in low frequencies which causes it to be unsuitable to some applications.

Hence, to overcome all of these weaknesses, a piezoelectric transducer which contains the piezoelectric material, is capable to produce charges when it is deformed under applied stress, had been introduced as shown in Figure 2.1 (c). In 1880, Pierre and Jacques Curie had discovered the piezoelectric effect which can produce an electrical charge that

is proportional to the amount of externally applied force or vice versa. It has been revealed that the piezoelectric effect was shown when the built-in dipole of the crystal structure in the piezoelectric material started the polling process by cooling under the Curie temperature in a high electric field and then immediately removing the poling field. Thus, the dipoles are not able to return their original orientation and become permanently piezoelectric. The common well-known piezoelectric materials in the market are the ceramic type; such as Lead Zirconate Titanate (PZT) and polymer type; such as Polyvinylidene fluoride (PVDF) (Boisseau, Despesse, & Seddik, 2012).



| Electrostatic converters | Electromagnetic converters | Piezoelectric converters |
| --- | --- | --- |
| Use of a variable capacitor structure | Use of Lenz's law | Use of piezoelectric materials |

(a)       (b)       (c)
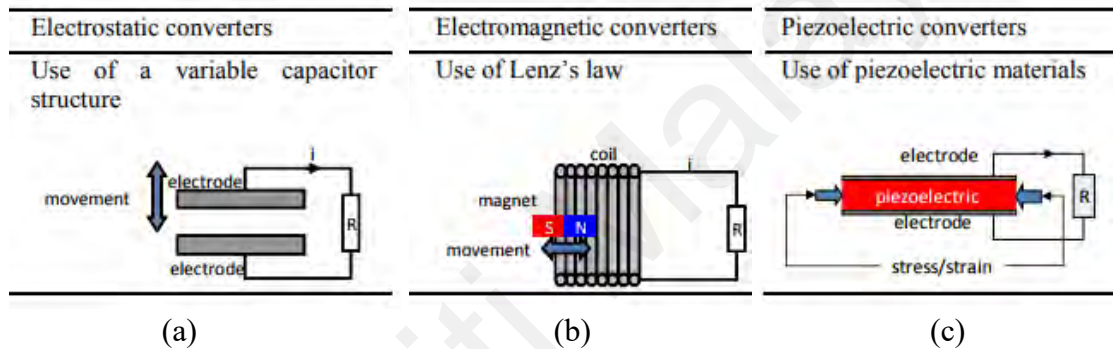
Figure 2.1 Comparison of the three main types of transducer (Boisseau et al., 2012)

A transducer can be further categorized into a sensor, actuator, or harvester based on its application. Among all these three types of transducers, piezoelectric transducers are more widely used and studied in the field of energy harvesting since it has higher capacitance, higher voltage output, and are more flexible to be integrated into a system. As a result, the piezoelectric harvester is chosen for the application in this study.

### 2.1.2 Material of Piezoelectric Plate

There are a few types of piezoelectric material available nowadays in the piezoelectric energy harvesting field, namely piezoelectric quartz, ceramic materials (i.e., PZT), and piezo film.

Quartz is not a pyroelectric where its properties depend directly on cutting orientation but are independent of variation on temperature. It has a comparatively high voltage

sensitivity but low charge sensitivity which is 100 times lower than the PZT values. The quartz has a linear response to the frequency as well (Mohammadi, 2013). On the other hand, the polyvinylidene fluoride (PVDF) membrane which is also known as the piezo film is a pyroelectric which can generate voltage due to a change of temperature, about 10 V/°C. It has a lower strain and dielectric constant than PZT ceramics, but it can generate 10 times higher voltage output than a PZT ceramic under the same loading force. However, PVDF is not selected for the application under a high force environment in this study due to its high fabrication cost (Kang & Cao, 2014).

Another frequently used piezoelectric material is the piezoelectric ceramic more well-known as lead zirconate titanate (PZT) which can change its dimensions in response to the applied voltage, or vice versa. It has a great capability of driving mechanical devices for precision positioning. It has very high piezoelectric coupling coefficients but relatively low maximum operating temperature at around 200°C. DL-53HD PZT (Del Piezo Specialities) was selected as the piezoelectric material for most of the study in the roadway energy harvesting field since it has a high figure of merit value ($2.64 \times 10^{-12}$), as suggested by literature (Daniels, Zhu, & Tiwari, 2013). The material properties of DL-53HD PZT which included its elastic stiffness constant, piezoelectric stress constant, and dielectric constant are all listed in Table 2.1.

Table 2.1 Material properties of DL-53HD PZT

| Parameters | | Symbols | Values |
|---|---|---|---|
| **Density (kg/m³)** | | $\rho$ | 7,900 |
| **Elastic Coefficient** | Stiffness constant (×10¹⁰ N/m²) | $C_{11}$ | 16.9 |
| | | $C_{12}$ | 11.8 |
| | | $C_{13}$ | 10.9 |
| | | $C_{33}$ | 12.3 |
| | | $C_{44}$ | 2.7 |
| | | $C_{55}$ | 2.7 |
| | | $C_{66}$ | 2.5 |
| | Elastic constant (×10⁻¹² m²/N) | $S_{11}$ | 15.1 |
| | | $S_{12}$ | -4.5 |
| | | $S_{13}$ | -9.4 |
| | | $S_{33}$ | 24.8 |
| | | $S_{44}$ | 37.1 |
| | | $S_{55}$ | 37.1 |
| | | $S_{66}$ | 39.2 |
| **Piezoelectric stress constant (C/m²)** | | $e_{31}$ | -12 |
| | | $e_{33}$ | 18.2 |
| | | $e_{15}$ | 21.9 |
| **Piezoelectric strain constant (×10⁻¹² C/N)** | | $d_{31}$ | -300 |
| | | $d_{33}$ | 680 |
| | | $d_{15}$ | 810 |
| **Dielectric permittivity** | Clamp dielectric constant, $\varepsilon^S$ (At constant strain) | $\varepsilon_{11}$ | 1,550 |
| | | $\varepsilon_{33}$ | 1,390 |
| | Free dielectric constant, $\varepsilon^T$ (At constant stress) | $\varepsilon_{11}$ | 3,550 |
| | | $\varepsilon_{33}$ | 3,850 |

### 2.1.3 Piezoelectric Effects

A direct piezoelectric effect is described as an electric field produced by applying mechanical stress on the piezoelectric, which is the fundamental used in the PEH. Conversely, the piezoelectric will deform when there is an external voltage applied on it which is named as the converse or inverse piezoelectric effect and applied in the actuator (Ueda, Schultz, & Asada, 2017). The general constitutive of direct and converse effects can be calculated as below (Zhao, Yu, & Ling, 2010).

Direct effect:
$$D_m = d_{mi}T_i + \varepsilon_{mk}^T E_k \qquad [2.1]$$

Converse effect:
$$S_i = s_{ij}^E T + d_{mi}E_m \qquad [2.2]$$

where $m, k$ = 1, 2, 3 (represents direction x, y, z); $i, j$ = 1, 2, 3, …, 6 (4, 5, 6 represents the shear about the x, y, z axes); $D$ = charge displacement tensor; $d$ = piezoelectric strain constant tensor; $T$ = stress tensor; $\varepsilon^T$ = permittivity/dielectric constant tensor measure at

constant $T$ condition; $E$ = external electric field; $S$ = strain tensor; $s^E$ = compliance tensor of PZT test at constant $E$ condition.

The direct piezoelectric effect is utilized in most energy harvesting applications, where there is no external electric field. The PEH can be designed in various modes which utilize the corresponding piezoelectric charge constant, $d_{mi}$ where '$m$' denotes the polarization direction of the piezoelectric layer, while '$i$' denotes the direction of the stress. For example, '1' is in the planar direction while '3' is perpendicular to the planar direction of the piezoelectric layers. Hence, 31 mode utilizes the $d_{31}$ piezoelectric charge constant, while 15 mode piezoelectric utilizes the shear effect. For 15 mode, the piezoelectric element is polarized in the axial direction and the induced electric field is perpendicular to the polarization in the thickness direction (J. Chen, Qiu, Han, & Lau, 2019; M′boungui, Adendorff, Naidoo, Jimoh, & Okojie, 2015). Normally, $d_{15} > d_{33} > d_{31}$ (Yang et al., 2018).

### 2.1.4 Piezoelectric Transducer's Evaluation Factors

There are several ways to evaluate the performance of a piezoelectric transducer, such as computing the force or displacement amplification factor of the amplifier structure based on the input and output ratio. Direct measurement of the open-circuit voltage or the power output across an optimum external load can be used to compare the PEH's performance. To ensure a fair comparison, power density either per unit PZT's volume or per device's volume has been proposed. Energy transmission efficiency, which is defined as the ratio of strain energy in the PZT materials and the total strain energy in the whole PEH, could be used as the evaluation factor as well (L. Wang, Chen, Zhou, Xu, & Zuo, 2016).

Besides, the electrical energy stored, $U_E$ in a PZT can be calculated with the open-circuit voltage and used as an evaluation factor. For PEH, the vertical force in the z-axis direction causes the polarisation, $P_3$ to occur on the surface of the PZT plate. Thus, equation [2.1] can be rewritten as shown in equation [2.3].

$$P_3 = \sum_{i=1}^{6} d_{3i} T_i \qquad [2.3]$$

where $P_3$ = piezoelectric polarisation at z-direction since it is equal to the charge density on the applied surface; $d_{3i}$ = piezoelectric constant; $T_i$ = stress tensor.

The internal electric field produced due to polarisation in PZT can be calculated as:

$$E_3 = \frac{P_3}{\varepsilon_{33}^T} = \sum_{i=1}^{6} g_{3i} T_i \qquad [2.4]$$

where $E_3$ = internal electric field in the PZT; $g_{3i}$ = piezoelectric voltage constant of PZT;

$\varepsilon_{33}^T$ = relative dielectric constant in z-direction.

The relationship between piezoelectric voltage coefficient, $g_{3i}$ and piezoelectric constant, $d_{3i}$ is given as:

$$g_{3i} = \frac{d_{3i}}{\varepsilon_0 \varepsilon_{33}^T} \qquad [2.5]$$

where $\varepsilon_o$ = dielectric constant of vacuum.

The stress tensor, $T_i$ on the PZT is because of the vertical force acting on it in the z-direction. Thus, the generated open circuit voltage on the PZT can be calculated from equation [2.3] and is shown in equation [2.6].

$$V_3 = \int E_3 dt_p = \sum_{i=1}^{6} \int g_{3i} T_i dt_p \qquad [2.6]$$

where $V_3$ = voltage caused by the polarisation change in z-direction, obtained via FEA;

$t_p$ = PZT thickness.

The output electric energy, $U_E$ and the total converted electric energy, $U$ of the PEH can be calculated as:

$$U_E = \frac{1}{2}P_3 E_3 A t_p = \frac{1}{2}V^2 \frac{\varepsilon_{33}^T \varepsilon_0 A}{t_p} \qquad [2.7]$$

$$U = \frac{1}{2}QV = \frac{1}{2}dg\sigma^2 A t_p \qquad [2.8]$$

where $A$ = surface area of the PZT plate; $Q$ = accumulated charge on the electrode; $d$ = current constant; $g$ = voltage constant; and $\sigma$ = loaded stress (Chua, Kok, & Goh, 2014).

The converted electric energy will increase with the product of $(d \cdot g)$ from equation [2.8]. Hence, another PEH's evaluation factor is the transduction rate of the PZT which is governed by the effective piezoelectric voltage and field constant, $g^{eff}$ and $d^{eff}$ (H. W. Kim et al., 2004).

Moreover, the performance of PEH can be evaluated by its ability to convert the mechanical energy to electric voltage energy through energy harvesting efficiency (or energy conversion efficiency), $\eta$. Equations [2.9] to [2.11] show the calculation for $\eta$, where $\eta$ is defined as the ratio between the harvested output electrical energy, $E_{out}$ and the input mechanical energy, $E_{in}$ (Cho et al., 2019; Covaci & Gontean, 2020; Yang, Erturk, & Zu, 2017). Zhao, Qin, and Ling (2015) had studied the efficiency by considering the electromechanical coupling factor, $k$ and the energy transmission coefficient, $\lambda_{max}$ of the Cymbal structure PEH for asphalt pavement energy harvesting application via FEA and the equations used are shown in equations [2.12] and [2.13].

$$\eta = \frac{Output\ electrical\ energy, E_{out}}{Input\ mechanical\ energy, E_{in}} \times 100\% \qquad [2.9]$$

$$E_{in} = \int_0^T F\ s(t)\ dt \qquad [2.10]$$

$$E_{out} = \int_0^T P\,dt = \int_0^T \frac{V_{rms}^2}{R}\,dt \qquad\qquad [2.11]$$

$$k^2 = \frac{Stored\ electrical\ energy}{Input\ mechanical\ energy} = \frac{U_E}{W} \qquad\qquad [2.12]$$

$$\lambda_{max} = \left(\frac{Output\ electrical\ energy}{Input\ mechanical\ energy}\right)_{max} = \frac{Q_s V_{oc}}{4W} \qquad\qquad [2.13]$$

where $F$ = applied force; $s$ = displacement; $T$ = period; $P$ = output power; $V_{rms}$ = root mean square of output voltage; $R$ = external load resistance; $W$ = work done by the external force in short circuit condition; $Q_s$ = electric charge in short circuit condition; $V_{oc}$ = electric potential in open circuit condition.

For applications such as energy harvesting from the roadway, it can be simulated by a routine, where the external force is loaded under the short circuit condition (i.e., Electric field, $E$ = 0); then the force is unloaded under the open circuit condition (i.e., Electric displacement, $D$ = 0).

However, the effective $k$ and $\lambda_{max}$ values are difficult to be calculated due to their complicity in the Cymbal-Pavement coupling system as reported by Zhao et al. (2015). Thus, another way to evaluate the harvester performance is by considering the electric energy storage in an open circuit, which is related to the energy conversion efficiency and electrical power. Meanwhile, a good coupling effect can be indicated by having the almost same surface displacement of the roadway with and without Cymbal. In short, the electric energy storage in an open circuit and surface displacement on the roadway can be used as the evaluating factors (Zhao et al., 2010).

## 2.1.5 Optimization Phase of Piezoelectric Transducer

The piezoelectric transducer, typically the PEH, converts the kinetic energy into electrical energy in three phases. Power enhancement can be done at each phase with particular approaches. The first stage is the mechanical-mechanical energy transfer process, which

14

is the transfer of the mechanical energy from a vibration source into piezoelectric material in the PEH. To improve the performance of the PEH, structural design with force amplification effects such as on the geometry, configuration, or parameter optimization can be developed.

For the next stage, the mechanical-electrical energy conversion process converts the mechanical energy into electrical energy in the piezoelectric element, where the selection of piezoelectric material is crucial. For instance, the PZT material with high piezoelectric strain constant $d$, high piezoelectric stress constant $g$, and high electromechanical coupling coefficient $k$ is always preferred to achieve high energy transduction rates.

The last stage would be the electrical-electrical transferring process, which is the extraction of electrical energy from piezoelectric material to outside of the PEH. In this process, impedance matching, circuit enhancement, and electrode optimization can be done to increase the energy extraction efficiency from the PEH (Xu, 2016; Yang et al., 2018).

### 2.1.6 Piezoelectric Transducer's Application

Over the years, many types of research regarding the application of a piezoelectric transducer in the energy harvesting field have been conducted (N. Wu, Bao, & Wang, 2021). However, only a few of them are focusing on the high force environment. The mechanical energy under the high force environment is mostly caused by the load or stress of the moving vehicle or human activities such as walking or running, which is a potential sustainable energy source to be explored further (Matthew Evans et al., 2019; Jasim, Wang, Yesner, Safari, & Maher, 2017; H. Zhao et al., 2012). Piezoelectric technology is believed to have the most potential in this field since a self-powered sensor by using the piezoelectric transducer had been suggested by Lin et al. (2013).  It has a wireless self-sustain power supply function in the transportation monitoring field.

### 2.1.6.1 Working mechanism of a piezoelectric transducer as a self-powered transportation monitoring sensor

Piezoelectric material not only can be utilized as an energy harvester but also to work as a sensor, such as a transportation monitoring sensor. The response of the voltage signal produced by PZT normally will reflect directly from the excitation force pattern. For example, unstable vibration sources such as the engine, motor, air-conditioning condenser, fluid flow including wave and wind turbine, will generate a random voltage signal. As a result, PZT is widely used as a pure energy harvester for these vibration sources, usually, it is integrated with Cantilever typed amplification structure. Differing from these vibration sources, vibration signal generated by vehicle or human walking comes in peak. Useful information, such as peak voltage value, time, date, period, etc, can be retrieved from the voltage signal produced by the PZT when there is stress applied on it. The piezoelectric transducer is aimed to provide a green energy source for the speed sensor and increase the efficiency of the weigh-in-motion (WIM) sensor. A series of study had been done by Lin et al. (2013) on the possibility of using a piezoelectric transducer (named as a nanogenerator, NG in the study) as a transportation monitoring sensor to detect vehicle speed and weight simultaneously.

### 2.1.6.2 Speed detecting mechanism

The NG has the same working principle as the piezoelectric energy transducer which is capable to transform the external force exerted by vehicles into useful electricity to power up the sensor itself. When a vehicle is passing by, an external force will be applied on the NG. As a result, the NG will deform and a piezoelectric potential difference will be generated due to induced charges as illustrated in Figure 2.2.
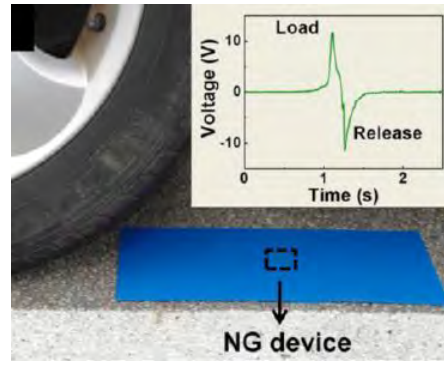
Figure 2.2 The peaks indicated the voltage generated when the vehicle tire passed
through the PZT transducer (Lin et al., 2013)

To detect the vehicle speed, two similar NGs are placed side by side in the direction
of the moving vehicle with a fixed distance of $\Delta s = 0.6$ m as tested by Lin et al. (2013)
along the roadway of a moving vehicle path as shown in Figure 2.3. When the front tire
of a vehicle rolled on the two sensors subsequently, two successive voltage peaks with
the time interval, $\Delta t$ can be recorded by the measurement system. By assuming that the
vehicle is moving with constant speed during this quick process, the instantaneous speed
of the vehicle, $V$ can be calculated simply as

$$V = \frac{\Delta s}{\Delta t}$$
[2.14]



Figure 2.3 Illustration of the working mechanism of a speed sensor
(Lin et al., 2013)

Two examples of vehicle's speed which is calculated from the data retrieved in voltage
against time graph are shown in Figure 2.4. From the settings done by Lin et al. (2013)
where the sampling rate = 500 s$^{-1}$ and the NGs' distance, $\Delta s = 0.6$ m, the detection limit
was equal to 300 m/s (1080 km/h). Hence, it is more than enough to detect the vehicle
speed even on the highway.
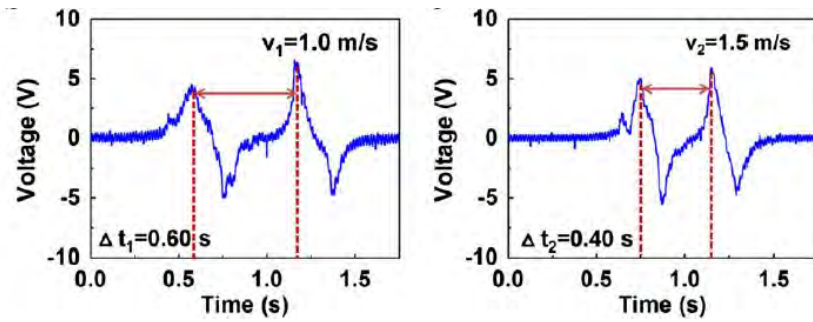
Figure 2.4 Two examples of speed calculated from the voltage against time graph by using two similar NGs (Lin et al., 2013)

### 2.1.6.3 Weight-in-motion detecting mechanism

Theoretically, the output voltage of the piezoelectric transducer is proportional to the stress applied onto the sensor. A study in determining the weight of a vehicle in motion using Quartz instead of PZT as the sensor material had been done and proven to be working successfully by Karim, Ibrahim, Saifizul, and Yamanaka (2014). The sensor was also proven to be capable of measuring the vehicle loads successfully without any structural failure (Karim et al., 2014). The weight detection system is shown in Figure 2.5. According to the results, there is a great potential of using the piezoelectric transducer as a self-powered sensor for monitoring the weight and speed of vehicles on the road at the same time. When compared with the traditional techniques for transportation monitoring, such as speed camera and electronic balance, the piezoelectric-based speed and weight sensor has the advantages, as it is a self-powered sensor that does not require any external power source.
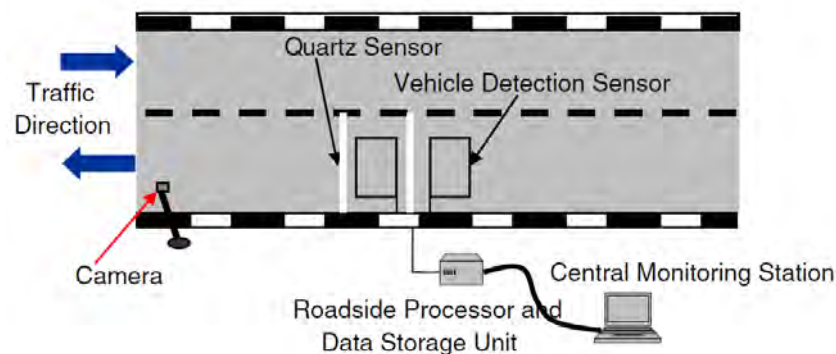


Figure 2.5 Weight monitoring system (Karim et al., 2014)

### 2.1.7    Summary

As the PZT has a lower cost and requires less maintenance, it will be studied further in this project. It is also believed that the piezoelectric transducer could serve as a reliable energy harvester on the roadway, which is capable to convert the mechanical energy from the moving vehicle into electrical energy that is more than enough to power up the sensor itself and some small electronic equipment along the roadway. Also, effective $k$ and $\lambda_{max}$ values can be used to evaluate the performance of PEH.

Geometry modification at the first stage with the development of a mechanical amplifier structure is the most directive way to manipulate the stress distribution, increase overall PZT's deformation, power output, and load capacity. Furthermore, there is room for improvement found in the design and development of mechanical amplifier structures, especially in compression mode. Hence, only the optimization via mechanical amplifier structure will be focused on in this study.

Since a high force environment that can up to thousands of Newtons per impact is focused on in this study, the piezoelectric transducer should be well-designed to prevent failure. Other than increasing the load capacity, the energy harvesting amplification factor has to be further magnified to achieve self-powered functionality. In short, a successful piezoelectric transducer for high force environment application should have high efficiency, low cost, and a long lifetime (Ling, Cao, Zeng, Lin, & Inman, 2016).

### 2.2    Various Types of Mechanical Structure in Piezoelectric Transducer

The mechanical amplifier structure, which is also known as amplification frame, is a structural design that enlarges the input loading to a much higher output force. Consequently, the PZT will deform more based on the amplification effect under larger stress, leading to higher power output. Hence, it is important to design a mechanical amplifier structure in order to amplify the load that is acting on a PZT plate within the

material stress limit (H. Zhao et al., 2012). Figure 2.6 shows several mechanical structures which can be generally classified into three main classes, namely a cantilever type, a flexure type, and a combination multistage type. The flexure type can be further divided into flextensional and flexcompressive types based on its deformation direction either away or towards the middle node. In this section, the characteristics and mechanisms of these three main classes of mechanical amplification structures will be discussed starting from 2000 to date, which includes the derivative structures in recent years.
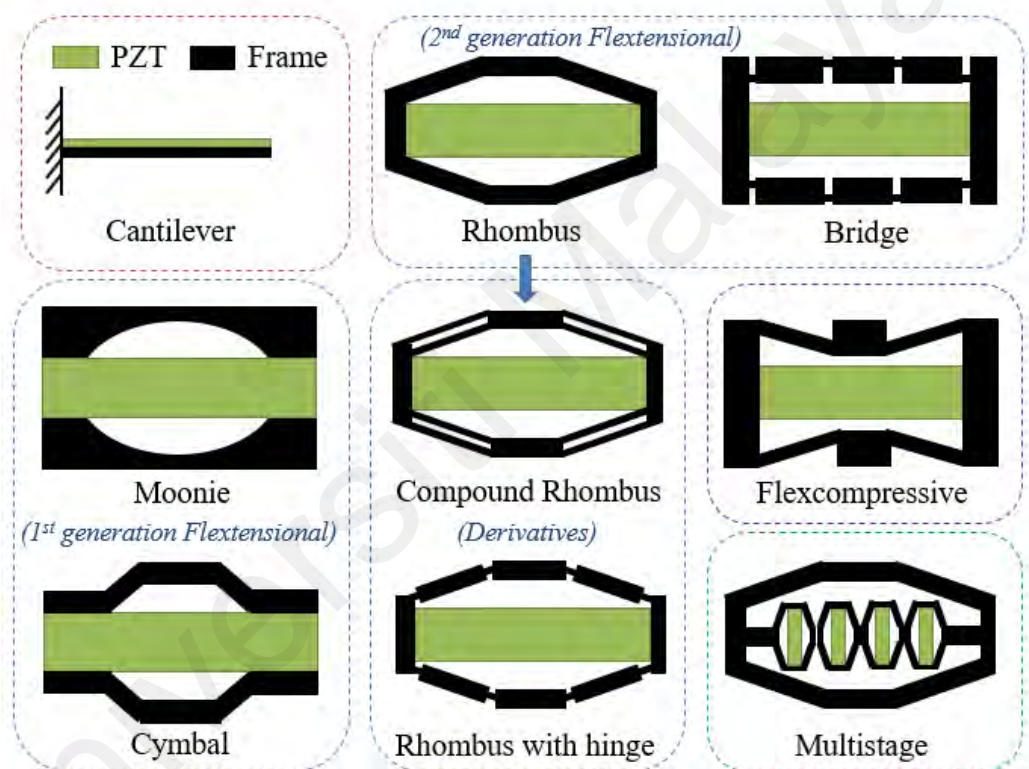


Figure 2.6 Various types of mechanical structure in the piezoelectric transducer

### 2.2.1 Cantilever Structure

The cantilever beam structure is one of the most popular and basic structures in the piezoelectric transducer. Over hundreds of papers were published regarding this fundamental structure since 2004. The cantilever beam transducer consists of a thin layer of rectangular piezoelectric ceramic bonding with a metal plate with different thicknesses. One end of this structure is fixed while the other end is free for any forcing function, probably from the vibration source to act on it. This kind of structure has a great advantage

as its resonance frequency is much lower where a large mechanical strain can be easily generated at the piezoelectric when it is excited at its resonance frequency from a relatively small force (T. B. Xu, 2016).

### 2.2.1.1 Conventional cantilever and proof mass

The cantilever structure is named according to the number of active layers which refers to the piezoelectric layer that is being utilized to produce electricity. A general configuration of a cantilever structure with only one 31-mode piezoelectric layer is named as 'Unimorph' as illustrated in Figure 2.7 (a). On the other hand, a 'Bimorph' structure is constructed with two piezoelectric plates to sandwich the metal plate in the middle. 'Bimorph' structure is constructed with two PZT plates that sandwich the metal plate. Its power output is doubled without a significant change in the device volume (H. Li, Tian, & Deng, 2014).

However, the cantilever structure has a narrow bandwidth where the beam oscillates in a smaller amplitude once the excitation frequency shifts away from the resonance frequency (L. Li et al., 2018). A proof mass is attached at the free end to tune the resonance frequency by changing its mass, size, and location. The power output of a cantilever PEH is proportional to the attached proof mass as it increases the average strain energy (Roundy & Wright, 2004). Hence, the proof mass should be maximized within the design constraints such as the size and beam strength.

A torsional mode cantilever can be achieved by using a pair of asymmetry proof mass which is placed at different distances to the neural axis (Abdelkefi, Najar, Nayfeh, & Ayed, 2011) or using a rotator (Mei & Li, 2013) as shown in Figure 2.7 (b). It improved 30% of energy harvesting performance by undergoing both bending and torsion. Moreover, the locations of the two masses can be chosen to bring the lowest two global natural frequencies closer to each other, leading to a wider bandwidth, which is another

benefit of this design. An impact engaged 2 degree-of-freedom (DOF) harvester was proposed to enhance the dynamic motion of the cantilever during the in-phase mode where a larger impulse will be imparted on the tip mass as shown in Figure 2.7 (c) (Hu, Tang, Das, & Marzocca, 2018).
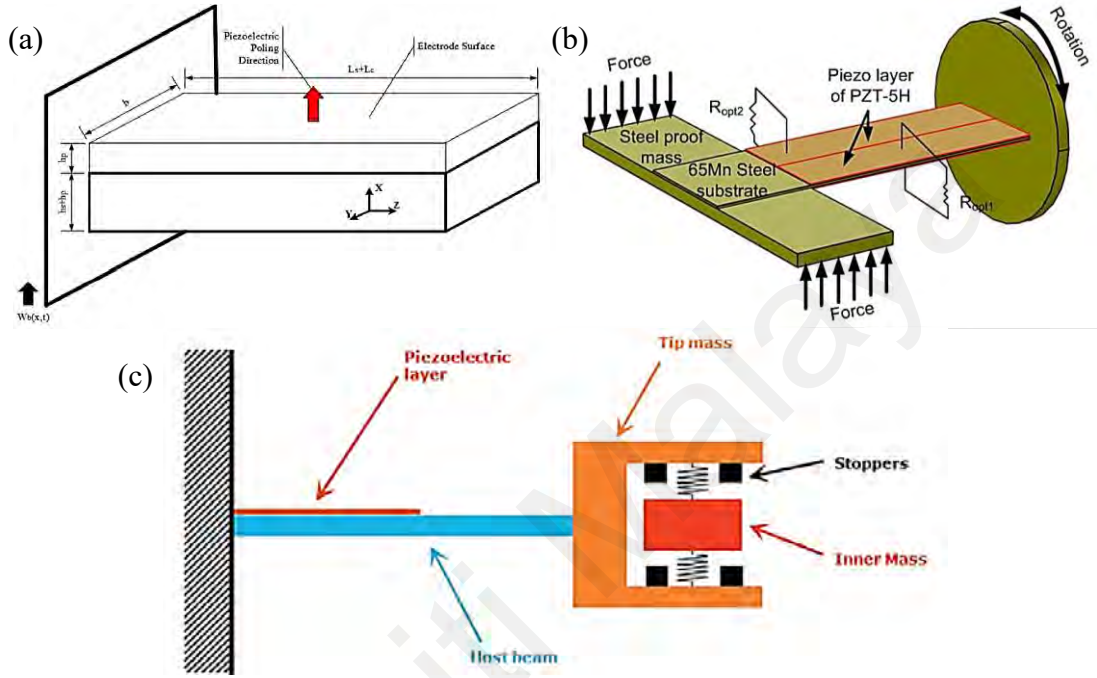


Figure 2.7 (a) Conventional 31-mode Unimorph cantilever PEH (Keshmiri, Deng, & Wu, 2019); (b) Bimorph PEH in torsional mode (Mei & Li, 2013); (c) 2DOF harvester with stoppers (Hu et al., 2018)

### 2.2.1.2 Beam shape

Apart from matching the excitation frequency with the resonance frequency of the energy harvester to achieve maximum deflection of the beam, the strain distribution within the piezoelectric also plays an important role as the power output is largely dependent on the volume of piezoelectric material that is subjected to the mechanical stress. Generally, the stress is maximum at the fixed end and decreases while moving away from the clamp. Thus, the non-stressed part of the piezoelectric does not actually generate much power output and can be removed as shown in Figure 2.8.
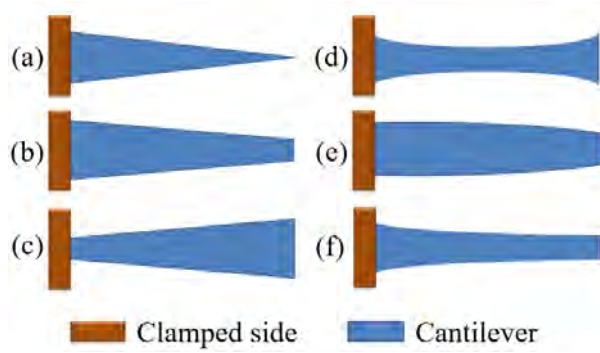
Figure 2.8 Top view of the (a) triangular, (b) tapered, (c) reverse tapered, (d) quadratic, (e) trigonometrically tapered, and (f) exponentially tapered cantilever beam shape

A tapered or triangular shape transducer may achieve constant strain levels throughout the length of the PZT (Glynne-Jones, Beeby, & White, 2001). A tapered cantilever PEH managed to harvest more than twice the energy than the rectangular cantilever due to the rise in bending energy (Roundy et al., 2005). A triangular cantilever showed 25% higher strain and deflection than the rectangular beam with the same base and length dimensions (Mateu & Moll, 2005). However, Dietl and Garcia (2010) presented tapered and reverse tapered cantilever PEHs that had slightly lower power output than the rectangular beam with the same beam length of 60 mm. Benasciutti, Moro, Zelenika, and Brusa (2009) performed a fair comparison among the rectangular, tapered, and reverse tapered structures under two cases. Both tapered structures in case I (same resonance frequency and volumes) were having lower power density (-13.3% and -6.7%) than the rectangular cantilever, while structures in case II (same width of 14 mm) had improved the power output up to 24% and 113% respectively. The reversed tapered cantilever had greater power density than the tapered structure in both cases as the stress at the fixation had been significantly improved. The large area free end could be facilitated to locate the proof mass.

A quadratic shape cantilever PEH was developed which scavenged two times more energy than a rectangular cantilever (Ben Ayed, Abdelkefi, Najar, & Hajj, 2013). Besides, a trigonometrically tapered or exponentially tapered cantilever had up to 45% greater

buckling and flutter capacities than the rectangular beam (Keshmiri & Wu, 2018). A slope angle of 0.94° is tapered along with the thickness of the beam which has a more evenly strain distribution and power amplification factor of 3.6 (Yang et al., 2018). However, due to difficulty in manufacturing such a small slope angle, this method is not widely applied, and hence cantilever with branches is then developed.

Figure 2.9 (a)-(c) shows three beam shapes, namely, T, Pi (π), and E-shaped which are compared with a rectangular cantilever. Although the rectangular cantilever had the highest power output of 87.2 µW, the E-shaped cantilever showed the best performance with the highest displacement of 0.6078 µm and a power output of 49.005 µW (Kaur et al., 2016). A 7-layers zigzag beam PEH with an inclined angle of 12˚was proposed which can be excited from 3 axes as shown in Figure 2.9 (d). Maximum powers of 180 µW, 88 µW, and 56 µW were generated when exciting in vertical, horizontal, and longitudinal directions. The 3-dimensional PEH can realize a wide bandwidth, high acquisition efficiency, and high fatigue life (T. Ma, Chen, Wu, Du, & Ding, 2019). A 2-directional flexible longitudinal zigzag structure (S. Zhou, Chen, Malakooti, Cao, & Inman, 2016) and the multi-branch structure (Xiangyang Li, Yu, Upadrashta, & Yang, 2019), had been proposed for the low-frequency vibration source. Figure 2.9 (e) shows a 31-mode arc-shaped PZT was merged on the cantilever PEH with higher and more uniform distributed stress. It showed 2.55 times and 4.25 times higher power than the plain cantilever PEH for the one half-tube and two half-tubes PEH (Yang, Wang, Zuo, & Zu, 2017).
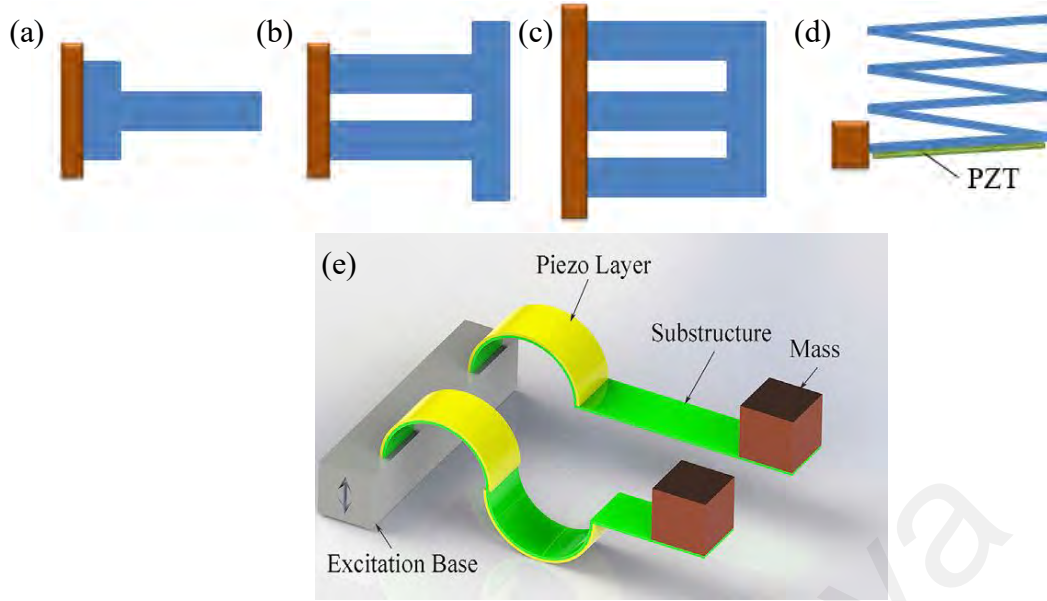
Figure 2.9 Top view of (a) T-shaped, (b) Pi-shaped, and (c) E-shaped cantilever;
(d) Side view of Zigzag cantilever; (e) Cantilever with curved PZT
(Yang, Wang, et al., 2017)

### 2.2.1.3 'd33' & 'd15' mode cantilever

Since $d_{33} > d_{31}$, an interdigitated surface electrode design is introduced to achieve 33-mode PZT, but the poling treatment is complicated (H. Li et al., 2014). Another way is changing the orientation of the PZT by aligning the poling axis parallel with the stressing axis. Due to the limit of poling length in a PZT plate, a few segments of the PZT are combined and formed a piezoelectric ceramic multilayer stack (PZT stack). The $d_{eff}$ of the PZT stack is the multiplication of $d_{33}$ with the number of piezoelectric layers and an efficiency constant. The constant depends on the constraint effect from electrodes, the ratio of electrode area over the total area of the piezoelectric plate, and the encapsulation layer of the multilayer stack (T.-B. Xu, Siochi, et al., 2011). The $d_{eff}$ of the PZT stack is $1.39 \times 10^6$ pC/N at resonance, which is larger than a single PZT plate ($< 1 \times 10^4$ pC/N) with the assumption of 80% power transition efficiency. The power density is significantly higher than a similar size cantilever type PEH and increases with the number of PZT layers. The harvested energy was successfully stored in a 6600 F supercapacitor and charged from 0 to 4.48 V in 1.0 s, which equals 66.2 mJ of electrical energy (T.-B.

Xu et al., 2013). Generally, the PZT stack is suitable for a large force environment due to its high mechanical stiffness.

The 33-mode PZT stack is embedded with the cantilever structure to examine the effect of different PZT stacks number, lengths, and thickness. The PZT plates were assembled in series but connected electrically in parallel to offer a larger electrode area, higher electric current, and lower impedance as shown in Figure 2.10 (a). The stack design managed to decrease the natural frequency of the harvester. Meanwhile, increasing the PZT's length will lead to higher charge and voltage outputs (Keshmiri et al., 2019). Figure 2.10 (b) shows a barbell-shaped PEH with a 33-mode ring-type PZT stack that can overcome the failure of the epoxy bonding layer and sustain larger impacts (J. Wu et al., 2016).

J. Zhao et al. (2012) proposed a cantilever harvester with two 15-mode piezoelectric plates ($13.0 \times 2.5 \times 1.0$ mm$^3$) which were series-connected to utilize the shear effect. It had a greater power output than that with only one 15-mode piezoelectric plate even in a larger size ($13.0 \times 6 \times 1.0$ mm$^3$). However, due to manufacturing difficulty in the polarization process which requires extremely high voltage (up to 80 kV and a maximum possible poling length of 32 mm can be manufactured by DeL Piezo Specialties to ensure good poling.), 15-mode is less utilized. So, there is room for improvement in this aspect in the future.
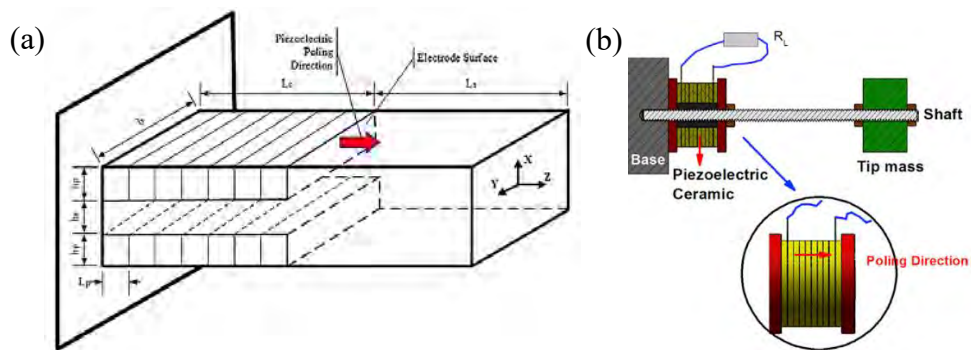


Figure 2.10 (a) 33-mode PZT stack cantilever harvester (Keshmiri et al., 2019); (b) Barbell-shaped cantilever harvester (J. Wu et al., 2016)

### 2.2.1.4 Magnetic tunable cantilever

Challa, Prasad, Shi, and Fisher (2008) proposed a magnetic field tunable cantilever PEH to alter the stiffness and tune the resonance frequency from 26 Hz to 22-32 Hz with a power output of 240-280 µW. Harne and Wang (2013) then presented the difference between magnetic attraction and repulsion bistable harvester. Figure 2.11 (a) shows a magnetic attraction PEH which can be multi-stable based on the angular orientation of the external magnets (Huang, Zhou, & Litak, 2019). An asymmetric U-shaped cantilever was adopted to exhibit a magnetic nonlinearity with multimodality as shown in Figure 2.11 (b). It yielded a closer two resonance frequencies bandgap compared to the linear one without the two permanent magnets. Hence, this design shows higher energy output, lower and closer resonance peak (Sun & Tse, 2019).

Two stoppers are added to an inverted cantilever to confine the beam's deflection range so that the elastic force dominates the magnetically attractive coupling employed in the PEH, making the device monostable as shown in Figure 2.11 (c) (Erturk, Hoffmann, & Inman, 2009). By altering the spacing between the tip mass and the external magnets, the operating frequency can be tuned (Fan, Tan, Liu, Zhang, & Cai, 2019). S. Zhou, Cao, Erturk, and Lin (2013) used rotatable magnets to obtain a broad low-frequency range of 4–22 Hz within a compact design by altering the magnet's inclination angle rather than changing the magnet spacing. A non-contact magnetic plucking is induced to achieve frequency up-conversion in a knee-joint PEH as shown in Figure 2.11 (d). The knee-joint motion will excite the 8 Bimorphs PEHs through the repulsive force between the primary magnets (PM) and the secondary magnets (SM). The repelling configuration produced 3.6 times higher energy output than the attracting configuration. An average power output of 5.8 mW was generated under a knee-joint motion at 0.9 Hz (Kuang, Yang, & Zhu, 2016).
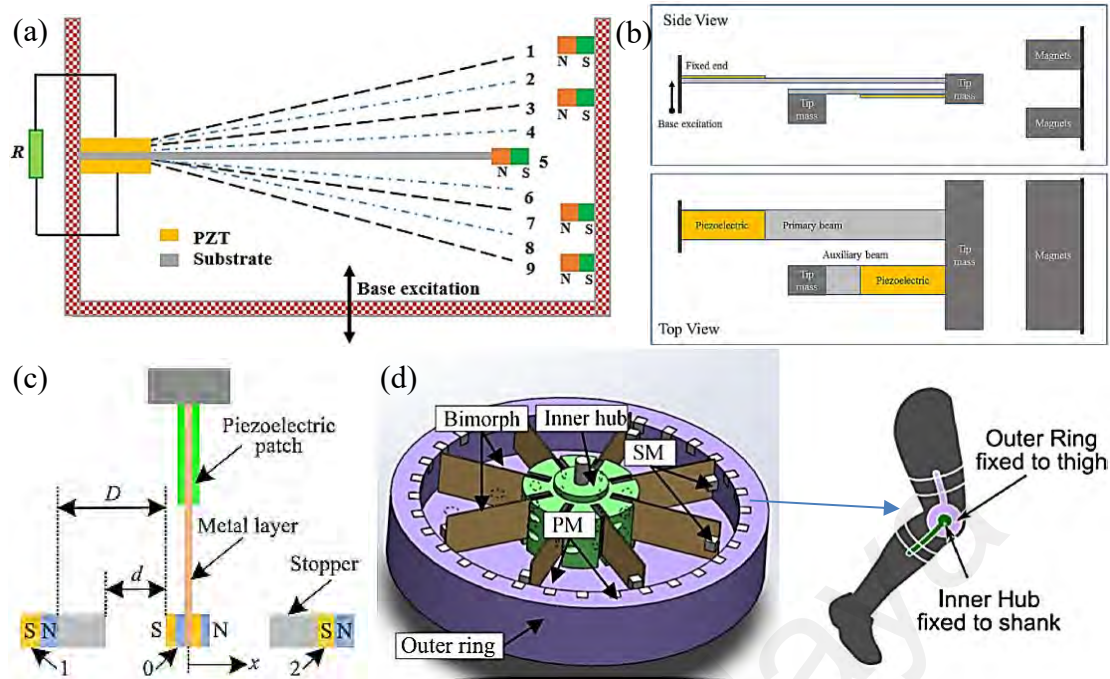
Figure 2.11 (a) Structural schematic of a magnetic attraction multi-stable PEH (Huang et al., 2019); (b) Asymmetric U-shaped magnetic repulsion PEH (Sun & Tse, 2019); (c) Vertical Bimorph cantilever PEH in a magnetic field with two additional stoppers (Fan et al., 2019); (d) Schematic diagram of knee-joint PEH with frequency up-conversion induced by magnetic plucking (Kuang et al., 2016)

### 2.2.1.5 Pre-stressed & edge-clamped

Reduced and Internally Biased Oxide Wafer (RAINBOW) and Thin Layer Unimorph Driver (THUNDER) are two pre-stressed transducers developed by NASA in the 1990s. RAINBOW consists of a PZT layer and an oxygen reduce layer (Haertling, 1999). However, it is more brittle and not suitable for high force roadway environments (H. Zhao et al., 2012). On the other hand, THUNDER is constructed by sandwiching the piezoelectric layer with aluminum and stainless steel layers which are heated and cooled rapidly. The difference in thermal expansion coefficients introduces the pre-stress in the PZT (Mossi, Selby, & Bryant, 1998). THUNDER structure has higher block force, displacement, and fatigue life, which can withstand higher force up to 0.5 MPa. Hence, due to its lower stiffness than the road, this structure design is considered not suitable for roadway application (H. Zhao et al., 2012). Umeda, Nakamura, and Ueha (1996) developed a pressure mode all edge clamped circular PEH with a piezoelectric disc bonded to a bronze disc with high stiffness as shown in Figure 2.12. The two sides of the

diaphragm must be isolated to create stress in response to a pressure change in the surrounding medium (S. Kim, Clark, & Wang, 2005). The power output is 1-20 mW, which is higher than a cantilever but lower than a flextensional PEH (T. B. Xu, 2016).
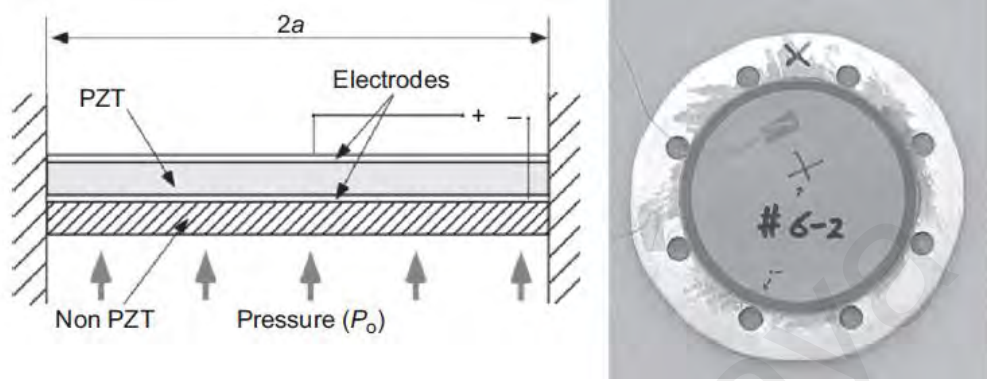


Figure 2.12 Edge-clamped Circular Diaphragm (T.-B. Xu, 2016)

In summary, Cantilever structures such as 'Unimorph', 'Bimorph', and THUNDER are widely used in energy harvesting from mechanical vibration. However, the energy source of moving vehicles on the roadway is driven by stress acting from the tire to the ground than the vibration energy. Moreover, the frequency of the vehicle load in motion is normally 0.1 to 10.0 Hz which is relatively low (H. Li et al., 2014). Hence, the cantilever type transducer is not analyzed in this study.

### 2.2.2 First Generation Flextensional Structure

A cantilever typed harvester may achieve high power output under its resonance mode. However, long-term excitation at its natural frequency may lead to a shorter lifetime as fatigue may occur due to its weak mechanical strength (H. W. Kim et al., 2004). Hence, the piezoelectric harvester is aimed to work under a higher forcing environment with a larger scale of piezoelectric deformation to obtain larger power generation. In consequence, the first generation of flextensional structure is developed with higher robustness and magnification function. This structure converts the transverse input force into larger lateral tension or compression output force acting on the piezoelectric plate

which improves the power output from mW/device up to tens of mW/device (T.-B. Xu, 2016).

### 2.2.2.1 Moonie, Cymbal, and Rectangular Cymbal

Moonie structure is constructed with two half-moon shaped metal end caps to protect the PZT under high stress level as shown in Figure 2.13 (a) (H. Kim, Tadesse, & Priya, 2009; Shixin & Li, 2001). Figure 2.13 (b) shows a Cymbal structure is designed to reduce the stiffness of the Moonie frame and stress concentration in the PZT. Thus, the allowable applied stress and the displacement can be increased (H. Zhao et al., 2012). The Cymbal structure comes in circular and rectangular shapes as shown in Figure 2.13 (c) and (d), where Rectangular Cymbal is named as Bridge or Trapezoidal Bridge in some papers. Figure 2.13 (e) and (f) show a metal ring and threaded bolts are used to avoid the asymmetries configuration and improve the mechanical coupling effect instead of using epoxy adhesive only (Bejarano, Feeney, & Lucas, 2014).
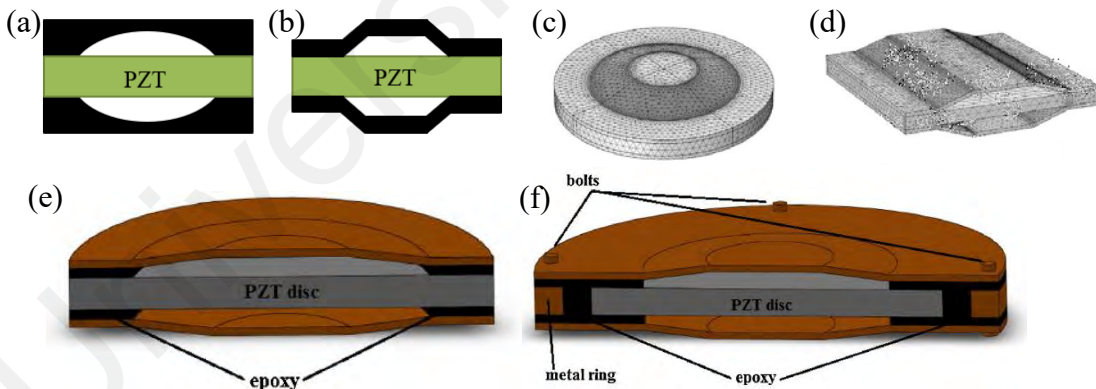


Figure 2.13 (a) Side view of Moonie and (b) Cymbal; (c) The structures of conventional circular Cymbal and (d) Rectangular Cymbal (Jasim et al., 2017); (e) Conventional epoxy bonding in Cymbal structure; (f) Reinforced bonding with retarded metal ring and bolts design (Bejarano et al., 2014)

A strain amplification factor ($\approx \varnothing_c/2h$) of 8.5 was calculated for the Cymbal structure based on the cavity height, $h$ and cavity diameter, $\varnothing_c$ (H. W. Kim et al., 2004). The authors also tested several types of PZT material. The D210 PZT shows the highest voltage output due to its higher $g$ than the soft APC-850 PZT and hard APC-841 PZT. In another study,

PZT-5H shows the highest ($d·g$) values in both 31 and 33-mode while PZT-5A has the highest ($d·g$) value in 15-mode as compared with PZT-2, PZT-4, and PZT-8 (H. Zhao et al., 2012). A Cymbal structure showed an amplification factor of 16-22 based on the standalone PZT plate's voltage output under an impact force (L. Wu, Chure, Wu, & Tung, 2014). X. Liu and Wang (2019) adopted the PZT stack design by having two PZT rings and three metal rings alternatively in the Cymbal structure to improve the power output in a high force roadway environment as shown in Figure 2.14 (a).

Zhao et al. (2010) selected the ordinary Cymbal PEH to harvest energy from asphalt pavement due to its low cost, high reliability, and reasonable efficiency. A bury depth of 40 mm and contact stress of 0.7 MPa (25 kN/tire) were set in the FEA. Increasing the diameter of Cymbal will enhance the voltage but decrease efficiency. The maximum output power was 1.2 mW with the assumption of 20 Hz vehicular frequency. 200 kW of harvested electricity had been reported from one lane-mile of highway in Israel and China which exhibited the possibility of roadway PEH application (Zhao, Ling, & Fu, 2013). Another study shows that one Cymbal PEH can generate 16 µW for the pass of one heavy vehicle wheel as shown in Figure 2.14 (b). 40–50 MWh/m$^2$ energy density can be obtained from 100 m road with the use of 30 thousand cymbals, which can account for >65 MWh annually (Moure et al., 2016).
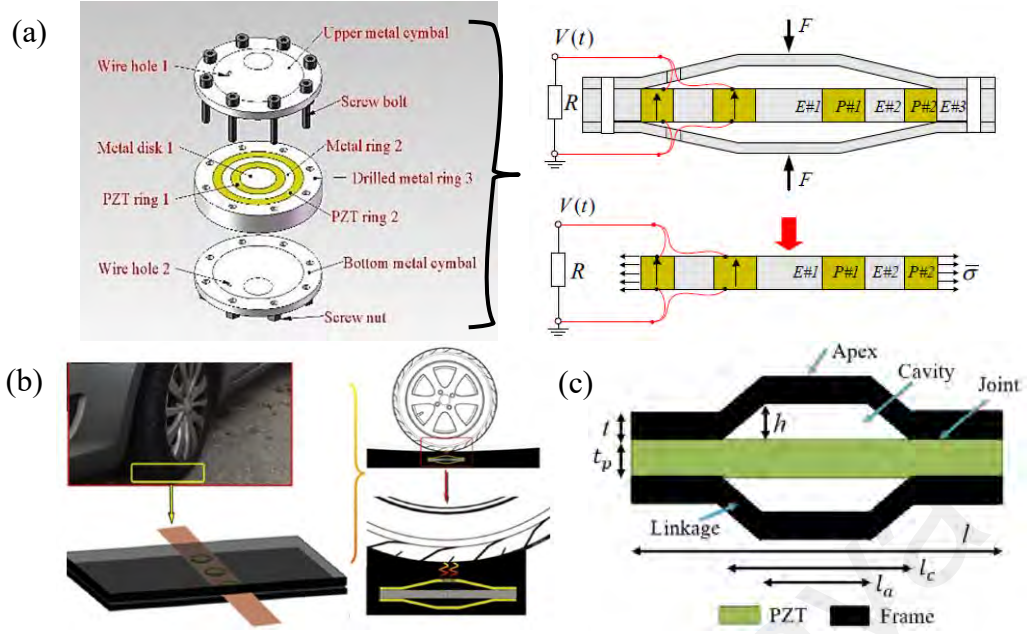
Figure 2.14 (a) Radially layered 31-mode Cymbal PEH (X. Liu & Wang, 2019);
(b) Vehicular loading of the wheels deform the asphalt and excite the Cymbal PEHs
which are embedded in the pavement (Moure et al., 2016);
(c) Schematic of a Rectangular Cymbal PEH

Rectangular Cymbal has the highest values of $V$, $W_l$, $U_E$, $k$, and $\lambda_{max}$, followed by the Cymbal and lastly the Moonie under the roadway condition (H. Zhao et al., 2012). H. W. Kim et al. (2004) agreed that the Cymbal structure was preferred over the Moonie in terms of low fabrication cost, high stability under high loading force, and large displacement. The Cymbal structure with higher $d^{eff} \cdot g^{eff}$ was more efficient than the cantilever PEH since the $d^{eff}$ value of the Cymbal is contributed by combining $d_{33}$, $d_{31}$, and its amplification factor, $\alpha$ as $d^{eff} = d_{33} - \alpha d_{31}$. The minus sign is because of the negative value of $d_{31}$ (Ren, Or, Zhao, & Luo, 2010).

The flextensional structures are recommended for roadway application because of their reasonable efficiency and stiffness compared to the THUNDER and a standalone PZT stack even they have higher $k$ and $\lambda_{max}$ values. The PEH should have the same stiffness as the pavement to reduce its influence on the pavement. Moonie has a lower efficiency (H. Zhao et al., 2012) and thus Cymbal and Rectangular Cymbal structures are recommended for energy harvesting in high force environment which can be up to thousands of Newton,

such as under floor tiles, shoes, roadway pavement, or machine suspensions, due to its inherent structure (Zhao et al., 2010).

### 2.2.2.2  Slotted Cymbal

Figure 2.15 (a) shows a slotted Cymbal with fringe radial slots is developed to release high circumferential stress and minimize the loss of mechanical input energy. More radial slots up till the slanted part of the Cymbal had been designed, which is named as cone radial slot as shown in Figure 2.15 (b). The power output was 0.6 times higher than the original Cymbal with 18 cone radial slots. The output voltage and power increased with the number and length of radial slots (J.-b. Yuan, Shan, Xie, & Chen, 2009). A circumferential slot had been tested with various depths which produced 0.8 times higher power than the ordinary Cymbal. However, the slotted design will reduce Cymbal's rigidity and difficulty may arise during the fabrication process (J. Yuan, Shan, Xie, & Chen, 2010).
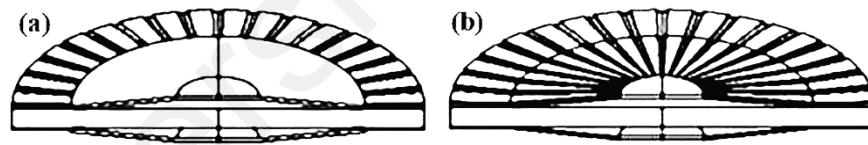


Figure 2.15 Slotted Cymbal with (a) fringe radial and (b) cone radial slots
(J.-b. Yuan et al., 2009)

### 2.2.2.3  Addition of substrate

Figure 2.16 (a) shows the PZT cracks at the contact area with the Rectangular Cymbal under 0.8 MPa (H. Zhao et al., 2012) as the stress concentrations exceed the PZT's yield strength of 35 MPa. An additional steel substrate which is 8.38 times thicker than the PZT, is introduced to reinforce the PEH and work safely under 1940 N. However, most of the input energy has been absorbed by the substrate, causing a low power output of 121.2 μW (Arnold, Kinsel, Clark, & Mo, 2011; Mo, Arnold, Kinsel, & Clark, 2013). Daniels et al. (2013) then proposed dual-layer substrates with a lower thickness that

sandwiched a 31-mode PZT plate to achieve the shielding effect from both sides and increase the load capacity as shown in Figure 2.16 (b). Figure 2.16 (c) shows the force amplification mechanism which transfers the compressive load force, $F$ into tensile force $F_{xp}$ along the $x$-axis. The total tensile force exerted on the sandwiched structure, $F_{tx}$ is calculated as shown in [2.15].

$$F_{tx} \ = \ 2F_{xp} \ = \ 2F_x \ = \ F \cot\theta \qquad\qquad [2.15]$$

where $\theta$ = the end cap internal angle; $\cot\theta$ = the amplification factor.

Figure 2.16 (d) and (e) show the overall stress has been reduced with the addition of dual-layer substrates (Kuang, Daniels, & Zhu, 2017). Luo, Liu, Zhu, and Ye (2017) then used sequential quadratic programming to optimize the parameters of the PEH. Rectangular Cymbal structure was used to fully utilize the best orientation of PZT materials. It is then applied as a footwear PEH as shown in Figure 2.16 (f). The ideal force amplification ratio of the Rectangular Cymbal is calculated based on the kinematic mechanism. It is equal to $\cot\theta$ where $\theta$ is the end cap internal angle, which is agreed by Xiaotian Li et al. (2011). The end caps will amplify the incident force when $\theta < 45°$. However, there is an optimum angle which is 15° in this design as the amplification factor will reduce when the inclined linkages are shortened by the large forces at an extremely small angle. The optimum configuration should be evaluated by considering the balance between energy harvesting performance and mechanical failure potential due to stress concentrations. For example, minimizing the end cap thickness can maximize the power output, but a thicker end cap can withstand a higher loading force (Kuang et al., 2017).
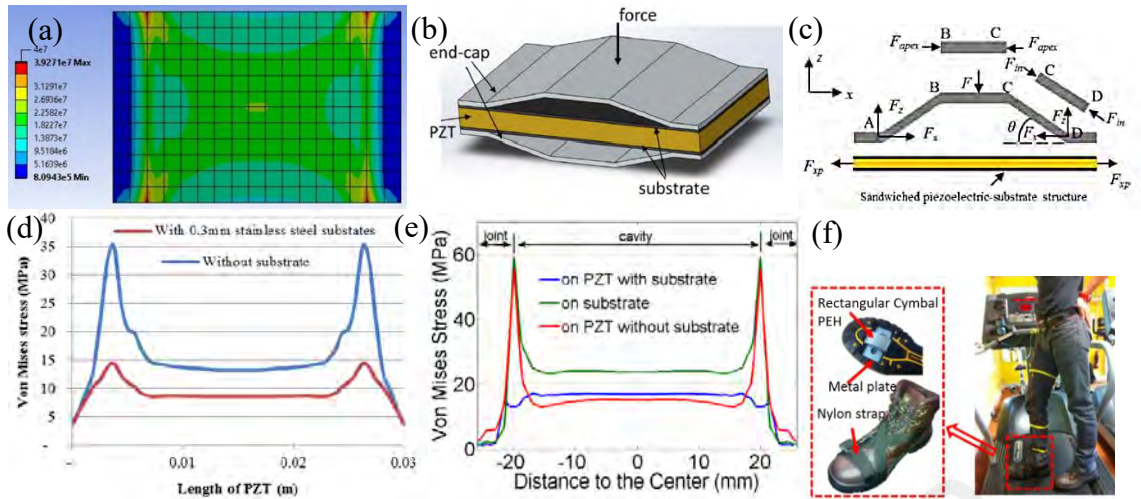
Figure 2.16 (a) Stress distribution of the PZT plate under high loading force © 2019 IEEE; (b) & (c) Rectangular Cymbal PEH with dual layer of substrates and its force amplification mechanism (Kuang et al., 2017); (d) & (e) Stress distribution of the PZT plate along the length of PZT with and without substrates (Kuang et al., 2017); (f) Experimental setup for testing the Rectangular Cymbal PEH as a footwear energy harvester (Kuang et al., 2017)

### 2.2.2.4 33-mode stacked-PZT Rectangular Cymbal

Figure 2.17 (b) shows a Rectangular Cymbal structure with a seven-layer parallelly connected 33-mode PZT-5X stack, which has a higher ($d \cdot g$) value than PZT-5H. It produces four times more energy than the traditional 31-mode Cymbal PEH. The thickness of the end cap and PZT, as well as the cavity height, are the key factors in optimizing the performance of PEH. It is demonstrated as a roadway PEH by having 64 parallel-connected Cymbal PEHs assembled in a 177.8 × 177.8 × 76.5 mm³ Aluminium casing as shown in Figure 2.17 (c) (Jasim et al., 2017).
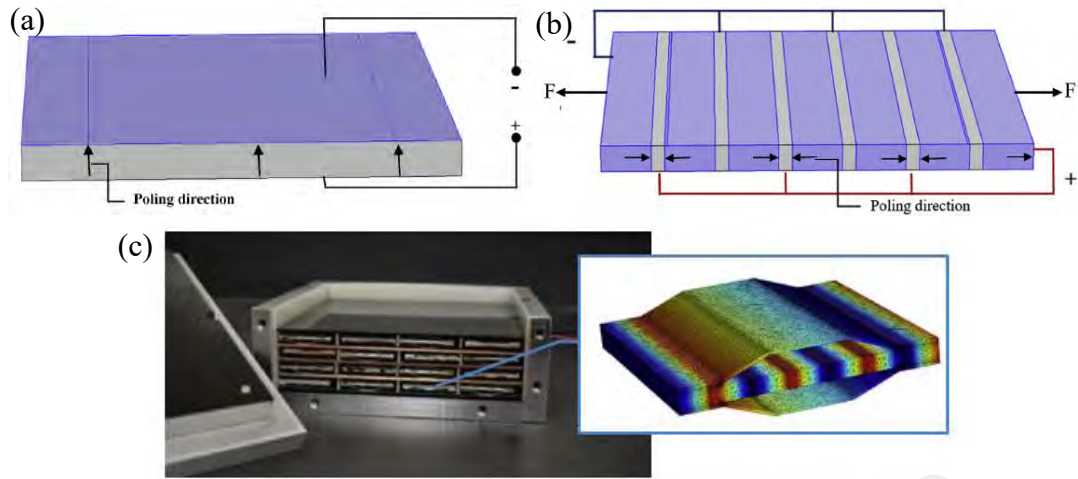
Figure 2.17 (a) 31-mode conventional PZT plate; (b) 33-mode parallelly connected PZT stack; (c) Prototype of a roadway PEH with 64 33-mode Rectangular Cymbal transducers (Jasim et al., 2017)

### 2.2.2.5  Arc and Arch Cymbal

Two arc shape rectangular Cymbal structures are designed to mitigate the effect of stress concentration as shown in Figure 2.18. The maximum electric potential of the Arch is higher than the Arc, followed by the Rectangular Cymbal. The voltage drops with a higher modulus and thicker end cap. In terms of load capacity, the Rectangular Cymbal has a maximum load at 1 MPa, followed by the Arch of 0.8 MPa and Arc of 0.7 MPa. The Arc is fragile due to its large maximum tensile stress and shear stress, whereas the Arch has high durability, strong capability to resist pressure, and high energy conversion efficiency to work as a pavement PEH (Zhao et al., 2015). However, the bonding strength and technique should be improved to cope with the shear stress (Zhao, Qin, & Ling, 2018). A circular Arch end caps are bonded to the Brass rings, then to the PZT disc and demonstrated as a shoes PEH. However, the Brass rings will reduce the transmission of energy to the PZT disc. The capacitance of the component will increase with a larger PZT area but a smaller PZT thickness. Hence, the matching impedance will reduce, resulting in higher power output and a lower force demand (Leinonen, Palosaari, Juuti, & Jantunen, 2013; Palosaari, Leinonen, Hannu, Juuti, & Jantunen, 2012).
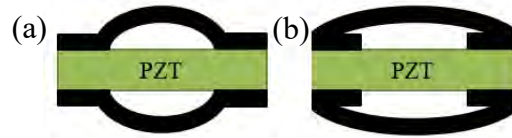
Figure 2.18 Front view of the (a) Arc and (b) Arch Rectangular Cymbal structure PEHs

### 2.2.2.6 Combined structure

It is difficult to excite the high-stiffness Cymbal PEH at its high resonance frequency as the ambient vibration sources normally are below 300 Hz (Dutoit, Wardle, & Kim, 2005). C. Xu, Ren, Di, et al. (2012) combined a high flexibility Cantilever beam with two Rectangular Cymbals structures, which are named as CANtilever Driving Low frequency Energy harvester (CANDLE) as shown in Figure 2.19 (a). It produced high power output at a low frequency, which is 4.9 times higher than the Cymbal PEH. The proof mass can convert more electrical energy from vibration sources and lower the natural frequency (C. Xu, Ren, Liang, et al., 2012). Tufekcioglu and Dogan (2014) applied the CANDLE concept with two circular Cymbal PEHs which consisted of a d31 two-layer-stacked PZT-5H disc each as shown in Figure 2.19 (b) and (c). But the harvesting performance is lower than the rectangular CANDLE.
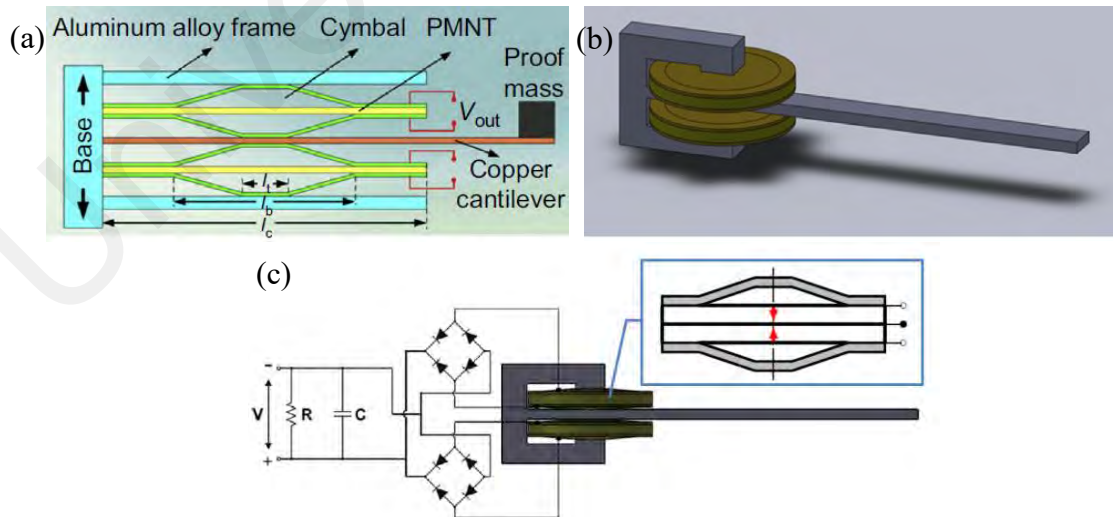


Figure 2.19 CANDLE based on a pair of (a) Rectangular Cymbals
(C. Xu, Ren, Di, et al., 2012) and (b) a pair of circular Cymbals with
(c) d31 two-layer-stacked PZT-5H disc (Tufekcioglu & Dogan, 2014)

Zou et al. (2016) introduced a nonlinear magnetic repulsive force by placing a Rectangular Cymbal PEH with a magnet opposite to the free end of the Cantilever to increase the bandwidth and power density. With the magnetic pressure exerted on PEH as the beam oscillated, the PZT was subjected to a tensile force. Zou et al. (2017) used another two PEHs as stoppers which can limit an unwanted large displacement of the tip magnet as shown in Figure 2.20. The energy loss caused by the magnetic stoppers was smaller than the collision stoppers. This design improves the harvesting performance from low-frequency weak vibrations source.
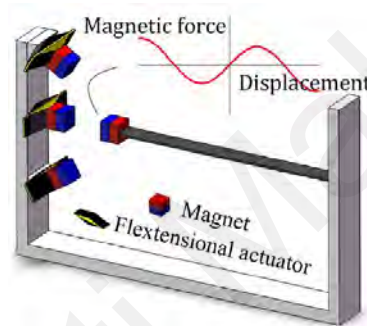


Figure 2.20 Combined structure of cantilever and flextensional transducers with nonlinear magnetic repulsive force (Zou et al., 2017)

### 2.2.2.7 Compressive mode Cymbal

Since the compressive yield strength of piezoelectric material is 10 times higher than its tensile yield strength which can be up to 600 MPa (270 MPa vs 35 MPa, estimated by STEINER & MARTINS, Inc), the compressive mode PEH is designed to withstand higher force (Yang, Zhu, & Zu, 2015; Yang, Zu, Luo, & Peng, 2016). A d31 PZT ring is compressed through an inner flextensional Cymbal structure to increase the power output and eliminate the bonding failure issue with an outermost retaining ring as shown in Figure 2.21 (a). The PZT ring is replaced by four d33 PZT stacks to further increase the power output as illustrated in Figure 2.21 (b) (Purviance, Wickler, Clayson, Barnes, & Mo, 2013). Two coil-type d33 PZT stacks are twined at the two ends of the Rectangular Cymbal with an outermost shaft that pre-compressed them. Larger electric voltage and

power output are produced if compared with Bimorph or tensional Cymbal PEHs (Xiaotian Li et al., 2011).

Figure 2.21 (c) shows another compressive mode Rectangular Cymbal PEH with two d33 PZT stacks was designed to sustain under heavy loads (X. Wang, Shi, Wang, & Xiang, 2016). Two compressive mode PEHs were combined and connected by a supported beam, which acted as a shared loading platform. It showed over 400% harvested energy if compared with two independent compressive mode PEHs (X. Wang & Shi, 2017). In short, compressive mode PEH has higher load capacity, lower resonance frequency, and higher power density than the conventional PEH including the standalone PZT stack. However, this design required the PZT to be placed outside of the end caps, resulting in a bulky design, which may not be suitable for applications with limited space such as under the shoes (Xiaotian Li et al., 2011).
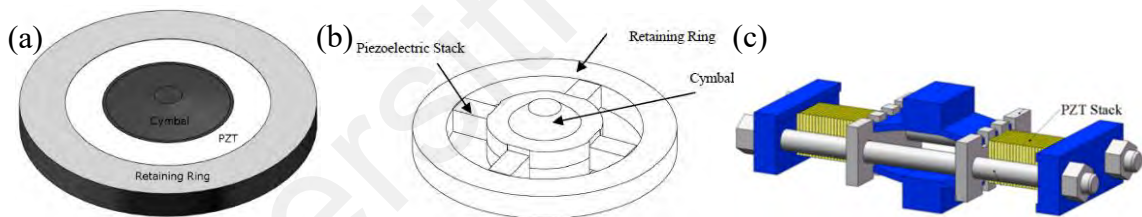


Figure 2.21 (a) first design by using PZT ring; (b) second design by using PZT stack © *2013, IEEE* (Purviance et al., 2013); (c) Flexcompressive Rectangular Cymbal PEH (Yang et al., 2018)

### 2.2.2.8 Compressive mode combined structure

Yang and Zu (2014) developed a compressive mode Rectangular Cymbal PEH using the cantilever beams and proof mass to increase the power output and wider the bandwidth as shown in Figure 2.22. When the PEH is excited under a base vibration, the mechanical energy is absorbed by the elastic beams and mass blocks. A pulling force is then induced on the end caps as the cantilever oscillates, resulting in compressive stress in the PZT plate. The Rectangular Cymbal can generate 100% higher voltage than a circular Cymbal as higher effective stress is found in the rectangular PZT (Yang et al., 2015). A force

amplification ratio of 6.3 is reported for the Rectangular Cymbal structure at 6.34˚ (Yang et al., 2016). The hinge design at the clamped connection between the cantilever ends and the base as well as the proof mass can reduce the stiffness and enlarge the deflection. The fully hinged PEH had 3 times higher voltage output, 15% lower natural frequency, and 37% broader frequency bandwidth, compared to the clamped design (Z. Li, Zu, & Yang, 2018).
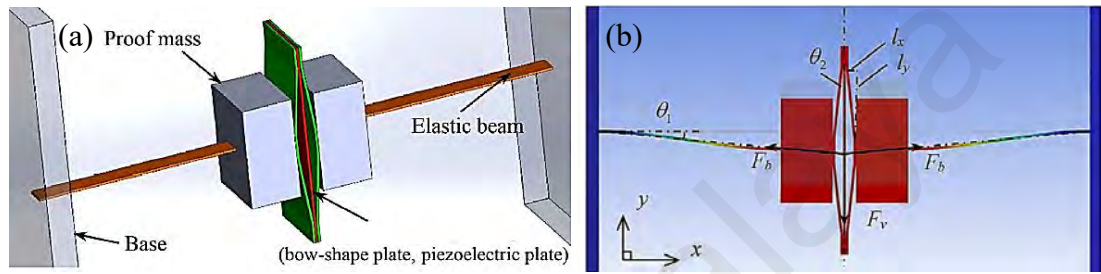


Figure 2.22 (a) Isometric view and (b) front view of a compressive mode combined structure of Rectangular Cymbal and elastic beam with mass blocks PEH
(Yang & Zu, 2014)

In short, the first generation flextensional typed structure has been well developed over the years. Combination or compressive mode by using a few types of the first generation flextensional is impressive. Although each of these structures has its pros and cons, modification can be done to match the design with the forcing environment.

### 2.2.3 Second Generation Flextensional Structure

In this section, the second generation and the derivative of flextensional structure will be discussed, where Rhombus and Bridge structures are the basis and popular core mechanism in engineering applications.

#### 2.2.3.1 Rhombus

The second generation flextensional structure is designed to overcome the destructiveness of the first generation flextensional structure such as the bonding failure issue. Rhombus structure can achieve this by clamping the PZT plate from the vertical sides as shown in Figure 2.23 (a). The ideal displacement amplification ratio, $G_{ideal}$ of the Rhombus is equal

to cot $\theta$, which is similar to the Cymbal structure as they share the same quarter model shown in Figure 2.23 (b) (H.-W. Ma, Yao, Wang, & Zhong, 2006). In fact, the flexure linkage possesses both bending and longitudinal stiffness which causes elastic energy stored in the mechanism. The actual displacement amplification ratio, $G_{actual}$ can be derived as shown in equation [2.16]. A maximum amplification ratio of 9.47 is proven when the angle, $\theta$ equals 3.04° (Shao, Xu, Chen, & Feng, 2014).

$$G_{actual} = \frac{\Delta y}{\Delta x} = \frac{l_a \cos\theta}{\dfrac{t^2 \cos^2\theta}{1.5 l_a \sin\theta} + l_a \sin\theta} \tag{2.16}$$

Ling et al. (2016) included the input stiffnesses ($K_{in}$, $K_v$, and $K_{PZT}$) of the compliant mechanism in the calculation, rather than the bending stiffness ($K_\theta$) and translational stiffness ($K_l$) only. This is because the output displacement of a PZT stack will be reduced due to the preload if compared with the free-operating Rhombus structure. The calculated displacement amplification ratio, $R_{amp}$ is 13.05, using equation [2.17], which is <10% deviated from the experiment.

$$R_{amp} = \frac{K_{PZT} K_v}{K_{PZT} + K_{in}} \times \frac{K_l L^2 \sin\theta \cos\theta}{12 K_\theta \cos^2\theta + K_l L^2 \sin^2\theta} \tag{2.17}$$
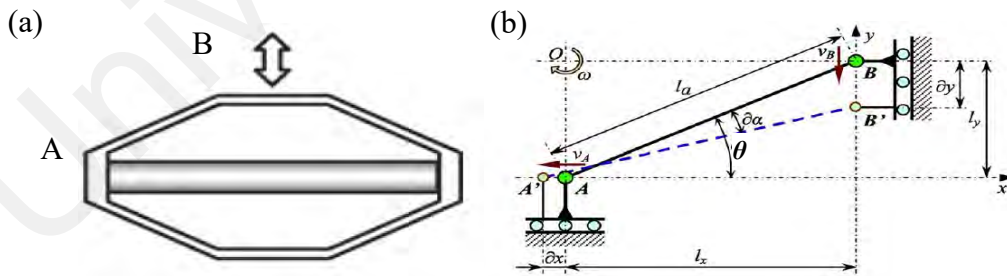


Figure 2.23 (a) Rhombus structure PEH and (b) its quarter amplification mechanism kinematic model where $\theta$ is the inclined angle (H.-W. Ma et al., 2006)

### 2.2.3.2 Rhombus with hinges

H. Zhou and Henson (2007) proposed a Rhombus structure with additional hinges design at the four linkage arms. The hinges have lower thickness and less stiffness than the arms which ease the deformation of the frame. Fillet is designed to reduce stress concentration

at the corner (Ouyang, Zhang, & Gupta, 2005). However, it has a lower load capacity and safety factor since the bending area is concentrated at the hinges (Wen, Xu, & Zi, 2018). Hence, the hinge design is suitable when large deformation and amplification ratios are desired under low excitation force.

Feenstra et al. (2008) applied this structure in developing a compressive mode PEH which utilized the differential forces exerted in the straps of a backpack due to walking, as shown in Figure 2.24. A tensional outward pulling force was applied to the Rhombus structure through the backpack strap and the PZT was being compressed by the extended part from the sides. This lightweight transducer backpack design only leads to minimal parasitic effects, making it a feasible method of gathering energy from human motion. A mean power of approximately 0.4 mW is produced from each piezoelectric device, which could power some low power electronics.
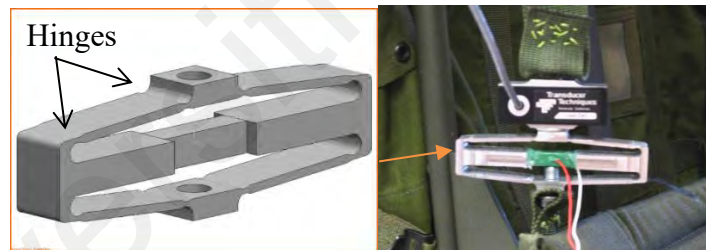


Figure 2.24 Rhombus structure PEH and its backpack application (Feenstra et al., 2008)

### 2.2.3.3 33-mode stacked-PZT Rhombus

A 33-mode multilayer-stacked-PZT Rhombus PEH which is named as APA 400M is reported with lightweight (19 g) and compact size (48.4 × 11.5 × 13.0 mm$^3$) as shown in Figure 2.25 (a) (Sosnicki, Lhermet, & Claeyssen, 2006). The poling directions are indicated with red arrows as shown in Figure 2.25 (b) (W. Zhou & Zuo, 2013). The experiment results show that the mechanical-to-electrical energy conversion efficiency is 19%. It has three main advantages over the standalone PZT. Firstly, 48.6 times more mechanical energy is transmitted into the PZT through the Rhombus frame. Secondly, the energy conversion efficiency is about three to fivefold by utilizing a 33-mode PZT.

Lastly, 26.5 times more electrical charge is generated through the parallel-connected PZT stack (W. L. Zhou, Zuo, & Asme, 2014). By adding a 500 g proof mass on top of the structure, 328.34 mW can be generated at its natural frequency of 138.1 Hz. It is 164 times higher than a non-proof mass structure with a natural frequency of 936 Hz (T.-B. Xu et al., 2013).
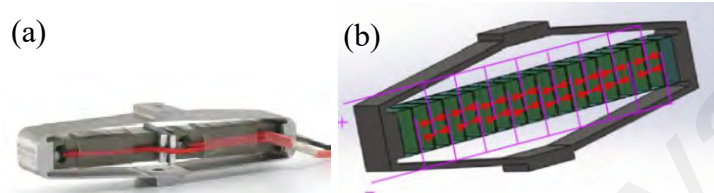


Figure 2.25 (a) Cedrat, APA 400M (CEDRAT TECHNOLOGIES, 2020);
(b) Parallel-connected multilayer PZT stack in Rhombus PEH (T. B. Xu, 2016)

### 2.2.3.4 Compound Rhombus

Compound Rhombus was designed to strengthen the PEH with higher stiffness and load capacity by increasing the beam number for the four arms. The distance between two adjacent beams was set at 1.5 mm to avoid manufacturing difficulty. The FEA force amplification factor was computed based on an input force of 400 N and the corresponding output force acted at the PZT, which was equaled to 4.33 for a single beam design with a safety factor of 1.5. The four-beam compound structure had a lower amplification factor of 3.88 but a higher safety factor of 3.03. The maximum stress had been reduced and the safety factor had been enhanced with the increasing number of beams. However, the force amplification ratio was decreased, and the overall frame size was increased. Eventually, the two-beam compound Rhombus was adopted with an amplification ratio of 4.17 and a safety factor of 2.42 (Wen et al., 2018).

### 2.2.3.5 Combined Rhombus structure

Two Rhombus structures are coupled with a cantilever to harvest energy from fluid motion and power the systems deep in an oil well with high pressure (200 MPa) and temperature (>160˚C). Figure 2.26 (a) shows the flow-induced vibration will excite the

cantilever and be amplified by the Rhombus structure to act on the PZT as *F'*. Two water-resistant PZTs are completely isolated from the fluid flow to reduce the corrosion and degradation effects. The maximum power generated is 25 mW across 100 $\Omega$ resistor at 20 L/min of flow rate and 305 Hz. The resonance frequency can be tuned by altering the beam's length and thickness. The PZT stack can ensure a high fatigue limit and energy density (H. J. Lee, Sherrit, Tosi, Walkemeyer, & Colonius, 2015). A buckled-spring-mass bistable harvester implemented two Rhombus structures, flexure hinge, and mass blocks to capture the vibration energy as shown in Figure 2.26 (b). This architecture allows the energy of the dynamic mass to be transferred and amplified in the Rhombus. It exhibits wide bandwidth and a high power output of 16 mW under an acceleration of 3 m/s$^2$ at 26.5 Hz (Bencheikh et al., 2014; W. Liu, Badel, Formosa, Wu, & Agbossou, 2013a, 2013b).
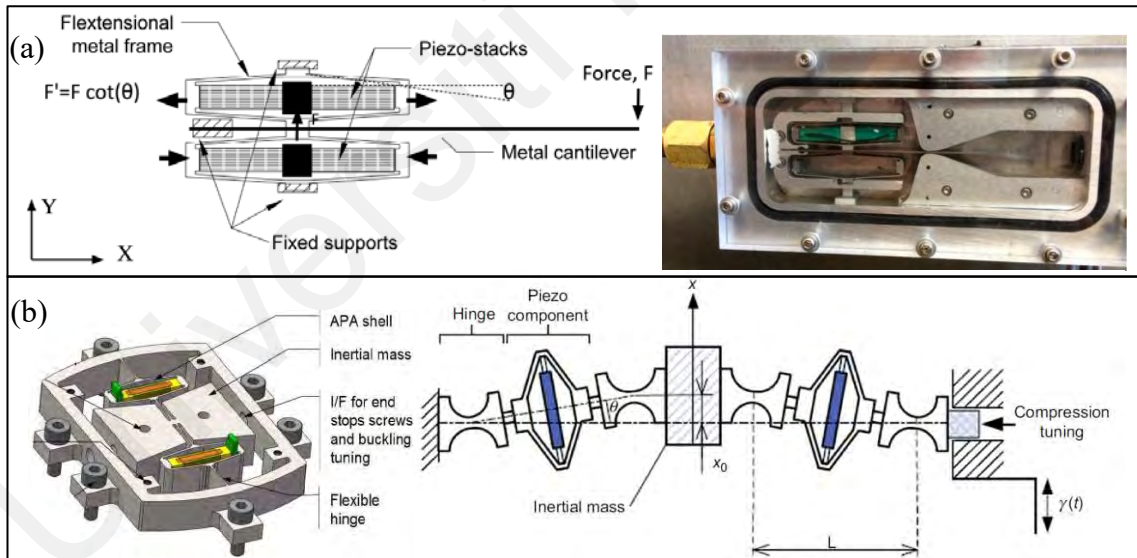


Figure 2.26 (a) Combined structure of Rhombus and cantilever PEH in internal fluid flow (H. J. Lee et al., 2015); (b) Buckled-spring-mass (BSM) bistable harvester (Bencheikh et al., 2014)

### 2.2.3.6 Hybrid Rhombus structure

A Hybrid Piezoelectric Energy Harvesting Transducer (HYPEHT) is designed with an outlook of Rhombus shape with one 33-mode Straight Inner Piezoelectric Multilayer Stack (SIPMS) at the middle and sandwiched by two 33-mode Curved Outer Piezoelectric

Multilayer Stacks (COPMSs) as shown in Figure 2.27 (a) (T.-B. Xu, Jiang, X.,Su, J.,Rehrig, P.W.,Hackenberger, W.S.,, 2008). The piezoelectric multilayer-stacked hybrid actuation/transduction system (stacked-HYBATS) has a different stacking axis of SIPMS which works in 31-mode as shown in Figure 2.27 (b). It yielded 200% and 15% larger displacement than 31 and 33-mode Rhombus transducers (Tolliver, Xu, & Jiang, 2013).
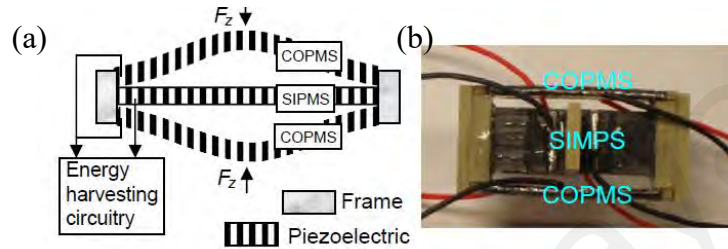


Figure 2.27 (a) The HYPEHT with three 33-mode PZT stacks;
(b) The stacked-HYBATS prototype with one 31-mode SIMPS and two 33-mode COMPSs (T. B. Xu, 2016)

A $35.5 \times 18 \times 10$ mm$^3$ HYPEHT prototype has yielded 19 times more electrical energy output than a same size 31-mode flextensional PEH and 100-1000 times more than a Bimorph PEH with 26% energy conversion efficiency. Hence, the advantages of HYPEHT can be summarized as, firstly, almost all mechanical energy is coupled into the PZT because minimal non-piezoelectric materials are involved in the design. More electrical charges are produced because of the Rhombus force amplification mechanism and the PZT stack. Lastly, the curved 33-mode COPMSs are relatively soft and have a large bending motion which leads to high power output (T.-B. Xu, Jiang, & Su, 2011; T. B. Xu, 2016).

### 2.2.3.7 Bridge

In the Bridge structure, two parallel horizontal hinges of different heights have replaced the slanted hinges in the Rhombus structure as shown in Figure 2.28 (a). The aligned hinges in the Rhombus structure perform better in reducing the maximal stress and withstand a larger force due to its higher stiffness (Mottard & St-Amant, 2009). However,

this high stiffness may reduce the power output as less frame deformation and lower stress are applied at the PZT. Hence, the Bridge structure has comparatively larger deformation with lower stiffness; but it is more widely used in actuators since the area for exciting force acted on the apex of PEH is limited.

On the other hand, Ling et al. (2016) stated that the piezo-actuating force in the Bridge compliant mechanism is along the axis of the flexure hinge which makes it different from the Rhombus structure. A constant moment should be established in the flexure hinge as shown in Figure 2.28 (b). Thus, the Bridge compliant mechanism should not be simply equated to a Rhombus structure when conducting force analysis (Wei et al., 2017). Energy conservation law and the elastic beam theory are employed in the calculation of amplification ratio, $R_{amp}$ with consideration of the translational and rotational stiffness.

$$R_{amp} = \frac{K_l L^2 \tan \theta}{4K_\theta + K_l L^2 \tan^2 \theta} \qquad [2.18]$$
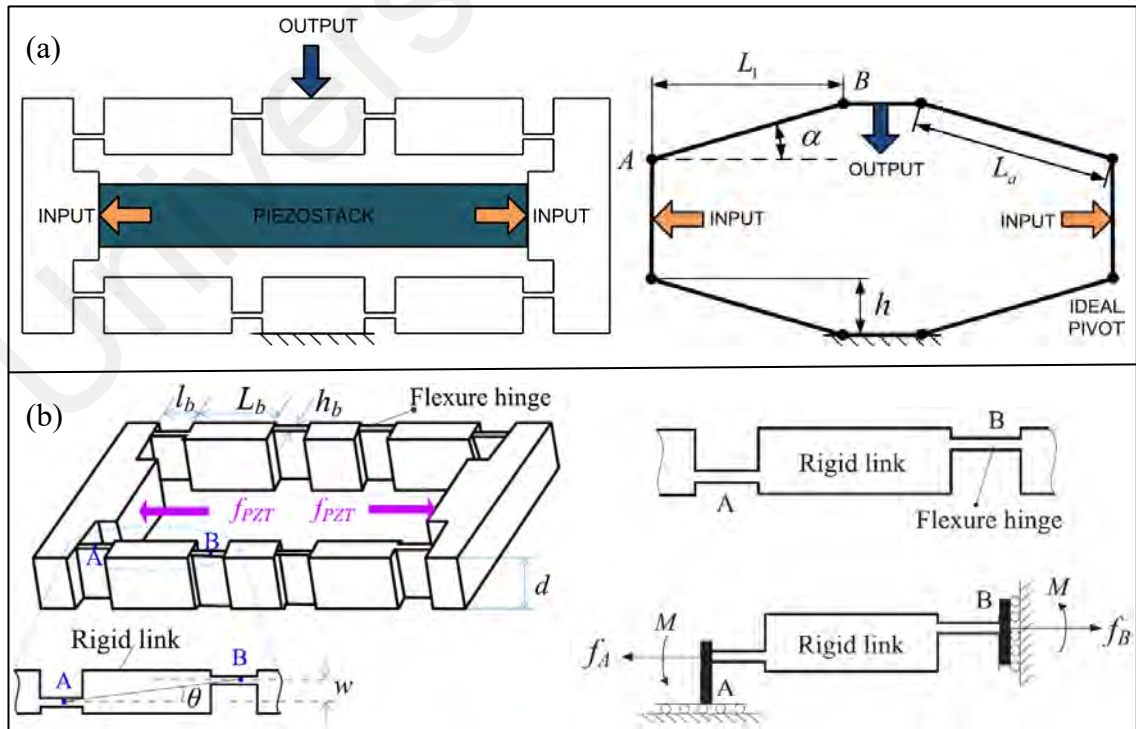


Figure 2.28 (a) The displacement amplification mechanism of a Bridge piezoelectric actuator with its simplified model (Qi, Xiang, Fang, Zhang, & Yu, 2015); (b) The Bridge compliant mechanism with the consideration of moment at the flexure hinge (Ling et al., 2016)

As a conclusion, an inappropriate approximation in which the Bridge compliant mechanism was simplified and equivalent to a Rhombus structure in some previous studies leads to inaccurate kinematic prediction under small designed angles of a compliant mechanism. In particular, the stress concentration effect of the flexure hinges in the Bridge compliant mechanism should be considered for further improving the prediction accuracy of the theoretical model (Ling et al., 2016).

### 2.2.3.8 Compound Bridge

Double flexure arms are designed in a Compound Bridge structure to increase the relatively low stiffness of the conventional Bridge actuator as shown in Figure 2.29 (a). This is because a Compound Bridge with larger lateral stiffness is more suitable for actuator isolation and protection purposes to tolerate the external load. Also, according to practical requirements, more than two bridges can be employed to develop a Compound Bridge transducer to achieve even higher lateral stiffness. Figure 2.29 (b) shows the right-circular (fillet) hinge is adopted to reduce the stress concentration. The corner-filleted hinges can provide better performance in terms of displacement amplification and natural frequencies (Ouyang et al., 2005). The Bridge structure has a displacement amplification ratio of 12 and is widely applied in the actuator (Q. Xu & Li, 2011). By using topology optimization, a Bridge structure can be developed with maximizing output displacement as well (Clark, Shirinzadeh, Pinskier, Tian, & Zhang, 2018). However, topology optimized Bridge structure will cause difficulty in fabrication.
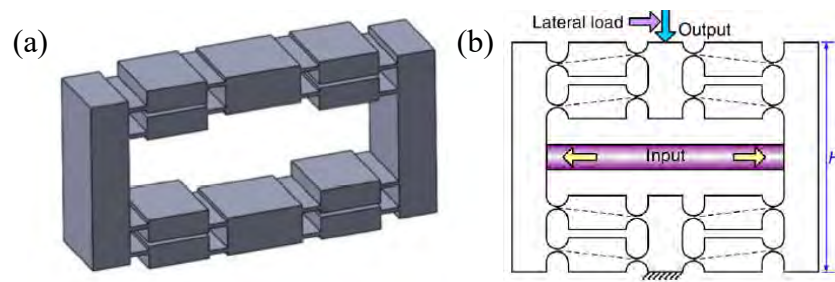


Figure 2.29 (a) Compound Bridge structure with double flexure (double-beams) arms (Choi, Lee, Kim, Lim, & Kwon, 2018); (b) Additional filleted hinge design on the Compound Bridge actuator (Q. Xu & Li, 2011)

### 2.2.4 Flexcompressive Structure

A compressive mode transducer is always preferred as the compressive mean normal stress is beneficial to retard the growth of cracks and increase the fatigue strength (Y.-L. Lee & Barkey, 2012). Flexcompressive or named as Compressive Flexure frame is developed to make the PEH directly work in compression mode as shown in Figure 2.30. This design has the advantage of eliminating the manufacturing complexity, the risks of buckling, and a large potential energy loss. It shows an 8 times greater voltage output and 112 times greater power output compared to a standalone PZT stack (Y. Wang et al., 2016).
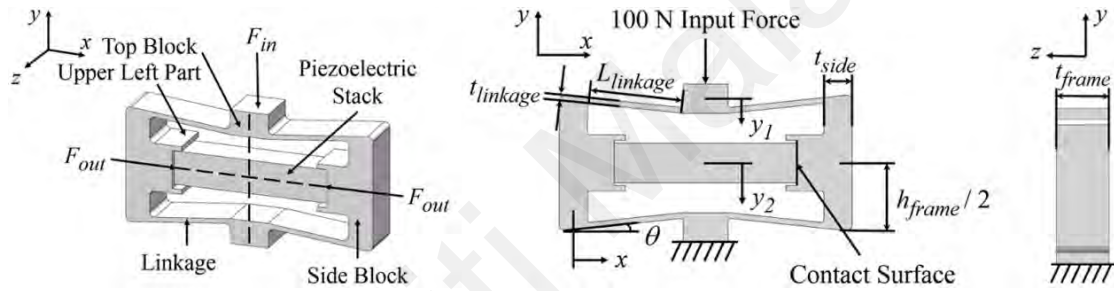


Figure 2.30 Flexcompressive structure with its parameters (Y. Wang et al., 2016)

Another study was carried out to investigate the effect of each parameter on the amplification factor such as the tilt angle, the thickness, and the length of the linkage: $\theta$, $t_{linkage}$, and $l_{linkage}$; the thickness, the height, and the elastic modulus of the frame: $t_{frame}$, $h_{frame}$, and $E_{frame}$; as well as the width of the side block, $t_{block}$. The force amplification ratio will increase with longer and thinner linkages, thicker and shorter side blocks, smaller frame width, or soft frame materials. The thinner, narrower, and longer linkage will enhance its bending deflection causing a larger displacement and contraction of the PZT (W. S. Chen, Wang, & Deng, 2017).

The force amplification ratio of Flexcompressive structure, $k_{amp}$ has been presented in equation [2.19] which considered the nonlinear properties and deformation of the frame. Another two types of flexcompressional frames are compared with the original structure.

Frame I is designed to have longer flexure linkages that enhance the bending deflection and two extended clamping sides for the PZT, while Frame II is larger and consists of two PZT stacks. The two frames have amplification ratios of 8.0 and 8.4, which are higher than the original frame with a 3.5 ratio (W. S. Chen et al., 2017). Frame I is then applied to harvest energy from foot strikes (H. Liu et al., 2019).

$$k_{amp} = \frac{F_{out}}{F_{in}} = \frac{n_1 - n_2}{d_1 + d_2 + d_3 + d_4} \qquad [2.19]$$

where $n_1 = L_{linkage}^3 \cos\theta \sin\theta \, E_{frame}^2 A_{linkage} E_{stack} A_{stack} I_{block}$,
$n_2 = 12 L_{linkage} \cos\theta \sin\theta \, E_{frame}^2 I_{linkage} E_{stack} A_{stack} I_{block}$,
$d_1 = L_{linkage}^3 \sin^2\theta \, E_{frame}^2 A_{linkage} E_{stack} A_{stack} I_{block}$,
$d_2 = 12 L_{linkage} \cos^2\theta \, E_{frame}^2 I_{linkage} E_{stack} A_{stack} I_{block}$,
$d_3 = 12 L_{stack} E_{frame}^3 I_{linkage} A_{linkage} I_{block}$, and
$d_4 = 4 L_{block}^3 E_{frame}^2 I_{linkage} A_{linkage} E_{stack} A_{stack}$.

Another mathematics model of the amplification factor, α has been presented and equals 8 by considering the frame geometry and the stiffness of the PZT stack, $k$ as shown in equation [2.20]. However, it decreases with increasing frequency, which is only 5.1 at 20 Hz as it does not consider the dynamic effects of the structure (M. Evans, Tang, & Aw, 2018). Hence, the developed PEH is suitable for low-frequency energy harvesting such as from human walking as shown in Figure 2.31. Since α is influenced by $k$, the optimization of the frame and PZT stack must be conducted concurrently (Matthew Evans et al., 2019; Ling et al., 2016). The optimal dimensions and amplification ratio of the PEH vary based on the type and amplitude of the input force. For example, with the optimized PZT stack parameters, such as the diameter, thickness, and the number of PZT layer, an increase in power output by a factor of 21 is achieved, from 2.61 mW to 54.8 mW under walking conditions. A factor of 9 is obtained under jogging conditions, from 16.4 mW to 147 mW with the same PZT stack length. In practical, the PEH should be tested based on the worst-case loading condition, where the optimized stack under jogging conditions is

subjected to a walking input. This causes a 28% reduction in the average power output, ending up with 39.1 mW (Matthew Evans et al., 2019).

$$\left(\frac{1}{k} + \frac{L\cos^2\theta}{2E_bA_b} + \frac{L^3\sin^2\theta}{12E_bI}\right)\alpha^2 + \left(\frac{L\sin\theta\cos\theta}{E_bA_b} - (1-\tan\theta)\frac{L^3\sin\theta\cos\theta}{12E_bI}\right)\alpha$$

$$+ \frac{L\sin^2\theta}{2E_bA_b} - \frac{L^3\cos^2\theta\tan\theta}{12E_bI} = 0 \qquad\qquad [2.20]$$
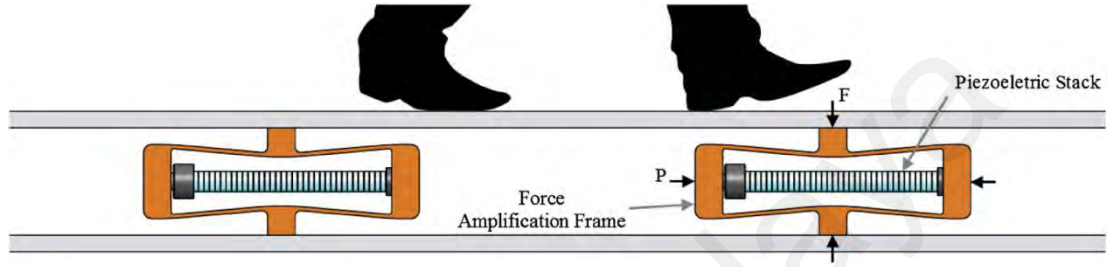


Figure 2.31 Energy harvesting with Flexcompressive structure from human walking (Matthew Evans et al., 2019)

### 2.2.4.1 Compressive Flexure with hinge

Hinge with fillet design is added in a Flexcompressive frame to release the bending constraints between the thick beams and the blocks as shown in Figure 2.32 (a). In this way, the stagnation of bending energy could be mitigated causes the mechanical energy could be efficiently transmitted to the PZT stack with minimum loss. Stack holders are designed to hold the PZT stack in a dynamic environment. The force amplification factor is found to be 8.5. The shoe with fewer PEH can generate more power due to the larger force input to each structure. Six Flexcompressive PEHs in a shoe produce the highest power (14 mW, which is 56% more than that with eight PEHs) if compared to four and eight PEHs (F. Qian, Xu, & Zuo, 2018). Another study applied the hinge design to reduce the energy stored in the inclined beams. Pre-stress is added by having a smaller cavity length for the PZT as shown in Figure 2.32 (b) – (d). The load resistance should match with the internal impedance to obtain the maximum power generation. The FEA displacement ratio of the PEH is 10.13, which is close to the experimental value of 9.50 (Kuang, Chew, & Zhu, 2020).
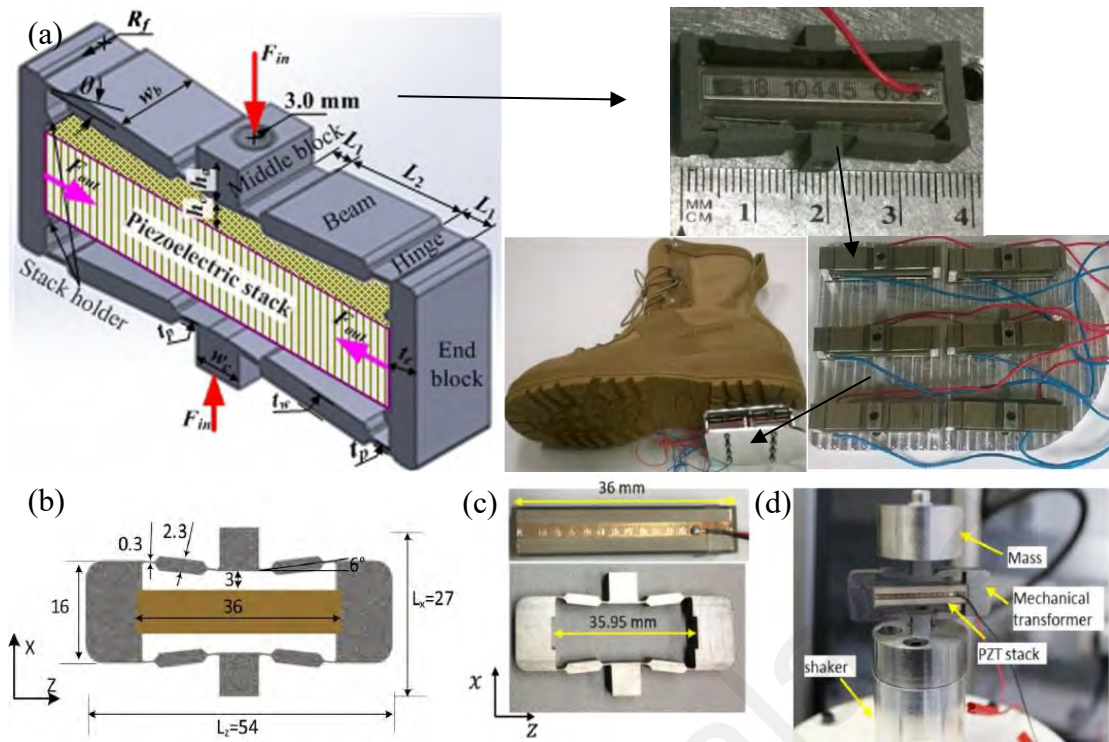
Figure 2.32 (a) A Flexcompressive frame with hinges PEH that fixed into a boot
(F. Qian et al., 2018); (b) Dimensions of the PEH: unit in mm, (c) the fabricated
Flexcompressive structure with shorter cavity length than the PZT, and
(d) experiment setup of the pre-stressed PEH with a proof mass
(Kuang et al., 2020)

Y. Wang et al. (2016) shifted the hinge to the end block and increased the beam thickness. Experiments show that the Flexcompressive structure without hinge design has 8 times greater voltage output and 112 times greater power output than a standalone PZT stack. However, the PEH with hinge design is only 3 times and 17 times more than that of the standalone PZT stack because the flexure-induced increase in input energy is not sufficient to compensate for the potential energy loss stored in the flexures hinge even with the thicker beams. Hence, this type of hinge has poor energy converting efficiency.

### 2.2.5 Multistage Structure

In recent years, researchers tend to further improve the overall actuator or harvester design via multistage force amplification mechanism with either the same type of amplifier frame or a combination of some. A few examples of multistage PEH are discussed in this section.

### 2.2.5.1  Multistage Rhombus structure

A two-stage force amplification mechanism was introduced with a larger vertical Rhombus structure and three horizontal smaller Rhombus frames inside as shown in Figure 2.33 (a). Since the first stage output ends are connected to the input ends of the second stage frame, it is considered as a two-stage amplification mechanism that can capture more energy into the PZT (Tolliver, Jiang, et al., 2013; T. B. Xu, 2016). Rhombus with hinge structure has been used as the second layer amplifier as shown in Figure 2.33 (b) (Ueda et al., 2017). Wen and Xu (2017) utilized two Rhombus frames (one inner and one outer) to obtain a large amplification ratio in compressive mode. They investigate the effect of hinges orientation on the Rhombus structure as shown in Figure 2.33 (c)-(e). The original linkage design shares the stress evenly and reduces the risk of damage, whereas the aligned hinge and parallel hinge can reduce the stiffness of the frame and result in more strain energy. However, the ability to withstand stress is reduced for the structures with hinges design. The original linkage design is selected by considering the safety factor, force amplification, and size of PEH.

Based on the principle of energy conservation, the input energy is equal to the sum of output energy and stored strain energy in the frame. The unconverted stored strain energy can protect the structures from damage. Hence, a compromise between these two kinds of energy is the key to maintain an optimal force amplification ratio and safety factor. This two-stage Rhombus amplifier has a large force amplification ratio of 26 (even it is less than expected as the single outer and inner frames have amplification ratios of 9.54 and 8.88, respectively) and a compact size which is suitable for footstep PEH.
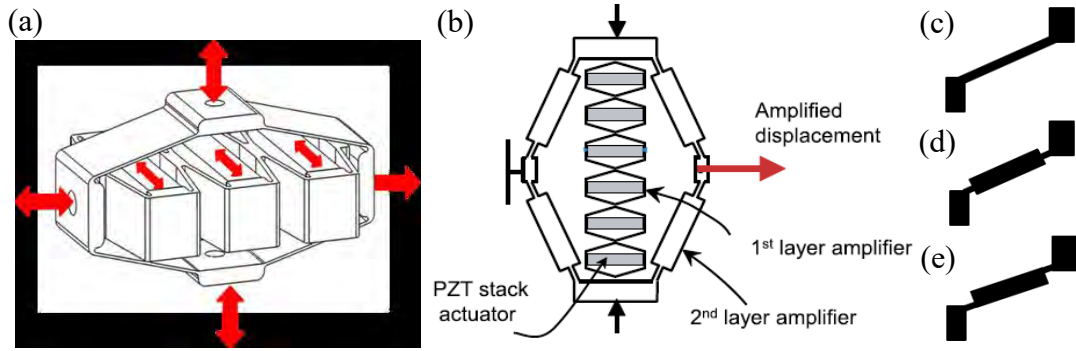
Figure 2.33 Multistage Rhombus structure (a) The inner and outer frames lay in the perpendicular planes (reprinted from (T. B. Xu, 2016), Copyright 2016, with permission from Elsevier); (b) Both the inner and outer frames lay in the same plane (reprinted from (Ueda et al., 2017), Copyright 2017, with permission from Elsevier); (c) Original design; (d) Aligned hinge; (e) Parallel hinge

Double flexure arm compound Rhombus frames are applied to achieve higher stiffness and safety factor (1.23 rises to 2.94) with a little scarification on the amplification ratio (22.62 reduces to 17.90). The total force amplification ratio, $\acute{N}$ is the multiplication of the inner and outer structure's amplification factors where $\acute{N} = \eta \acute{N}_{outer\ frame} \acute{N}_{inner\ frame}$. The force transmission coefficient, $\eta$ is equaled to 0.85, which is calculated from the FEA amplification factors, i.e., 17.9/(4.74 × 4.33). The maximum power of the PEH is 203 times over the standalone PZT stack (Wen et al., 2018).

### 2.2.5.2 Multistage Flexcompressive structure

L. Wang et al. (2016) used three Flexcompressive structures with hinge design as the inner frame and one larger Flexcompressive structure as the outer frame to avoid the potential buckling failure in compression loading. Since there is strain energy stored in the frame, the magnification effect should consider both the force amplification ratio and the energy transmission efficiency (ratio of strain energy in the PZT and the total strain energy in the whole PEH). The two-stage Flexcompressive PEH has demonstrated a total of 20.8 times force amplification ratio and 18% energy transmission ratio, where 7.8 times force amplification and 24% energy transmission ratio are contributed by the inner frame, the rest is contributed by the outer frame. The power density is 127 times more than a standalone PZT stack.

Feng Qian et al. (2019) then applied the two-stage Flexcompressive amplifier in a shoe heel to achieve an autonomous power supply for wearable sensors and low-power electronics as shown in Figure 2.34. The two-stage force amplification frames magnify the dynamic forces and transfer them to the PZT stacks with minimum energy loss. The actual force amplification factor is found less than the simulated value of 12.8 and decreases with the increment of the loading force. This is due to the change in tilt angles of the beams and the stiffness of the PEH is not linear at large deformations. Hence, the analytical model is not accurate if it does not consider the large deformation and nonlinearity.
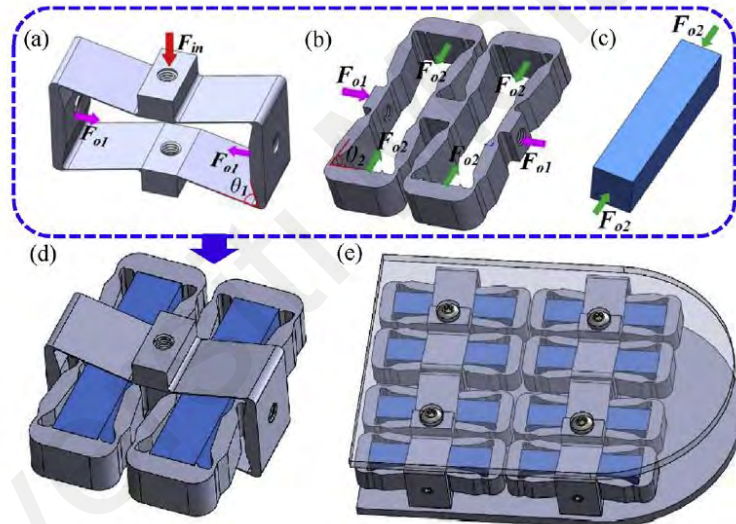


Figure 2.34 (a) Flexcompressive outer frame; (b) Two series-connected Flexcompressive structures with hinge design as the inner frame; (c) d33 PZT stack; (d) Two-stage Flexcompressive structure; (e) Configuration of the PEH in a shoe heel (Feng Qian et al., 2019)

The two-stage compound Flexcompressive structure has a lower safety factor of 1.57 and an amplification ratio of 10.07 if compared to the two-stage compound Rhombus structure (2.98 and 15.21). This is because the amplified input force in the outer Flexcompressive structure reduces the output displacement and limits the amplification factor of the inner frame due to the law of conservation of energy (Wen et al., 2018).

### 2.2.5.3 Integrated multistage amplifier

Wen and Xu (2019) introduced an underground integrated four-stage PEH to scavenge energy from human footsteps using a wedge mechanism, leverage mechanism, Flexcompressive structure, and Rhombus structure as shown in Figure 2.35 (a). The vertical input motion of the top plate is converted by the wedges to an amplified horizontal output motion. A larger forcing area is provided by having a top plate to withstand a larger load safely. Experimental results show that the harvester exhibits a large force amplification ratio of 17.9 and high peak power output of 50.8 mW across a matched resistor.

Z. Wu and Xu (2019) introduced a PEH which utilized the bidirectional friction force produced between footstep and harvester. A Rhombus structure is combined with a selectivity lever (SL) which is composed of a lever mechanism and position limiters to utilize both pull and push inputs as shown in Figure 2.35 (b) and (c). The lever mechanism is adopted to change the direction of input force, and position limiters are employed to distinguish between pull and push inputs. The FEA force amplification ratios are 12.20 and 13.14 under the pull and push input, respectively. The maximum average output power is 128.51 µW under back-and-forth input, which is 313.44 times higher than the PZT alone.
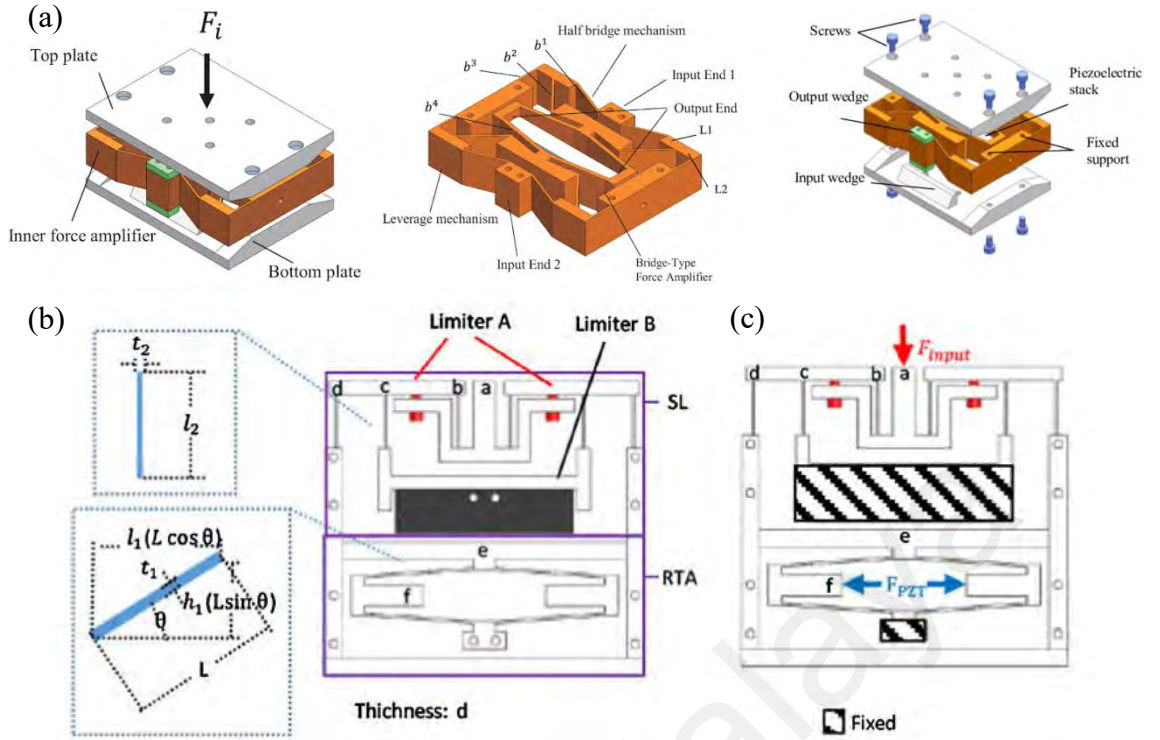
Figure 2.35 (a) Integrated four-stage force amplifier (Wen & Xu, 2019); (b) Two-stage bidirectional Rhombus structure PEH and (c) the schematic mechanism under push input (Z. Wu & Xu, 2019)

### 2.2.6 Comparison of the Energy Harvesting Performance and the Amplification Ratio for Various Amplifier Structures

In this section, the energy harvesting performance and the amplification ratio of various amplifier structures have been compared and discussed. Table 2.2 summarizes the excitation force, piezoelectric material, dimensions, output power, output voltage, optimum resistance, and application of different structures PEH described herein. A summary of the amplification factor based on the analytical theory has been presented in Table 2.3.

A direct comparison of the power output of PEHs with various amplifier structures has been made to evaluate their energy harvesting performance. However, the high power output may be due to a larger piezoelectric used in the PEH. Hence, it is fair to compare the PEH with the calculated power density per unit of piezoelectric volume. Figure 2.36 shows the power output and the calculated power density of each type of PEH under 0 –

2,500 Hz. It is noted that most of the PEH work under 200 Hz of excitation frequency to match with the vibration-based energy sources available in our surroundings. For instance, the commercial and industrial machines have around 120 Hz of vibration source, HVAC vents are around 60 Hz while human body movements, roadway pavement, bridge, and railways are <10 Hz (Siddique, Mahmud, & Heyst, 2015).

Figure 2.36 shows that the cantilever structure is widely tuned and utilized under the frequency of 20 – 80 Hz. The Cymbal PEH is comparatively more flexible to be designed under various frequencies among all the structures, whereas the Rhombus, Flexcompressive, and multistage structures focus on low-frequency vibration source, which is below 10 Hz. Since the power harvesting from footsteps occurs at a very low frequency which is close to 1 Hz (Shenck & Paradiso, 2001), many flexure structures show their implementation potential in this application. Moreover, the standalone PZT stack shows a capability to work under extremely high excitation frequency, around 2,500 Hz.
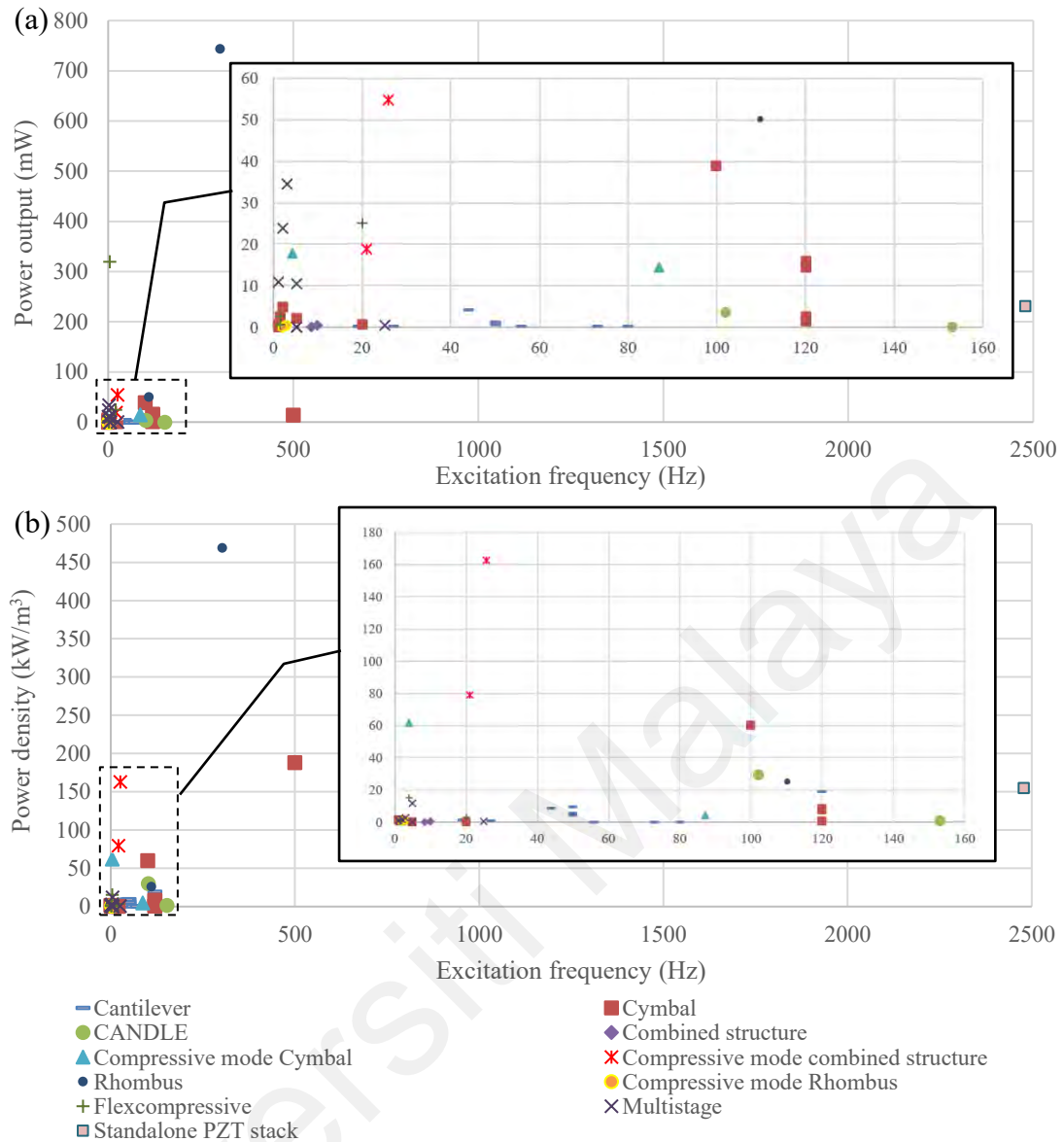
Figure 2.36 Graph of (a) power output and (b) power density against the excitation frequency for different types of amplifier structure PEH

Other than the excitation frequency, the applied force and electronics used on the PEH should be aware when comparing the power level of different PEHs (Palosaari et al., 2012). Figure 2.37 (a) presents the plot of power density by the excitation frequency and the applied force. Figure 2.37 (b) shows that the PEH is designed to have greater power output by either targeting the higher loading environment or the higher frequency vibration source. All of the structure, except for the cantilever, is designed and tested under higher loading force. Closer views with lesser overlapping points for the Cymbal and multistage structure are shown in Figure 2.37 (d) and (e). The multistage structure is

frequently implemented in low frequency but high loading force environments, while the

Cymbal is the most commonly applied structure.
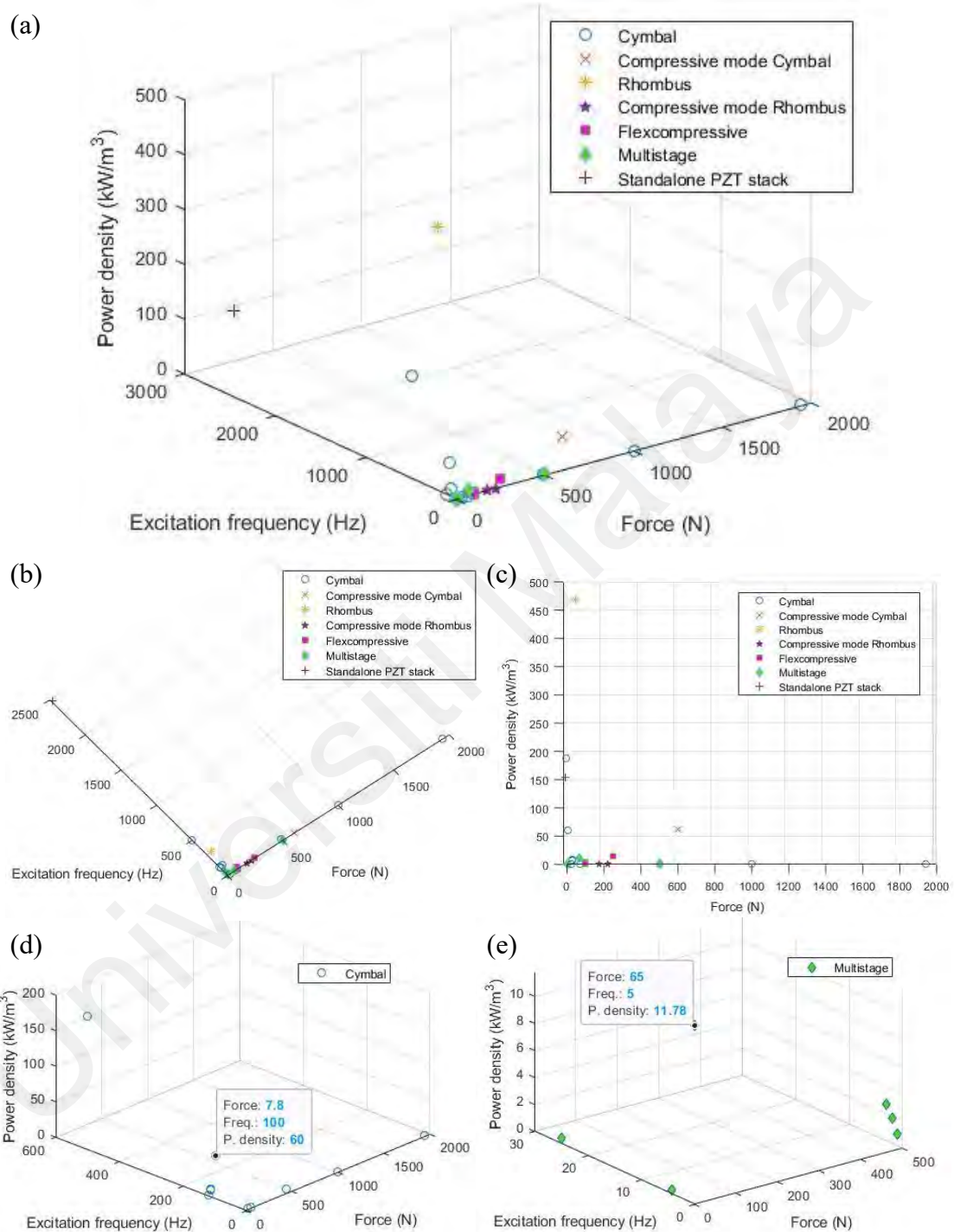


Figure 2.37 (a) 3D plot of power density with the excitation frequency and the applied force for various PEHs, (b) the xy-plane, (c) the yz-plane, (d) the 3D plot for Cymbal structure and (e) the 3D plot for multistage structure

Figure 2.38 presents the power density of PEH under the acceleration source of less

than 3 $g$. The cantilever structures show a comparatively low power density (<20 kW/m$^3$)

as they are excited under a low vibration amplitude and medium range of frequency. This is because the cantilever robustness is insufficient to withstand higher cyclic force and stress. Hence, the combined cantilever and flextensional structures have higher power density as they utilize the high force amplification factor and robustness of flextensional structure to increase the load capacity in the high force environment.
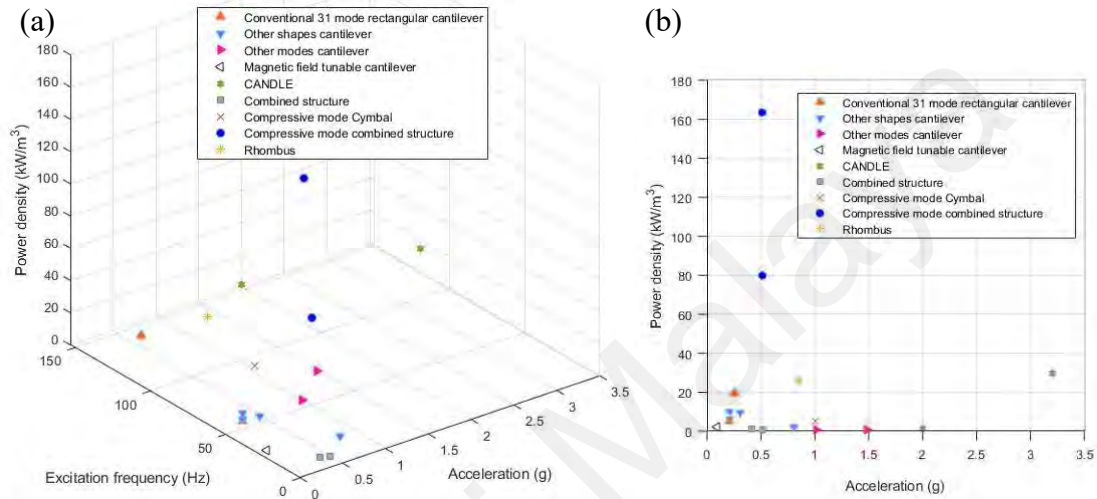


Figure 2.38 (a) 3D plot of power density with the excitation frequency and the acceleration for various PEHs and (b) the yz-plane

Table 2.3 summarizes the equation of amplification ratio, the variable and theory used, the analytical, FEM, and experimental amplification ratio for different structures PEH. The elastic beam theorem and kinematic analysis on the flexure arm are the basic theory to apply in the model. It is noticed that the force amplification ratio has been up to 20 by using the multistage structure in a PEH, whereas a 112 power amplification ratio has been achieved using a Flexcompressive structure. A maximum of 12 displacement amplification ratio has been obtained experimentally with a Bridge or Rhombus structure. Generally, the displacement amplification ratio is slightly greater than the force amplification ratio (as shown in the Rhombus structure), while the amplification ratio which is calculated based on the power variable has the greatest value among all. In other words, an amplifier structure will have a different scale of increment in these variables even under the same input condition.

Thus, it is unfair to directly compare based on the value of the measured amplification ratio for different structures. This is because the amplification ratio is computed based on different input and output variables for different studies, such as power, voltage, force, displacement, and energy. Furthermore, various theories have been used and different constraints have been considered when generating the analytical equation for the amplification ratio. Hence, the comparison should be made using the same variable under similar constraints.

In summary, the cantilever structure is suitable for broadband energy harvesting from mechanical vibration, but not a high force environment due to its fragile characteristics. The PZT stacking design increases the load capacity and the power output by utilizing the PZT's 33-mode. The flexure structure has been widely developed as it has higher stiffness, load capacity, and amplification factor. The derivatives of flextensional structures such as the compound beam will increase the stiffness of the structure, whereas the hinge design will mitigate the stagnation of bending mechanical energy in the frame. The fillet design will reduce stress concentration. A compressive mode PEH is always preferred due to the larger compressive yield strength of a PZT. Many designs have been proposed, such as fixing the PZT outside of the flextensional frame, applying a pulling force on the flextensional structure, or using a multistage flextensional frame to activate the compression mode in the PZT. However, it will lead to a bulky design and is impractical for those applications where pulling force is absent. Hence, the Flexcompressive structure has better overall performance as it utilizes the 33-mode parallel-connected PZT stack in a direct compressive way. The combined structures have a wider bandwidth with the adopted cantilever structure, while the multistage structure can achieve a greater amplification effect which should be implemented in future design.

Table 2.2 A summary of the performance based on the power output for various PEH structures

| Amplifier structure | PZT material | PZT's dimension (mm) | Loading force/Pressure/ Acceleration | Freq. (Hz) | Avg. Power (mW) | Power density (kW/m³) | Voltage (V) | Load (Ω) | Application [reference] |
|---|---|---|---|---|---|---|---|---|---|
| Rectangular cantilever | PZT-5H (Piezo Systems Inc.) | (11×3.2×0.28) ×2 pieces | 0.25$g$ | 120 | 0.375 | 19.02* | 14 | 250k | Vibration-based PEH (VPEH) for radio transmitter (Roundy & Wright, 2004) |
| Triangular cantilever | PZT-5H | Trapezoid: $w_{root}$ = 20, $w_{tip}$ = 10, $l$ = 10, $t$ = 0.07 | 0.8mm displacemnet | 80 | 0.0015 | 0.14* | 1 | 333k | VPEH (Glynne-Jones et al., 2001) |
| Rectangular cantilever | PSI-5A4E PZT (Piezo Systems Inc.) | (25×14×0.2) ×2 pieces | FEA: 0.2$g$; 10g proof mass | 50 | 0.630* | 4.5 | 54 | Open circuit | VPEH (Benasciutti et al., 2009) |
| Tapered cantilever | | ($w_{root}$ = 20.2, $w_{tip}$ = 6.73, $l$ = 26, $t$ = 0.2) ×2 pieces | | | 0.784* | 5.6 | 60.3 | | |
| Reverse tapered cantilever | | ($w_{root}$ = 7, $w_{tip}$ = 23.84, $l$ = 22.7, $t$ = 0.2) ×2 pieces | | | 1.344* | 9.6 | 72.6 | | |
| Zigzag cantilever | PZT-5H | 45×15×0.2 | 0.8$g$ | 19 | 0.18 (peak) | 1.33* | 16 (peak) | 10k | VPEH for wireless switch (T. Ma et al., 2019) |
| Arc-shaped PZT cantilever | PZT-5H | Arc-shaped: ($Ø_{outer}$ = 20, $Ø_{inner}$ = 19.5, w = 15, t = 0.5) ×2 pieces | 0.3$g$ | 44 | 4.08 | 8.88* | 29 (peak-to-peak) | 100k | PEH (Yang, Wang, et al., 2017) |
| Standalone PZT stack | PZT d33 stack: Navy Type II Ceram Tec SP505 (SP505 stack) | 1 stack: 300 PZT layers = 7×7×32.34 | 11.6$N_{rms}$ (resonance mode) | 2479 | 231 | 154.5 | 2.9$V_{rms}$ | 1M | (T.-B. Xu, Siochi, et al., 2011) |
| | | | 40.0$N_{rms}$ (off-resonance mode) | 680 | 18.7 | 11.8 | - | 1M | |
| Barbell-shaped cantilever | d33 BiScO₃-PbTiO₃ ceramic | 1 ring stack: $Ø_{outer}$ = 21, $Ø_{inner}$ = 8, $t$ = 20 | 1$g$ | 56 | 0.00476 | 0.0008* | 8 | 2.1M | High temperature VPEH (J. Wu et al., 2016) |
| Rectangular cantilever | d15 PZT-51 (Baoding HengSheng Acoustics Electron Apparatus Co. Ltd Baoding) | (13.0×2.5×1.0) ×2 pieces | 1.48$g$ | 73 | 0.0087 | 0.13* | 12.4 (peak-to-peak) | 2.2M | (J. Zhao et al., 2012) |
| Magnetic field tunable cantilever | PZT (APC International Ltd) | (34×20×0.16) ×2 pieces | 0.08$g$ | 22-32 | 0.24-0.28 | 1.19* | - | 26k | VPEH (Challa et al., 2008) |
| Moonie | PZT-5H | Ø = 32, $t$ = 2 | FEA: 0.7MPa | - | 0.012mJ | - | 44.9 | - | (H. Zhao et al., 2012) |
| Cymbal | | | | | 0.489mJ | | 284.2 | | |
| Cymbal | D210 PZT (Dongil Technology, Korea) | Ø = 29, $t$ = 1 | 7.8N | 100 | 39 | 60 | - | 400k | VPEH (H. W. Kim et al., 2004) |
| | Noliac NCE51 and PiCeramics PIC 141 | Ø = 30, $t$ = 1 | 0.9MPa | - | 0.016 | 0.023* | - | 1M | Roadway PEH (Moure et al., 2016) |
| | PZT -5A | Ø = 35, $t$ = 4 | 8.15N | 120 | 1.40 | 0.36* | - | 410k | VPEH (J. Yuan et al., 2010) |
| | Radially layered PZT-5H (d31) | $Ø_{outer,1}$ = 50, $Ø_{inner,1}$ = 40, $Ø_{outer,2}$ = 30, $Ø_{inner,2}$ = 20, $t$ = 5 | 500N | 20 | 0.92 | 0.17* | 52.8 (open circuit, 100MΩ) | 0.8M | Roadway PEH (X. Liu & Wang, 2019) |
| Cymbal with Unimorph | PZT-5H | Ø ≈ 25, $t$ = 0.191 | 1940N | 1 | 0.121 | 1.29* | - | 3.3M | Underfloor/Roadway PEH (Mo et al., 2013) |

Table 2.2, continued: A summary of the performance based on the power output for various PEH structures

| Amplifier structure | PZT material | PZT's dimension (mm) | Loading force/Pressure/Acceleration | Freq. (Hz) | Avg. Power (mW) | Power density (kW/m³) | Voltage (V) | Load (Ω) | Application [reference] |
|---|---|---|---|---|---|---|---|---|---|
| Slotted Cymbal (18-fringe) | PZT-5H | Ø = 35, $t$ = 2 | 30N | 120 | 14.5 | 7.54* | 85 | 520k | (J.-b. Yuan et al., 2009) |
| Slotted Cymbal (18-cone) | | | | | 16 | 8.32* | 90 | 500k | |
| Slotted Cymbal (circumferential) | PZT -5A | Ø = 35, $t$ = 4 | 8.15N | 120 | 2.5 | 0.65* | - | 400k | VPEH (J. Yuan et al., 2010) |
| Rectangular Cymbal | PMN-PT single crystal $0.71Pb(Mg_{1/3}Nb_{2/3})O_3$-$0.29PbTiO_3$ | 26.6×4×0.7 | 0.55N | 500 | 14 | 188 | 45.7 (peak) | 74k | VPEH (Ren et al., 2010) |
| Rectangular Cymbal | PZT-5H | 32×32×2 | 0.7MPa | - | 1.13mJ | - | FEA: 382.0 | - | (H. Zhao et al., 2012) |
| | | | | 1 | - | | 168.8 | | |
| Rectangular Cymbal | | 30×20×2 | 0.7MPa | 10 | - | - | 168.8 | - | (Zhao et al., 2015) |
| Arc Rectangular Cymbal | | | | | - | | 230 | | |
| Arch Rectangular Cymbal | | | | | 0.6mJ | | 286 | | |
| Arch Rectangular Cymbal | | | 0.75MPa @2.5m/s | - | - | - | 202 | - | Roadway PEH (Zhao et al., 2018) |
| Arch Circular Cymbal | PZT-5H (Morgan Electro Ceramics) | Ø = 3, $t$ = 0.5 | 24.8N | 1.19 | 0.66 | 1.37 | 82 (peak) | 2.6M | Footstep PEH (Palosaari et al., 2012) |
| Rectangular Cymbal (dual substrates) | DL-53HD PZT (Del Piezo Specialities) | 52×30×4 | 1kN | 2 | 4.68 | 0.75* | - | 6.6M | Shoes PEH (Kuang et al., 2017) |
| | | | 4.8km/h | 1.4 | 2.5 | 0.40* | 180 (peak) | 2M | |
| Rectangular Cymbal | PZT-5X d33 stack (Sinocera, State College, PA) | 1 stack: 7 PZT layers = 32×32×2 | 0.7MPa | - | 0.743 mJ | - | 556 | Open circuit | Roadway PEH (Jasim et al., 2017) |
| | | 64 stacks | 70kPa | 5 | 2.1 | 0.0023* | - | 400k | |
| CANDLE (Rectangular Cymbal) | PMNT (0.71PMN-0.29PT) | 25×5×1 | 3.2$g$ | 102 | 3.7 | 29.6 | 38 (peak) | 251k | VPEH (C. Xu, Ren, Di, et al., 2012) |
| CANDLE (Circular Cymbal) | PZT-5H d31 stack | (Ø = 12.7; $t$ = 0.5) ×2 disks | 2$g$ | 153 | 0.1416 | 1.12* | 2.38 | 40k | VPEH (Tufekcioglu & Dogan, 2014) |
| Combined structure (3 Rectangular Cymbals & Cantilever with magnet stoppers) | PZT-5H (d31) | (40×10×0.8) ×3 pieces | 0.4$g$ | 9.9 | 0.387 (peak) | 0.40* | - | 390k | VPEH (Zou et al., 2017) |
| | | | 0.5$g$ | 8.5 | 0.0295 | 0.03* | | | |
| Compressive mode Rectangular Cymbal | PZT-4 d33 ring stack | (1 stack: 10 PZT rings Ø$_{outer}$ = 15, Ø$_{inner}$ = 5, $t$ = 10) ×2 stacks | 1$g$ | 87 | 14.6 | 4.65* | 111 (peak-to-peak) | 40k | Footstep PEH (Xiaotian Li et al., 2011) |
| | PZT d33 stack | (20×20×36) ×2 stacks | 600N | 4 | 17.8 | 61.81* | - | 120k | (X. Wang et al., 2016) |
| Compressive mode combined structure (Rectangular Cymbal & cantilever) | PZT-5A | 32×15×0.5 | 0.5$g$ | 21 | 19 (peak) | 79.17* | - | 300k | VPEH for WSN (Yang & Zu, 2014) |
| | PZT-5H | 32×15×0.7 | 0.5$g$ | 25.7 | 54.7 (peak) | 162.80 | - | 100k | VPEH (Yang et al., 2015) |

Table 2.2, continued: A summary of the performance based on the power output for various PEH structures

| Amplifier structure | PZT material | PZT's dimension (mm) | Loading force/Pressure/ Acceleration | Freq. (Hz) | Avg. Power (mW) | Power density (kW/m³) | Voltage (V) | Load (Ω) | Application [reference] |
|---|---|---|---|---|---|---|---|---|---|
| Rhombus | PZT d33 stack: APA 400M-MD | 2 stacks ≈ 40×7×7 | 0.85g | 110 | 50 | 25.51* | - | 2k | VPEH, Self-powered AM transmitter (Sosnicki et al., 2006) |
| | (SP505 stack) | 32.4×7×7 | 50N | 303 | 744* | 468.63* | 12.5 | 1M | (W. Zhou & Zuo, 2013) |
| Compressive mode Rhombus with hinges | PZT d33 stack | 1 stack: 130 PZT layers = 16 ×5×5 | 220N | 2.75 | FEA: 0.4 | 1.00* | - | 19.2k | Backpack PEH (Feenstra et al., 2008) |
| | | | 176N | 2 | 0.176 | 0.44* | | | |
| Flexcompressive | PZT d33 stack (P-113-00) | 1 stack: 250 PZT layers Ø = 10, $l$ = 42 | 53.57N (peak) | - | 6.97 (peak) | 2.11* | 18.68 (peak) | 70k | Shoes PEH (Y. Wang et al., 2016) |
| | PZT-4 d33 ring stack | 1 stack: 12 PZT rings Ø$_{outer}$ = 15, Ø$_{inner}$ = 8, $l$ = 62 | 100N | 20 | 24.9 (peak) | 3.18* | 240 | 2.3M | (M. Evans et al., 2018) |
| | PZT d33 ring stack | 1 stack: Ø = 13, $l$ = 160 | 250N | 4 | 320 | 15.07* | 17.9V$_{rms}$ | 1k | Underfloor PEH (Matthew Evans et al., 2019) |
| Flexcompressive | (SP505 stack) | 32.34×7×7 | 100N | 1.4 | 0.65 2.00 (peak) | 0.41* 1.26* (peak) | - | 50k | (W. S. Chen et al., 2017) |
| Flexcompressive with longer linkage | | | | | 2.7 7.7 (peak) | 1.70* 4.86* (peak) | | | |
| Flexcompressive with hinge | | 6 stacks | 4.8km/h | - | FEA: 9.0 | 0.95* | 5.8V$_{rms}$ | 3.6k | Shoes PEH (F. Qian et al., 2018) |
| | | | | | Exp: 8.5 | 0.89* | 5.5V$_{rms}$ | | |
| Two-stage compound Rhombus | PZT d33 stack: P-885.91 (Physik Instrumente (PI) Co., Ltd.) | 1 stack = 36×5×5 | 2.33N | 25 | 0.341 | 0.38* | - | 2k | Footstep PEH (Wen et al., 2018) |
| Two-stage Rhombus & lever | PZT d33 stack: RP150 Harbin Soluble Core Tech Co., Ltd. | 1 stack = 28×5×5 | 10N (Push input) | 5 | 0.067 | 0.096* | 2.92 (peak-to-peak) | 12k | (Z. Wu & Xu, 2019) |
| | | | 10N (Pull input) | 5 | 0.055 | 0.079* | 2.58 | 11k | |
| Two-stage Flexcompressive (1 outer, 3 inner frames) | (SP505 stack) | (32.34×7×7 ) ×3 stacks | 100g proof mass | 37 | - | 2642mW/g² | - | 1.722k | (L. Wang et al., 2016) |
| Two-stage Flexcompressive (4 structures: 1 outer, 2 inner frames) | | 8 stacks | 500N (FEA) | 3 | 34.3 | 2.71* | - | 1.6k | Shoes PEH (Feng Qian et al., 2019) |
| | | | 500N | 2 | 23.9 | 1.89* | | 2.4k | |
| | | | 500N | 2 | 11.0 | 0.87* | | 5.1k | |
| | | | 4.8km/h | - | 10.4 | 0.82* | | - | |
| Four-stage Rhombus, Flexcompressive, wedge & lever | PZT d33 stack: P-885.91 (PI) | 1 stack = 36×5×5 | 82.29N (one complete press-and-release cycle) | - | 34.81 (peak) | 38.68* | 26.39 | 20k | Floor tile PEH (Wen & Xu, 2019) |
| | | | 65N | 5 | 10.6 | 11.78* | - | 10k | |

* *denotes calculated value*

Table 2.3 A summary of the amplification factor based on the analytical theory for various structures

| Variable | Theory & equation | Amplification ratio | | | | Reference |
|---|---|---|---|---|---|---|
| | | Structure | Analytical | FEM | Experiment | |
| Energy | Energy transmission coefficient *refer equation [2.13] | Moonie | - | 0.012 | - | (H. Zhao et al., 2012) |
| | | Cymbal | - | 0.015 | - | |
| | | Rectangular Cymbal | - | 0.037 | - | |
| Force | Kinematic principle $R = \dfrac{F_{output}}{F_{input}} = \cot\theta$ | Rectangular Cymbal, Rhombus | Varies based on the inclined angle, $\theta$ | - | - | (Kuang et al., 2017; Xiaotian Li et al., 2011; H.-W. Ma et al., 2006) |
| | $R_{total} = \dfrac{F_{output}}{F_{input}}$ | 4-beam compound Rhombus | - | 3.88 | - | (Wen et al., 2018) |
| | | Two-stage compound Flexcompressive | - | 10.07 | - | |
| | Compatibility condition theorem *refer equation [2.19] | Flexcompressive | 3.4 | 3.7 | 3.5 | (W. S. Chen et al., 2017) |
| | | Flexcompressive with longer linkage | 8.1 | 8.2 | 8.0 | |
| Force & voltage | Elastic beam theory $R_{total} = \dfrac{F_{output}}{F_{input}} = \eta \times R_{first\ stage} \times R_{second\ stage}$ | Two-stage Rhombus | - | 26 | - | (Wen & Xu, 2017) |
| | | | - | 22.62 | - | (Wen et al., 2018) |
| | | Two-stage compound Rhombus | - | 17.9 | 17.5 | (Wen et al., 2018) |
| | Kinematic principle for ideal case Theory: $R_{total} = R_{first\ stage} \times R_{second\ stage}$; $R = \cot\theta$ FEA: $R_{total} = \dfrac{F_{output}}{F_{input}}$ Experiment: Ratio of the gradients (from graph of output voltage against input force) for the developed PEH over the standalone PZT | Two-stage Flexcompressive (1 outer, 3 inner frames) | - | 21 | 20.8 | (L. Wang et al., 2016) |
| | | Two-stage Flexcompressive (4 structures: 1 outer, 2 inner frames) | - | 12.8 | 9.2 @80N 4.5 @500N | (Feng Qian et al., 2019) |
| | | Four-stage Rhombus, Flexcompressive, wedge & lever | 13.05 @3.7° | 18.83 | 17.90 Deviation<10% | (Wen & Xu, 2019) |
| Displacement | Beam theory and kinematic analysis *refer equation [2.16] | Rhombus | 9.47 | 6.2 | - | (Shao et al., 2014) |
| | Kinematic principle and elastic beam theory *refer equation [2.17] | Rhombus | 9 @3.2° | 8 @3.2° | - | (Ling et al., 2016) |
| | | | 13.05 @3.7° | - | Deviation<10% | |
| | $R_{amp} = \dfrac{\Delta y_{output}}{\Delta x_{input}}$ | Rhombus with hinge | 9 | 9 | Deviation<7% | (H. Zhou & Henson, 2007) |
| | | | - | 10.9 | - | (Feenstra et al., 2008) |
| | | Bridge | 12.86 | 11.95 | 12.44 | (Wei et al., 2017) |
| | Kinematic principle and elastic mechanism $R_{amp} = \dfrac{l_a \cos\theta}{\cos\alpha \frac{t^2 \cos\theta}{6l_a \sin\theta} + l_a \sin\theta}$ | Rhombus/ Bridge | 44 @0.8° | 19 @1.3° | - | (H.-W. Ma et al., 2006) |
| | | | 18.819 | 15.43 | 12.025 | (Qi et al., 2015) |
| Power | $R_{amp} = \dfrac{P_{developed\ PEH}}{P_{standalone\ PZT}}$ | Flexcompressive | - | - | 112 | (Y. Wang et al., 2016) |
| Power & voltage | Elastic beam theory *refer equation [2.20] | Flexcompressive | 8 | 8 | 52 (power) 7.2 (voltage) | (M. Evans et al., 2018) |

## 2.3 Parameters that Influencing the Performance of PEH with Rectangular Cymbal Structure

In this section, some important parameters that govern the performance of the amplification factor of the structural design will be discussed. The basic flextensional structure, Rectangular Cymbal will be considered in this section which is developed by Kuang et al. (2017) via FEA as shown in Figure 2.39. The dimensions of the model are listed in Table 2.4.
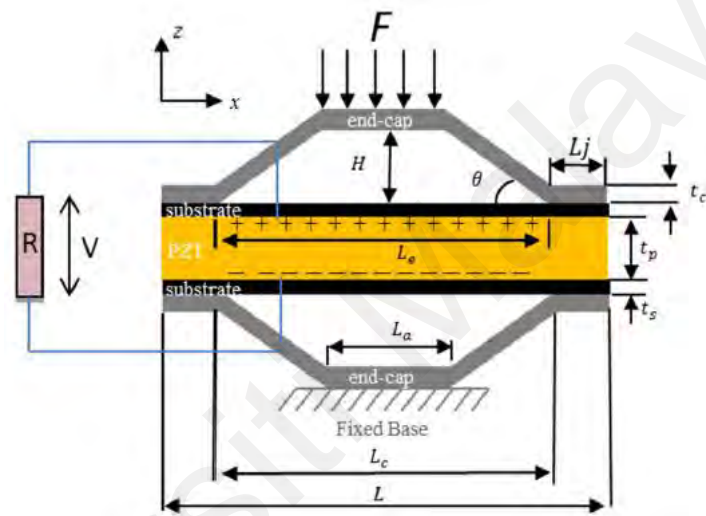


Figure 2.39 Rectangular Cymbal structure PEH (Kuang et al., 2017)

Table 2.4 Dimensions of Rectangular Cymbal structure used in the simulation
(Kuang et al., 2017)

| Dimensions | Symbol | Initial value | Lower limit | Upper limit |
|---|---|---|---|---|
| Total length (mm) | $L$ | 52 | - | - |
| Width (mm) | $W$ | 30 | - | - |
| PZT thickness (mm) | $t_p$ | 4 | 0.5 | 9 |
| End cap thickness (mm) | $t_c$ | 2 | 0.3 | 3 |
| Substrate thickness (mm) | $t_s$ | 0.6 | 0.2 | 0.9 |
| Cavity height (mm) | $H$ | 3.5 | 1 | 13 |
| Cavity length (mm) | $L_c$ | 40 | - | - |
| Apex length (mm) | $L_a$ | 14 | - | - |
| Joint length (mm) | $L_j$ | 6 | 2 | 10 |
| Electrode length (mm) | $L_e$ | 40 | 25 | 52 |
| End cap angle (°) | $\theta$ | 15 | 4.4 | 45 |

### 2.3.1    Effects of the Addition of Substrate and Its Thickness, $t_s$

From the simulation results done by Kuang et al. (2017), it had been revealed that the presence of two layers of the substrate is able to increase the load capacity of a PEH by shifting the stress concentration to the substrate instead of the PZT as mentioned in Section 2.2.2.3. The substrate thickness, $t_s$ plays an important role since the resulting average power output will decrease from 9.1 to 4.2 mW as $t_s$ increases from 0.2 mm to 0.9 mm.

This is because when $t_s$ increases, the cross-section area of the sandwiched structure increases, the stress level and power output will decrease when the same force is applied. Another significant point is that when the substrate thickness decreases, its ability to reduce the stress concentration will decrease at the same time. Therefore, the minimum applicable $t_s$ is 0.6 mm, which leads to a power output of 5.7 mW (Kuang et al., 2017).

### 2.3.2    Effects of the End Cap Material and Thickness, $t_c$.

Kuang et al. (2017) had evaluated the effects of the end cap material on the generated power output, by comparing four metallic materials with different Young's modulus and stress limits, namely stainless steel, copper (Cu) alloy, titanium (Ti) alloy, and aluminium (Al) alloy. It shows that using Al alloy as end caps can generate the highest power output, followed by Ti alloy, Cu alloy, and lastly stainless steel end caps. This is because Al alloy has the lowest Young's modulus which deforms the most among the four metals, followed by the Ti alloy, Cu alloy, and stainless steel.

When the end cap thickness, $t_c$ increases, the average power output will decrease since the end caps become stiffer and thus deform less under the same load force. It concluded that a more flexible end cap design with a smaller thickness and a lower Young's modulus is more efficient for energy conversion. However, when minimizing $t_c$ to maximize the power output, consideration must be taken on the yield strength of the end cap material

since the maximum von Mises stress in the end caps will increase if the end cap becomes thinner. Hence, due to the highest yield strength of Ti alloy, it is the best material for the end cap. However, Kuang et al. (2017) selected stainless steel as the end cap material for the overall consideration of the material strength, power output, cost, and availability in their study.

### 2.3.3 Effects of the Piezoelectric Plate Thickness, $t_p$

Kuang et al. (2017) found out that there is an optimal PZT thickness that produces a maximum power output for a particular PEH mass. When $t_p$ increases, the mass of the PZT increases and so does the ratio of the PZT mass to transducer mass. Hence, a larger amount of the mechanical energy input acting onto the PEH is absorbed by a thicker PZT to generate more power. As $t_p$ continues to increase, the PEH becomes stiffer, causing less deformation and mechanical energy is applied onto the PEH. Therefore, an optimal $t_p$ can be concluded at which the mechanical energy absorbed by the PZT and the electric power output both reach the maximum value.

### 2.3.4 Effects of End Cap Internal Angle by Altering Cavity Height, $H$

The internal angle is altered by varying the height of the cavity, $H$ which can be achieved by changing the length of the inclined segments of the end cap while keeping other parameters as constant. According to equation [2.15], the amplification factor will increase with decreasing in internal angle. In the real case scenario, the end cap segments will be shortened due to the large force applied at a very small internal angle. Thus, causing the amplification factor to decrease and power starts to decrease after hitting the highest power output. It is found out that equation [2.15] is only valid when the deformation of the end cap is small enough and the change in length of the end cap segments is not considered. In short, an optimum internal angle of 15° is suggested to

generate the highest power output with the particular Rectangular Cymbal PEH dimensions (Kuang et al., 2017).

To conclude, a small value of angle and thinner thickness of end cap tend to increase the amplification ratio. In fact, as long as the parameters are related to the end cap, substrate, and PZT, the power output is definitely influenced. Therefore, the optimizations of the width, height, thickness, and length of the frame, as well as PZT, are crucial in order to obtain a compact size and maintain the stability of the structure with high energy harvesting performance.

## 2.4    Energy Harvesting Circuit and Storage

An energy harvesting circuit is a series of linkage components between the energy harvester such as the PZT element and the application load. It is made up of an AC-DC rectifier, a step-down converter or known as a voltage regulator, and an energy storing device as shown in Figure 2.40.
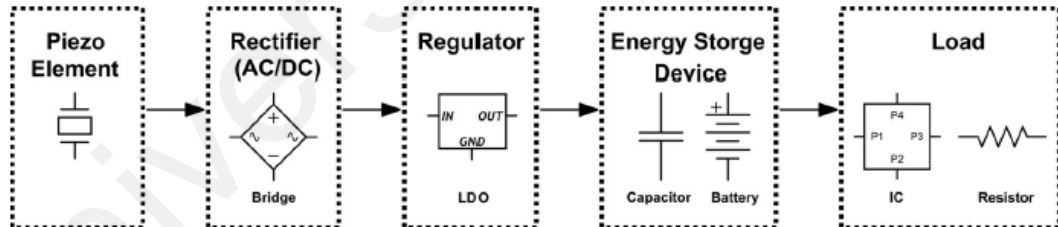


Figure 2.40 Block diagram of the PZT energy harvesting electric circuit
(H. W. Kim et al., 2004)

The important criterion of a circuit design is that it should be able to maintain the power output always at the maximum level. Since PZT is being compressed and released alternatively in the application, the voltage output will be intermittent. Hence, the designed circuit should adapt to these changes without failure (H. W. Kim et al., 2004).

### 2.4.1    AC-DC Rectifiers

One of the common solutions is by using a full-wave rectifier circuit with four diodes in a bridge circuit to rectify the AC voltage output from PZT to DC power with a connected capacitor. Normally, the power output is first rectified through a rectifier circuit and then transferred to a low-impedance load using a DC-DC converter circuit. As the resistive load increases, the output voltage generated by the transducer will increase too. When the power output reaches its maximum, the matching impedance is nearly equal to the calculated optimum resistance as shown in equation [3.2].

### 2.4.2    Step-down Converter / Voltage Regulator / DC-DC Converter

The rectified voltage produced by the PZT is then regulated to store in the energy storage device or external load. Tayahi, Johnson, Holtzman, and Cadet (2005) had proposed to use a step-down converter (LTC1474, Linear Technology) for powering remote sensing networks. It can stabilize the output voltage by having a discharging circuit. A reservoir capacitor is added to store the harvested energy in this designed circuit. Whenever the capacitor reached a pre-set value, it will discharge into the step-down converter, else the discharge circuit will be switched off.

Besides, to maximize the power input stored in an electrochemical battery, Ottman, Hofmann, and Lesieutre (2003) had proposed a controlled regulator circuit to increase the rate of charging in a battery by increasing the current flowing into the battery. Ottman's control algorithm is designed to sense the current flow into the battery and adjust the duty cycle of the switching DC-DC converter accordingly with 400% of improvement. However, this control circuit needs more power than a small PZT can provide. Hence, Ottman et al. (2003) discovered the interaction between PZT and the DC-DC converter that worked in discontinuous conduction mode (DCM) to solve this problem.

To amplify the power generated at low impedance, a DC-DC converter circuit had been proposed by H. W. Kim et al. (2004) which is named as buck converter as shown in Figure 2.41. It has a great effect on the application of battery charging since there is a shift in matching the impedance of the transducer. However, its optimal duty cycle is depending on inductance, switching frequency, the PZT capacitance, and the frequency of mechanical excitation of the piezoelectric device (Ottman et al., 2003).
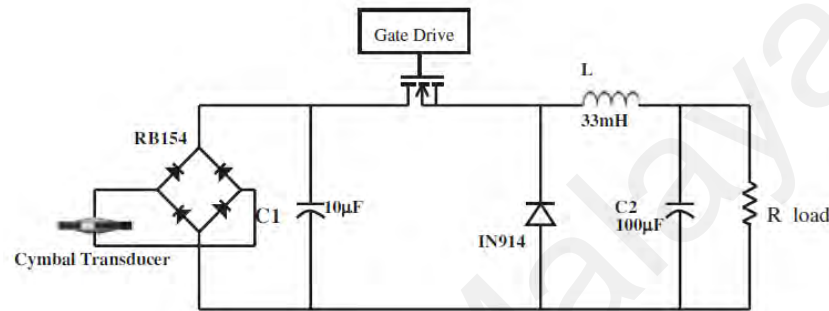


Figure 2.41 DC-to-DC converter circuit (H. W. Kim et al., 2004)

### 2.4.3 Energy Storage Devices

Since the power generated by PZT is normally small which is not enough to directly power up an electronic device or sensor, thus the generated energy is first stored in a storage device before using by any load. The saved energy is capable of powering WSNs, which can be used for a transportation monitoring system.

### 2.4.3.1 Capacitor

A capacitor has the advantage of not requiring any minimum voltage to start charging and thus it had been proposed by many researchers. Moreover, the capacitor can be charged and discharged in a short time because of its high power density. However, the drawback of the capacitor is that it has much lower energy densities which caused the voltages to drop instantaneously when it is discharged. In short, the capacitor is only suitable for applications that need rapid energy transfer but not those that require a stable output

voltage, while the rechargeable battery has a limited number of charging cycles (H. Li et al., 2014).

### 2.4.3.2 Supercapacitor

The supercapacitor has an electrolyte solution between two solid conductors to store the electrostatic charges. It has a great surface area which enables it to store more energy than conventional capacitors. Guan and Liao (2006) had carried out a series of studies on supercapacitors in terms of its energy density, capacity, and lifespan. It was then found out that the leakage resistance was the main factor that influences the performance of this storage device. All in all, the researchers suggested using the supercapacitor rather than the commercial capacitor due to its great performance in all aspects (Guan & Liao, 2006).

### 2.4.4 Integrated Circuits (ICs)

In recent years, an integrated circuit (IC) has been designed which is composed of all necessary components of an energy harvesting system in one circuit.

### 2.4.4.1 LTC3588–1

The commonly used IC in the PZT or solar energy harvesting field is the LTC3588–1 by Linear Technology as shown in Figure 2.42 (a). HiLetgo and SparkFun had come out with a smaller size of LTC3588 energy harvester breakout with only $20 \times 13$ mm$^2$ as shown in Figure 2.42 (b) and (c). The LTC3588 integrates a low-loss full-wave bridge to rectify a voltage waveform, a high-efficiency buck converter to maintain a regulated output voltage and store harvested energy on an external capacitor. In other words, it can be directly connected to the PZT or AC power source and readily output the harvested energy to power up a microprocessor as shown in Figure 2.42 (d). Hence, this circuit is suitable for wireless sensor networks and industrial equipment controls (H. Li et al., 2014).
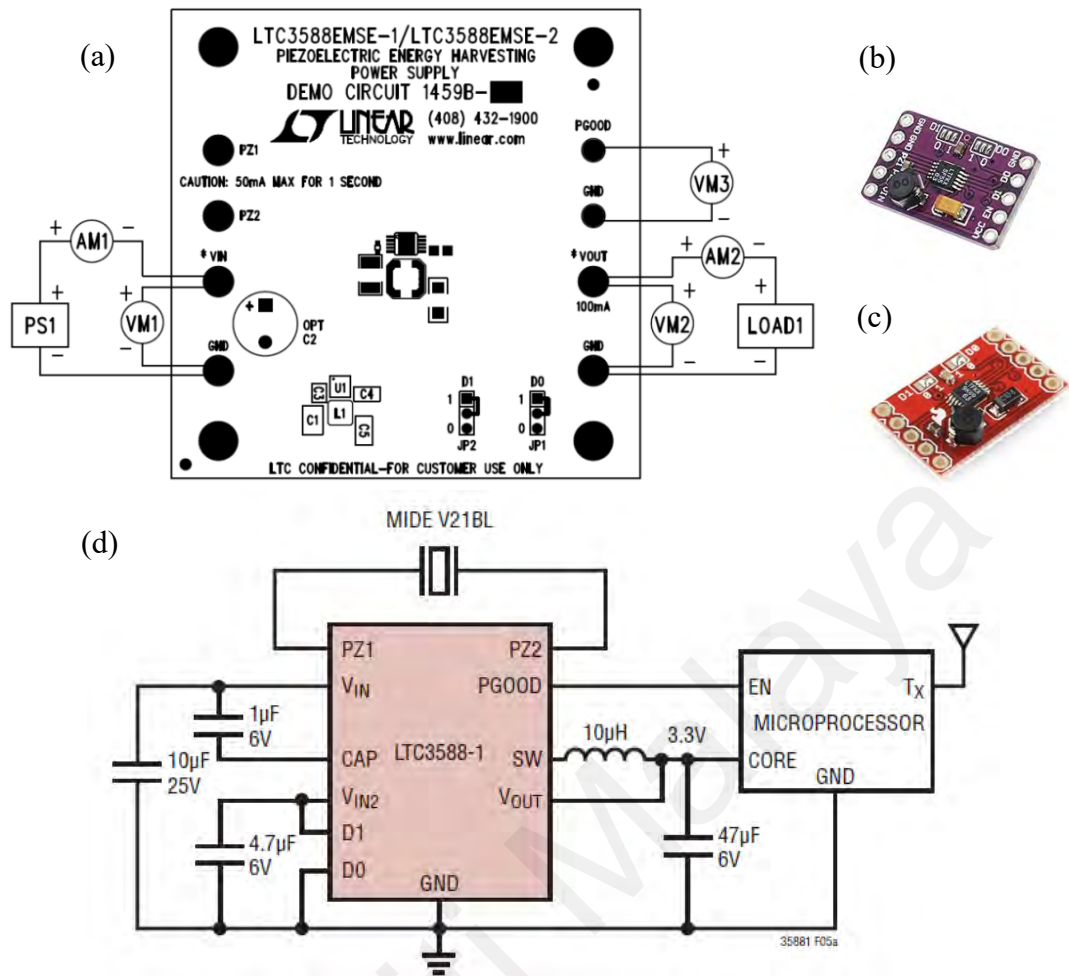
Figure 2.42 LTC3588–1 Piezoelectric Energy Harvesting Circuit by (a) Linear Technology, (b) HiLetgo, and (c) SparkFun (Analog Devices, 2019; SparkFun Electronics, 2020); (d) LTC3588-1 circuit diagram to power up a 3.3 V microprocessor with a wireless transmitter (Analog Devices, 2019)

LTC3588 has a wide input operating voltage range of 2.7 V to 20.0 V. The 20 V input protective shunt can accommodate a variety of piezoelectric elements and enable greater storage for a given amount of input capacitance. This IC has four selectable output voltages of 1.8 V, 2.5 V, 3.3 V, and 3.6 V with up to 100 mA of continuous output current. The low quiescent current of the LTC3588-1 enables efficient energy accumulation from piezoelectric elements which can have short-circuit currents on the order of tens of microamps. It can work under a temperature range of –40 to 120 °C. Moreover, the Undervoltage lockout (UVLO) mode with a wide hysteresis window allows charge to accumulate on an input capacitor until the buck converter can efficiently transfer a portion

of the stored charge to the output. In regulation, the LTC3588 enters a sleep state in which both input and output quiescent currents are minimal.

The versatile LTC3588-1 can be used in a variety of configurations to have more additional features. For example, it can also be used in concert with a backup battery connected to $V_{in}$ to supply the system if ambient vibrational energy ceases as shown in Figure 2.43. A blocking diode is placed in series with the battery to prevent reverse current in the battery if the piezo source charges $V_{in}$ past the battery voltage. Any stack of batteries that is less than 18 V can be used as a backup battery. Hence, the battery life can be greatly increased with this configuration.
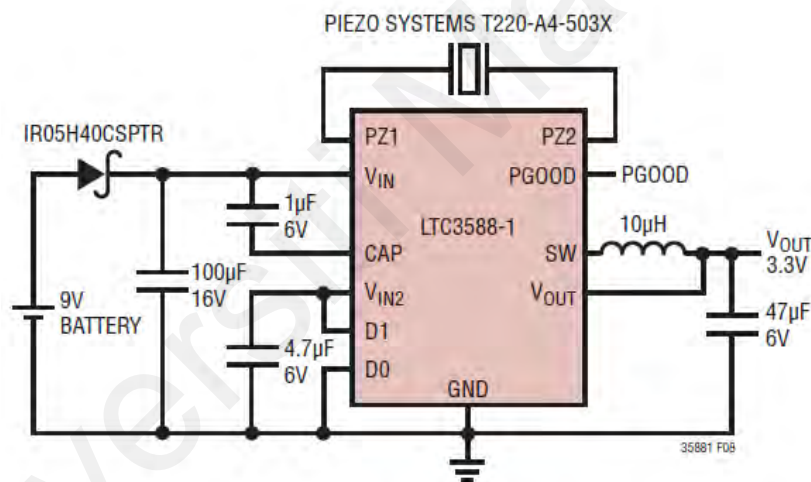


Figure 2.43 Circuit diagram of harvesting circuit with 9 V backup battery
(Analog Devices, 2019)

### 2.4.4.2 EH300 series harvesting circuit

EH300A is one of the energy harvesting modules from Advanced Linear Devices Energy Harvesting Modules with ultra-high-efficiency as shown in Figure 2.44. It can capture and store wasted energy from a variety of energy sources, such as piezoelectric, electromagnetic, solar, and thermoelectric materials. It has a compact size of $50 \times 18 \times 14 \text{ mm}^3$ and a maximum operating temperature of $70 \,^{\circ}\text{C}$. It has a wide input voltage range of up to 500 V and an input current of 200 nA to 400 mA. The harvested energy can use

to power electrical circuits and wireless sensor networks which require a DC voltage of 1.8 V to 5 V (Mouser Electronics, 2020). EH300A circuit had been used to charge a 100 µF capacitor with a piezoelectric flow energy harvester in 5.2 m/s airflows by Gao (2011).
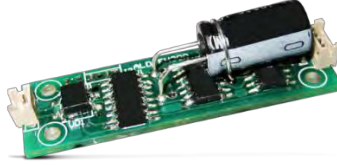


Figure 2.44 EH300A harvesting circuit (Mouser Electronics, 2020)

### 2.4.5 Voltage or Power Output Monitoring Devices

There are several ways to monitor and measure the power generated by the transducer during the experiment. Ren et al. (2010) used a Tektronix Digital Oscilloscope Hewlett Packard 54645A to monitor the output voltage by connecting the transducer with several load resistors to evaluate the performance of the device. The power, $P$ under different load resistances, $R_L$ can be calculated as

$$P = \frac{V_P^2}{2R_L} \qquad [2.21]$$

where $V_p$ = output peak voltage.

Another test was done by Kuang et al. (2017) using a National Instrument-NI 9229 data log to measure the voltage generated across the load resistor and calculate the total power generated. There is also another way to monitor the output voltage from the transducer by using an Agilent digital oscilloscope (model DSO6014A) (Xiaotian Li et al., 2011) or a digital storage memory oscilloscope (Agilent MSO-X 3054A) (L. Wu et al., 2014). Mo et al. (2013) had measured the output voltage by a Tektronix digital storage oscilloscope (TDS 2014C), which can measure the applied input load and the displacement of the transducer at the same time. The experiment was done by testing the fabricated transducer on an MTS Systems Corporation load-frame (Model 976.10-99) and

then applying cyclic loads of 720 N and 1940 N respectively at a frequency of 1 Hz as shown in Figure 2.45. To regulate the load resistance, a resistance control box (Global Specialties—RC10) was used.
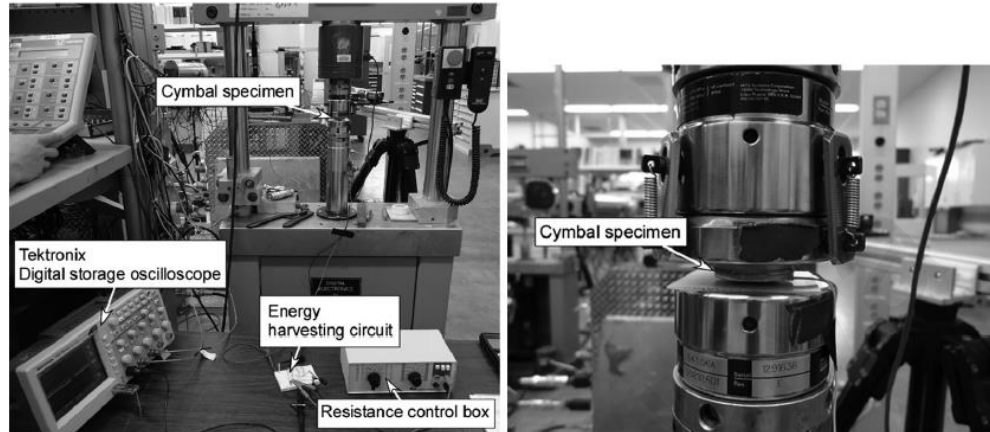


Figure 2.45 Devices used in the experiment done by Mo et al. (2013)

In summary, with the appropriate circuit used, the energy harvested by PEH can be stored and used for many applications, not only to power up other electronics but also to achieve a self-powered sensor system. This technology contributes to resolving the power supply problems of roadside monitoring devices and benefits the development of the IoT in the field of intelligent transportation.

# CHAPTER 3: METHODOLOGY

In this study, a novel compressive mechanical structure amplifier of the PEH is aimed to be fabricated and tested experimentally. Figure 3.1 shows the methodology flow chart of this study. At the beginning of this project, sufficient information regarding the proposed idea is gathered. Based on the literature review, several aspects are considered during the design process to optimize the performance of the PEH.
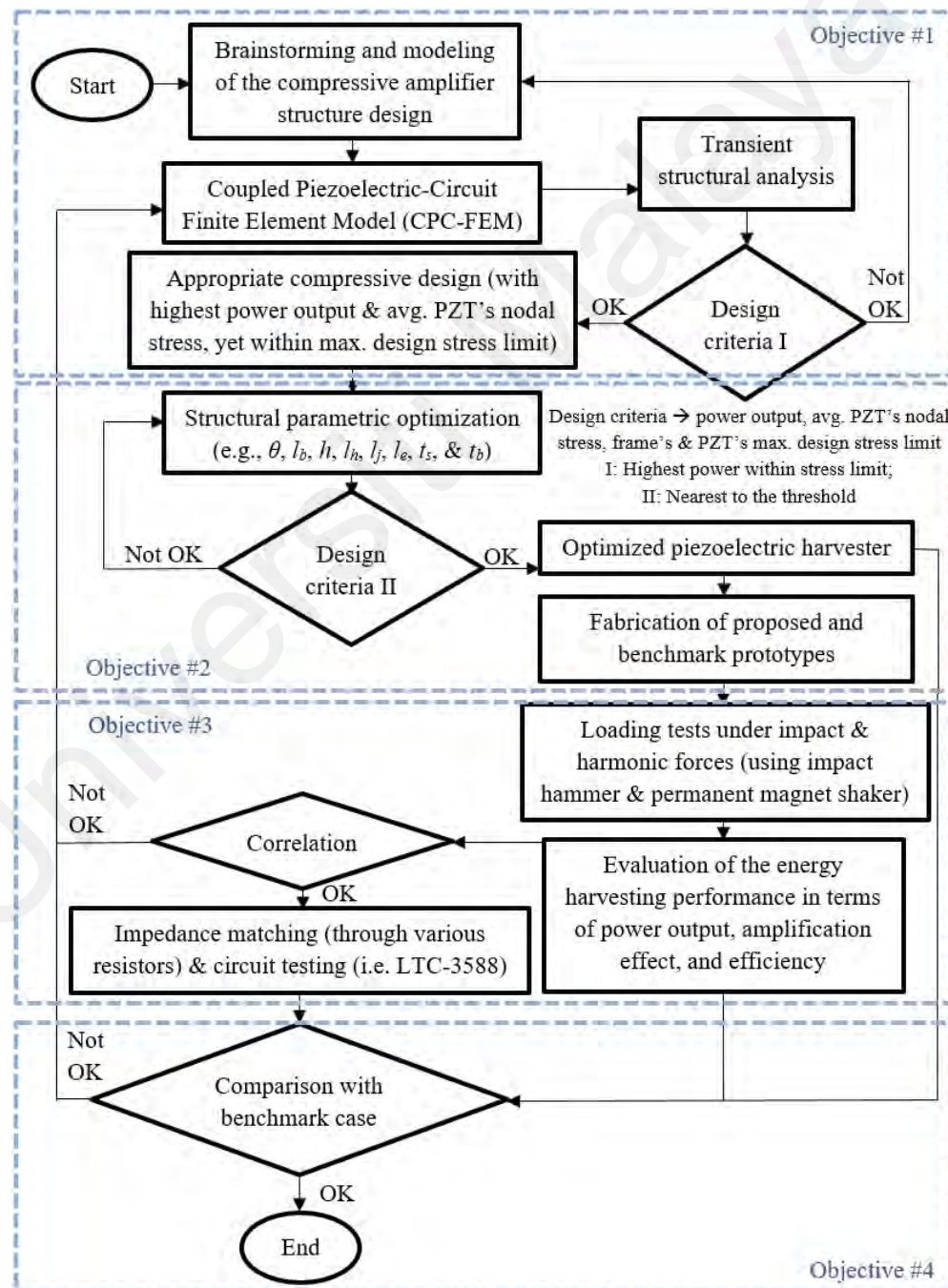


Figure 3.1 The methodology flow chart

## 3.1    Background Study

Various types of the existing PEH design had been studied to find out the optimal PEH design under a high force environment. These included the designs of mechanical amplifier structure, parameters that affect the performance of PEH, as well as circuit and energy storage systems. Several characteristics of the current existing PEH, including the main success factor of PEH or root cause of design failure, were being compared and evaluated. This is to investigate the main manipulation factor of a high-performance mechanical amplifier structure, such as the flexure hinge with a certain angle and the trapezoidal cavity shape for the flextensional structure. The gathered literature was reviewed and interpreted to identify the research gap. A short conclusion was made for each sub-section in the literature review.

## 3.2    Concept Generation and Selection

After reviewing the literature, several compressive structural designs were proposed based on the developed inverted trapezoidal cavity shape idea, which could achieve a compressive effect by remaining the PZT below the centre of cavity and utilizing the more commonly used compressive downwards loading force. Some additional features and frame designs were proposed as well. The parameters which were expected to have a huge impact on the energy harvesting performance are the inclined angle, frame linkage length, frame thickness, frame base length, and joint length. Thus, all these parameters were selected to be investigated further in this study.

## 3.3    Modeling

A computational-aided design software, SolidWorks® was used to construct the PEH model. FEA simulations were carried out to examine the performance of each proposed structure design. A validation of FEA settings had been done before selecting the best design. Similar settings were used for all the proposed designs to ensure a fair comparison

at the initial stage. For instance, a constant size of the PZT plate with the same frame's thickness was used in all simulations. An analytical model had been developed for the selected design before going through the parametric optimization.

### 3.3.1 Finite Element Analysis (FEA) Settings

A CPC-FEM was developed with ANSYS 18.2, an FEA software. It comprised a 3-dimensional (3D) structure of the PEH with a load resistor connected across the electrode of the PZT plate. This CPC-FEM combined the simulation of electric circuits and piezoelectricity in one model. In other words, the stress analysis, voltage, current, and power generated by the PEH could be simulated at the same time via CPC-FEM.

The simulation was started with a transient structural analysis by adding all the related material properties for the frame as listed in Table 3.1. General SUS 304 Stainless Steel with 251 MPa yield strength was selected as the frame material in the simulation at the initial stage. Other types of material, namely Titanium alloy (Ti) with a higher yield strength of 760 MPa or hot-rolled stainless steel, were used to replace the SUS 304. Equal channel angular pressing (ECAP) AISI 304L with a tensile yield of 1121 MPa and compressive yield strength of 768 MPa was another option for the frame material.

Meanwhile, the material properties for the DL-53HD soft PZT plate (from DeL Piezo Specialties) were added to the FEA engineering data, as shown in Table 2.1. It has a tensile yield strength of 35 MPa and a compressive yield strength, which is 10 times its tensile value. By taking a safety factor of 2, the yield strength is further divided to half.

Table 3.1 Mechanical properties of Stainless steel and Titanium alloy

| Mechanical properties | Type of material | Stainless steel SUS 304 | Titanium alloy Ti-5Al-2.5Sn |
|---|---|---|---|
| Isotropic elasticity | Young's modulus (GPa) | 193 | 110 |
| | Poisson's ratio | 0.24 | 0.34 |
| Density (kg/m$^3$) | | 8030 | 4480 |
| Yield strength (MPa) | | 251 | 760 |

Next, the positive and negative electrodes were defined at the top and bottom surfaces of the PZT plate respectively. A particular command under PZT geometry was inserted to define the master node at the electrodes as shown in Figure 3.2. It was done by firstly fixing the time integration parameters specifically for piezoelectric analysis. Following that, defined the variables, *H1* as the coordinate of the bottom electrode and *H2* as the coordinate of the top electrode in the vertical z-axis. After that, coupling all the voltage degrees of freedom, so that the simulated voltage was even.

```
/prep7
tintp,,0.25,0.5,0.5
H1 = 3.5587e-002
H2 = 3.9587e-002
nsel,s,loc,y,H2
cp,2,volt,all
*get,n_top,node,0,num,min
nsel,s,loc,y,H1
cp,1,volt,all
*get,n_bot,node,0,num,min
nsel,all
```

Figure 3.2 The command used to collect voltage value by defining the top and bottom electrode at the PZT

Suitable connection types were selected for all the contact regions. Mesh element size of 1.5 mm and element type, CIRCU 94 and SOLID226 were selected in this simulation. Furthermore, the fixed support was set at the bottom end cap as the boundary condition setting. An input force (i.e., 1 kN of sinusoidal force with 2 Hz or 1 kN of impact force for 0.01 s) was applied at the top end cap in z-axis.

Since a safety factor of 2 was suggested by the literature, the PEH could work safely under forces up to 2 kN. Meaning that it was capable to withstand a city car, for example, a *Perodua Kancil* with a range of car mass between 650 - 690 kg. By assuming a capacity of 2 persons, the city car had a total mass of 800 kg (8 kN), which is equal to 2 kN per wheel weight. From another perspective, a typical cruiser motorcycle with a rider that had a total useful payload of 200 kg could apply 1 kN per wheel on the developed PEH. The 2 Hz sinusoidal force function was used to demonstrate a huge number of vehicles that

passed through the PEH continuously. For instance, 10 vehicles passed through the PEH in 10 s, which meant two hits on the PEH per second by the front and rear tires of a vehicle. On the other hand, the 0.01 s impact force was used to demonstrate the human foot strike with a bodyweight of 50 - 100 kg on the developed PEH.

Figure 3.3 shows another command was inserted to create a circuit using the element type of CIRCUIT 94, which included a resistor. The optimal resistance, $R_{opt}$ was set to be 5.989 MΩ as calculated by using equations [3.1] and [3.2].

```
nsel,all
d,n_bot,volt,0
/prep7
et,100,CIRCU94,0
RC = 5.989e6
r,20, RC
type,100  $  real, 20
e, n_top,n_bot
/solu
outres,esol,all
```

Figure 3.3 APDL command used to create a circuit

The capacitance of the PZT plate, $C_p$ and $R_{opt}$ values were calculated as follows:

$$C_p = \frac{\varepsilon_0 \varepsilon_{33} W L_e}{t_p} = \frac{8.85 \times 10^{-12} \times 3850 \times 0.03 \times 0.052}{0.004}$$

$$= 1.329 \times 10^{-8} \ F \qquad [3.1]$$

$$R_{opt} = \frac{1}{2\pi f C_P} = \frac{1}{2 \times 3.142 \times 2 \times 1.329 \times 10^{-8}} = 5.989 \times 10^6 \ \Omega \qquad [3.2]$$

where $\varepsilon_0$ = free space permittivity constant of PZT; $\varepsilon_{33}$ = relative permittivity constant of PZT; $f$ = the frequency of the excitation force.

The desired solutions were inserted, namely the overall equivalent Von-Mises stress, particular equivalent stress of PZT plate, strain energy, and total deformation. With this, the model was ready to run and solve. The maximum stress value and location could be monitored and analyzed.

After that, another component system, Mechanical ANSYS Parametric Design Language (APDL), was used to obtain the voltage output and the average electric power output of the PEH. It was done by adding the input and reference files of that structural analysis into the Mechanical APDL, then editing it with a command to record the element solutions of the load resistor.

A command was inserted to show all the voltage, current, and power generated by the PZT plate as shown in Figure 3.4. The power output was then calculated by taking the average value shown in Figure 3.5.

```
/post26
*get,Circu,elem,0,num,max
esol,5,Circu,,smisc,2,I_piezo
esol,6,Circu,,nmisc,1,power
esol,7,Circu,,smisc,1,V_piezo
prvar,I_piezo,I_equiv,I_targ,power,V_piezo
prvar,I_piezo,power,V_piezo
plvar,I_piezo,I_equiv,I_targ,power,V_piezo
```

Figure 3.4 The command used to list and plot the power output data
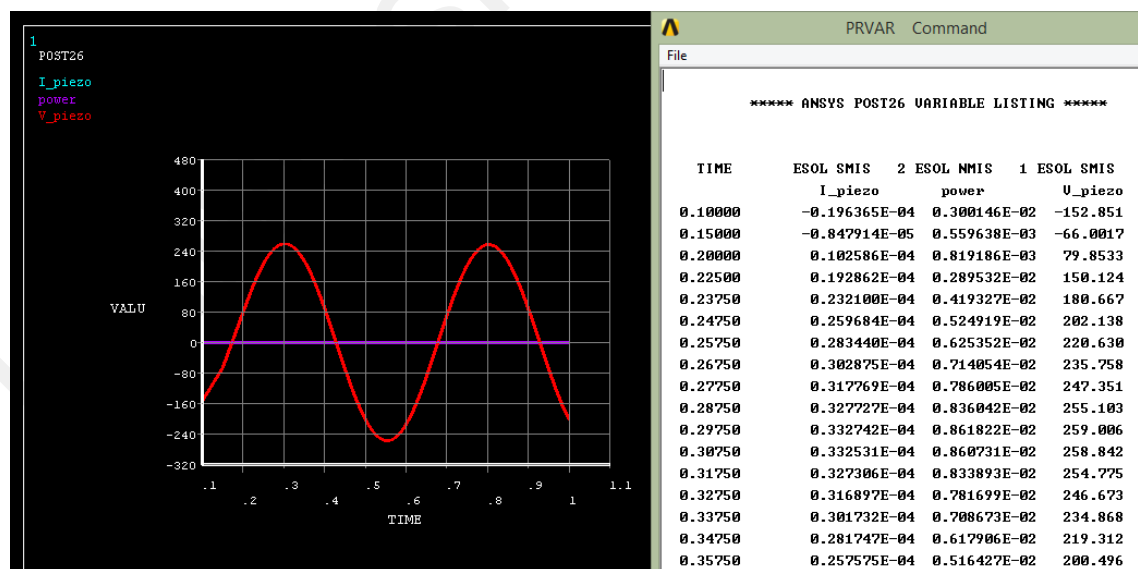


Figure 3.5 An example of power output data in APDL

With the FEA stress and power output results for all the proposed mechanical structure designs, the best compressive amplifier structure could be selected. However, before proceeding to the design selection, a validation of the FEA setting should be done. A

study on Rectangular Cymbal (known as Bridge structure in (Kuang et al., 2017)) PEH had been chosen as the benchmark case. To corroborate the FEA setting in this study, a similar dimension of Rectangular Cymbal PEH was constructed and optimized through the developed CPC-FEM. A good agreement of the FEA result should be achieved for the same structure in both studies. under the same boundary conditions, such as 1 kN sinusoidal force at 2 Hz. Figure 3.6 shows the forcing function and the constructed path at the edge of the PZT plate to extract the stress level. A close result was obtained and proceeded with the simulation of the proposed designs.
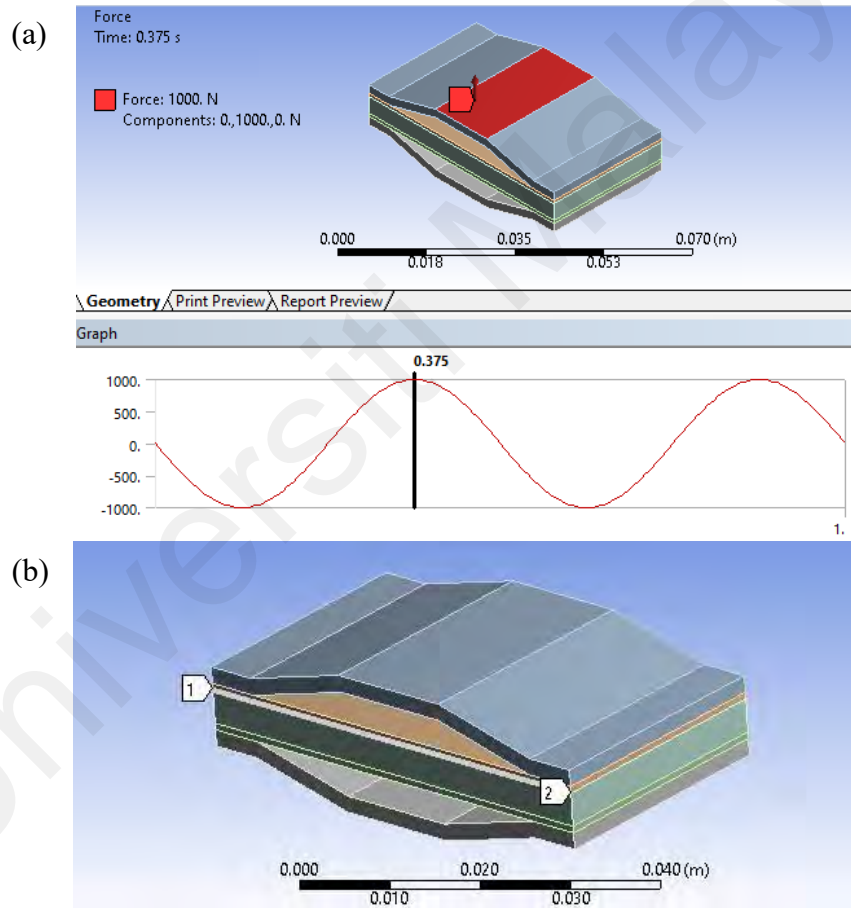


Figure 3.6 (a) Sinusoidal forcing function was set at the benchmark structure;
(b) The PZT's stress distribution along the length of the PEH was extracted by
constructing a path at the edge of the top surface of the PZT plate

All the proposed designs were evaluated based on the loading capacity (in terms of stress concentration and stiffness of amplifier structure), the energy harvesting performance (in terms of power density, force amplification effect, and efficiency), the

size, and the product cost. Some important considerations on the material strength must be taken, such as the working stress should not exceed the ultimate stress or the stress limit set in this study. This is to ensure the PEH works properly in high force environment while designing the mechanical amplifier structure. Meanwhile, the material usage and bonding method were selected wisely to maximize harvested power. The power output of the developed PEH with the best compressive amplifier structure was compared with the Rectangular Cymbal PEH to evaluate its overall performance.

Parametric optimization was carried out next to further enhance the amplification effect which included the inclined angle, frame thickness, base length, etc. When one parameter was being studied, the other parameters were kept constant. The relationship of each parameter on the power output and amplification effect were examined and discussed. Refinement on design dimension was carried out and the simulation was repeated until the PZT was fully utilized. All the FEA results are collected, analyzed, and discussed to finalize the optimum design of the PEH. The optimal dimension of the PEH was the best combination of all parameters which produced the highest power within its load capacity. The performance of the optimized structure was then compared with the unoptimized case. Another comparison was made between the optimized structure and the benchmark structure. The FEA result was then compared with the experimental results through the fabricated PEH.

## 3.4 Method of Fabrication for the Proposed and Benchmark PEH

The proposed PEH was fabricated by using the selected materials with the optimal dimensions of the amplifier frame determined in the previous FEA stage. A tensile type Rectangular Cymbal amplifier structure PEH which had been optimized by Kuang et al. (2017) under the same loading environment, is fabricated to act as a benchmark case. Two same-size soft DL-53HD PZT plates ($52 \times 30 \times 4 \text{ mm}^3$) are used in both structures to

ensure a fair comparison. After the prototypes of the PEH were fabricated, the joining or bonding of parts was carried out, for example joining the PZT plate with the end cap by using specific adhesive. 3M Scotch-Weld™ DP-460 structural adhesive was strongly suggested by several researchers to use in joining the substrates and the PZT plate, which has higher shear and peel strengths, and better heat and chemical resistance (Daniels et al., 2013). Laser welding was then carried out to attach the substrates with the metal end cap subsequently for the Rectangular Cymbal structure. Wire connection was done by soldering.

## 3.5 Loading Experiment for the Proposed and Benchmark PEH

Several loading experiments were conducted accordingly to evaluate the performance of the optimized PEH. For example, the loading tests were done by using Dytran Dytranpulse™ 5800B3 impulse hammer, PCB® Piezotronics 086D20 impact hammer, and permanent magnet shaker V201 to induce different types of force under a range of frequency. An impact force was applied on the PEH to demonstrate the applications such as human foot strike under shoes, floor tile, and vehicle's wheel loading on road surfaces; while a harmonic force was used to test the charging performance of the PEH under higher frequency. The developed compressive PEH and the benchmarking tensile Rectangular Cymbal PEH were tested under the same forcing environment to ensure a fair comparison. Their energy harvesting performances were examined in terms of power output and efficiency.

### 3.5.1 Impact Loading Test to Examine the Energy Harvesting Performance of PEH

An impact loading test was conducted to verify the FEA voltage and power output of the PEH using the impact hammer as shown in Figure 3.7. It was used to investigate the influence of the amount of applied load force on the voltage output. A Dytran

DYTRANPULSE™ series 5800B3 impulse hammer with a sensitivity of 10.91 mV/N, was used to induce an impact force with a lower range (< 200 N) on the PEH at the initial stage. It was then changed with another higher forcing range of impact hammer (i.e., PCB® Piezotronics 086D20 impact hammer) with a sensitivity of 0.23 mV/N. A statistic module was used to show the maximum value of the voltage produced for the corresponding peak caused by the impact. A voltage divider had been used to extend the measurable range of the Data Acquisition (DAQ) devices by reducing the measured voltage. The impact force was increased from 10 N to 1 kN manually and the result was recorded.

A direct comparison of the open-circuit peak voltage among the proposed PEH, benchmark PEH, and standalone PZT plate had been made, which shows the voltage amplification factor as well. Impedance matching had been carried out to find out the optimum resistance and maximum power output with different resistors. The energy conversion efficiency was computed by retrieving the mechanical input response (i.e., the displacement) from the accelerometer.

Procedures:

1. A DASYLab™ worksheet was prepared as shown in Figure 3.8 to visualize and record important data such as the input force and the voltage output. The sampling rate was set at 2560 S/s and block size was set at 4096.

2. The developed PEH prototype was fixed under the metal bars. The PZT wires were connected through the National Instrument Data Acquisition (NI DAQ) devices (i.e., NI cDAQ-9174 and NI-9232) to the personal computer (PC) while the impact hammer was connected to the DAQ NI-9234. A voltage divider with a total resistance of 10 MΩ (ratio of 1:10) was connected across the PZT if the output voltage was out of the measurable range (± 30 V) of the NI-9232.

3. The DASYLab™ worksheet was executed and loading force was applied from 10 N to 1 kN onto the prototype.

4. The applied input force and the corresponding output voltage were recorded.

5. The voltage output was then compared with the FEA result to verify the accuracy of the developed CPC-FEM. The percentage of deviation was calculated and discussed.

$$\text{Percentage deviation} = \frac{|Theoretical\ value\ -\ Actual\ value|}{Theoretical\ value} \times 100\% \qquad [3.3]$$

6. Steps 2 to 4 were repeated for the benchmark PEH and the standalone PZT plate. A graph of open-circuit peak voltage against input force for all the prototypes was plotted. The harvesting performance was compared based on the gradients of the graph.

7. Steps 2 to 4 were repeated by connecting the PEH across a range of resistors (10 kΩ - 1 MΩ). Impedance matching had been carried out to find out the optimum resistance and the highest power output. The percentage deviation to the FEA result was calculated through equation [3.3].

8. With the optimum resistance found in Step 7, the experiment was repeated for 1 kN of impact force. Post-processing of the acceleration response retrieved from the accelerometer with a sensitivity of 100 mV/g was carried out. For instance, double integration and band filter to obtain the mechanical input displacement. The energy conversion efficiency was calculated through equations [2.9] – [2.11].
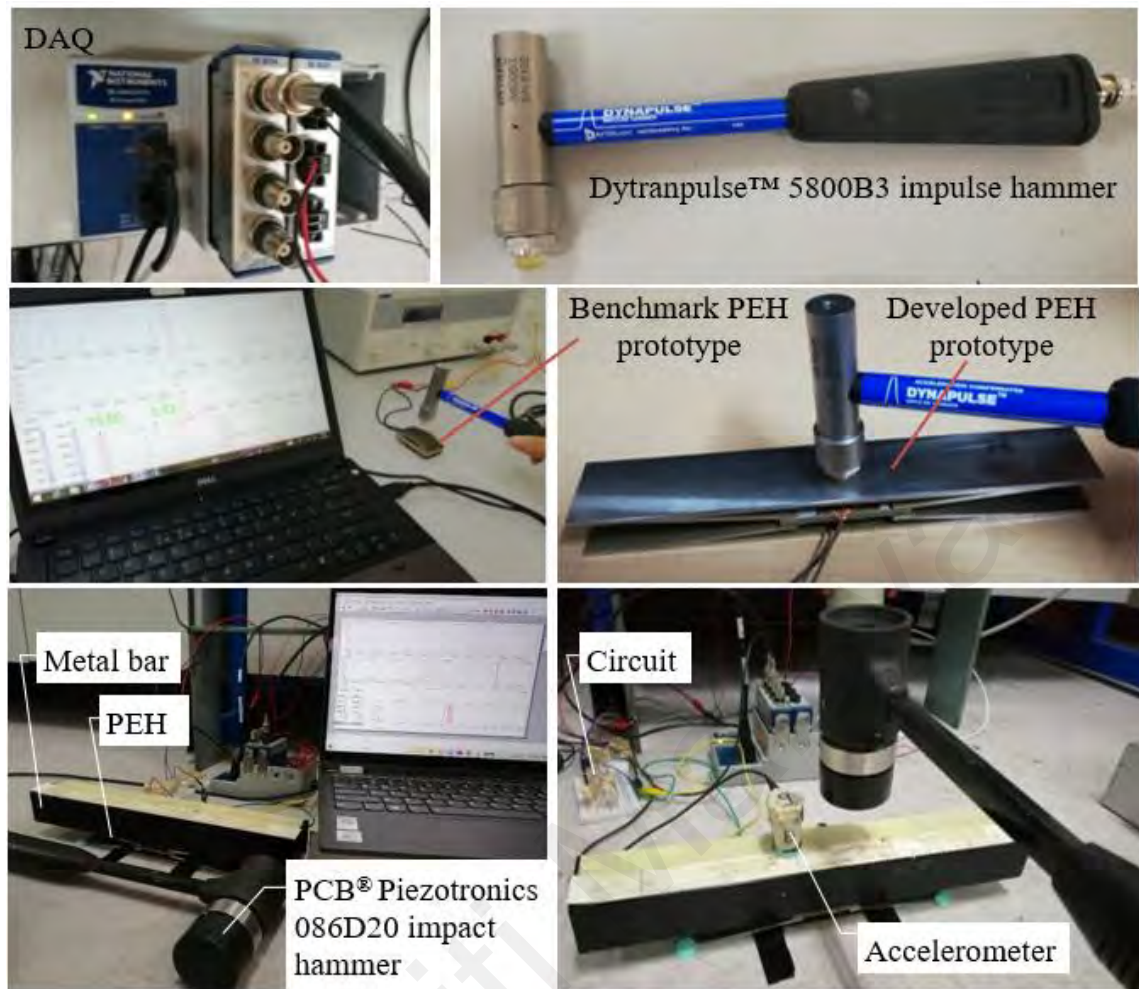
Figure 3.7 Impact testing setup
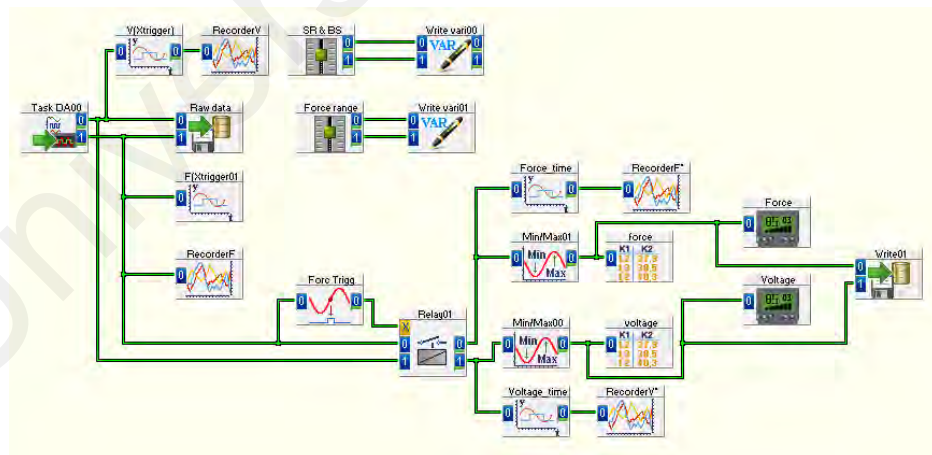

Figure 3.8 DASYLab™ Worksheet for loading test

### 3.5.2 Compression Loading Test Using Permanent Magnet Shaker V201

An LDS permanent magnet shaker (V201) could apply force with a wide frequency range which was up to 13000 Hz. Although its loading capacity was much smaller (in this case, 10 N sinusoidal loading force with 50 Hz was steadily applied), a rapid charging test

could be carried out with the energy harvesting circuit under the higher frequency loading. The same DAQ instruments and procedure as mentioned in Section 3.5.1 could be used in this experiment. Only the impact hammer was replaced by a shaker with LDS linear power amplifier (PA25E) and a Farnell function generator (FG3). A PCB® Piezotronics 208C01 force sensor with a sensitivity of 112.4 mV/N was attached at the shaker. It was connected to the DAQ NI-9234 to retrieve the input force.

Meanwhile, a Linear technology piezoelectric energy harvesting circuit, LTC 3588-1 could be tested on its performance such as charging time and the total harvested energy within a certain period via this experiment as shown in Figure 3.9. Figure 3.10 (a) shows the worksheet to retrieve the input mechanical and output electrical responses; while Figure 3.10 (b) shows the layout with the important variables, such as input force, acceleration, velocity, displacement, and output voltage. The root-mean-square voltage was computed in the DASYLab$^{TM}$ and used to calculate the power output under harmonic force.
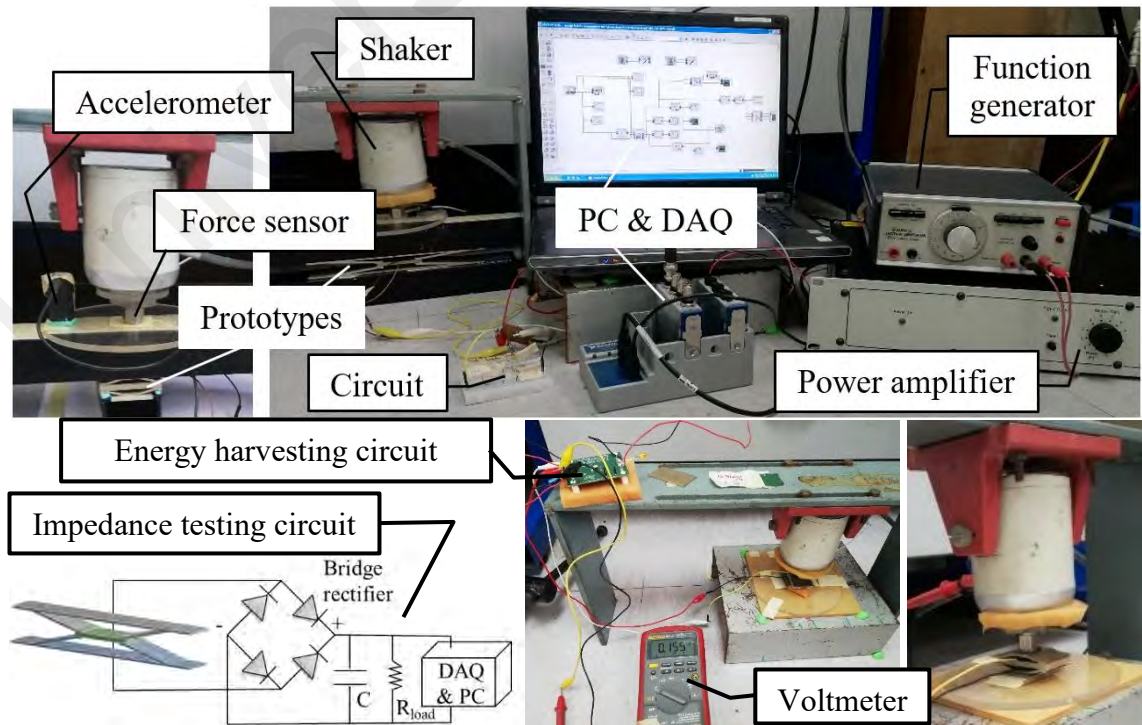


Figure 3.9 Shaker test experimental setup

(a)
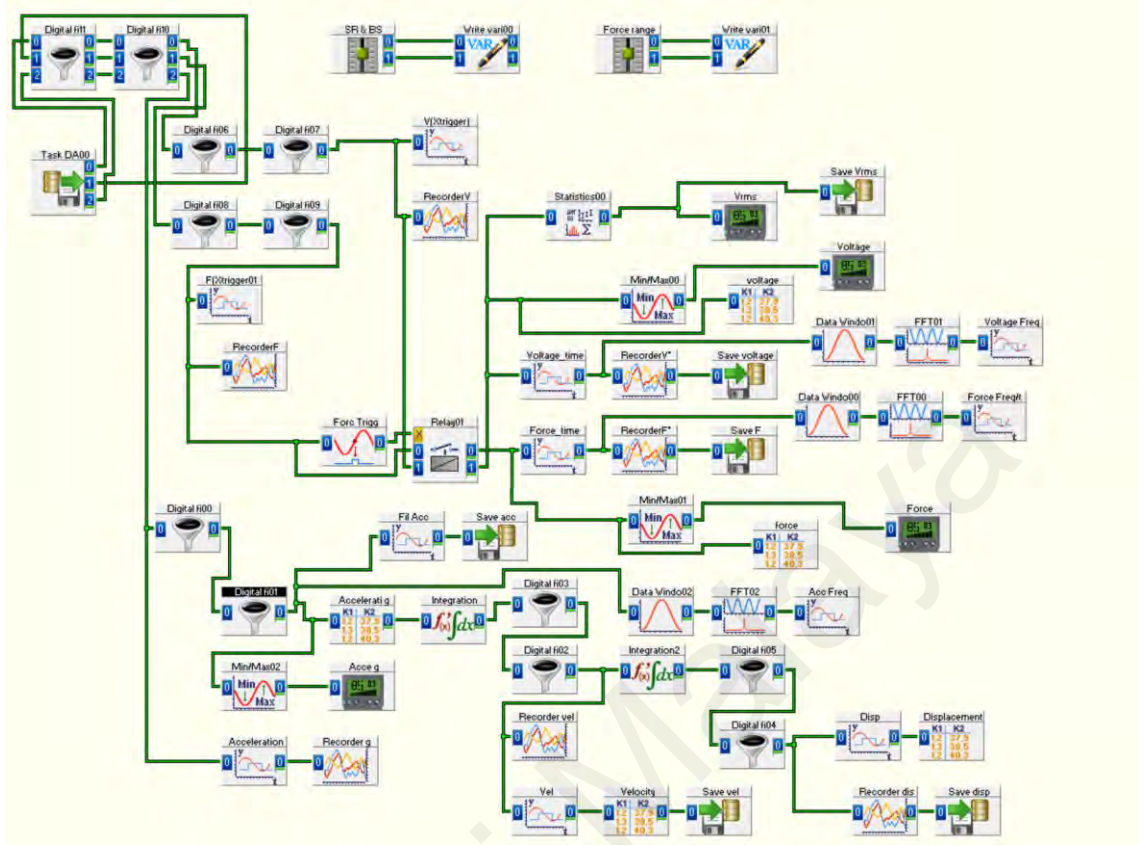
(b)
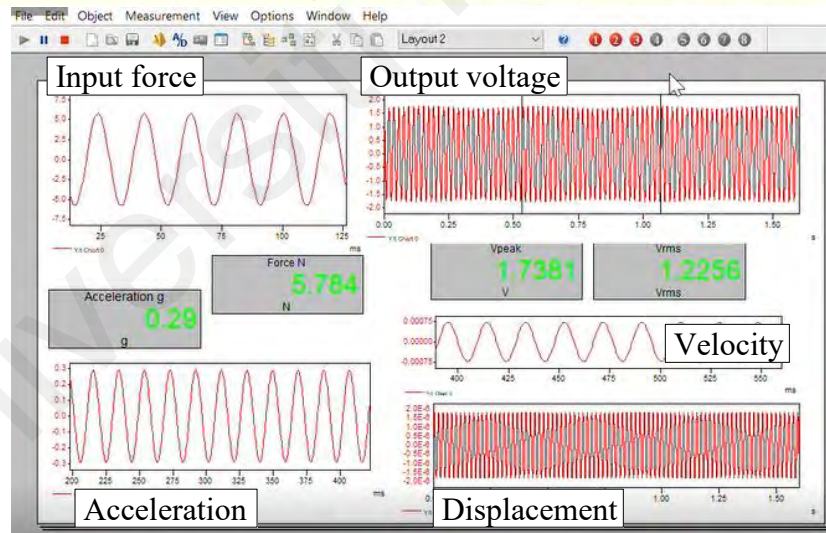
Figure 3.10 (a) Worksheet and (b) layout in DASYLab$^{TM}$ to examine the energy conversion efficiency of developed PEH under harmonic force

# CHAPTER 4: RESULT AND DISCUSSION

## 4.1 Concept Generation on Novel Amplifier Structure

After a deep study and close investigation on the various types of amplification frame, the mechanism of the force amplification structure has been examined. It can be clearly noticed that the main manipulation factor of the flexure typed amplifier structure is the flexure hinge with a certain angle. As a result, the common characteristic for the first generation of flextensional structure is the isosceles trapezoidal shape of the cavity. For instance, this characteristic can be observed from the front view of the Cymbal and Rectangular Cymbal structures. The general structure of the frame is constructed from two inclined planes connected to the centre loading force plane. Hence, the trapezoidal-shaped cavity will have a shorter upper boundary. When a compressive loading force is applied, the frame especially the flexure hinge will deform and extend the lower part of the cavity.

To implement a tensile force onto the PZT, the position of the PZT should be placed exactly at the middle under the flextensional frame. In contrast, the PZT should be placed outside the frame with fixed support to obtain the compressive effect as shown in Figure 4.1. On the other hand, the compressive effect on the PZT can be achieved by changing the direction of the loading force. An outward pulling force should be applied at the apex of the end cap instead of a compressive loading force so that the PZT which is placed under the cavity will be compressed by the shrunk end cap. In short, the deforming effect either in tension or compression depends on the location of the PZT and the direction or type of loading force through a flextensional amplifier structure. However, the flextensional structure has the common disadvantages of having restricted cavity height and linkage length due to the PZT size which may limit the amplification effect. Besides, only a small forcing area is provided at the apex of the flextensional or current

91

flexcompressive structures. Furthermore, PZT in tension may have a lower stress limit and power output due to its low tensile yield strength.
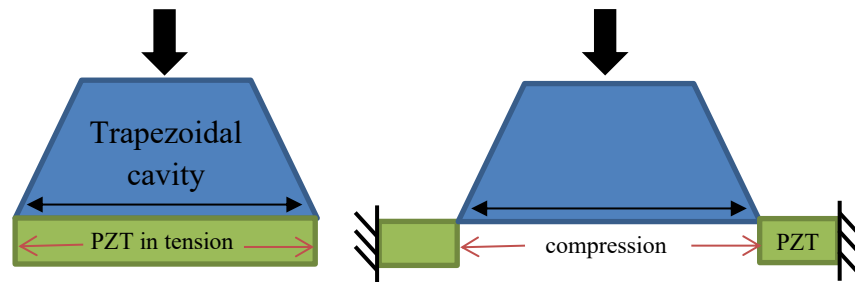


Figure 4.1 Type of loading force implemented on the PZT based on the location of PZT through the flextensional amplifier structure with trapezoidal cavity

Therefore, a compressive inward loading force with a PZT fixed at the centre is always preferred. A novel idea to induce the PZT under a compressive force with an innovative structural design has been proposed. It can be done by inverting the trapezoidal cavity with proper frame design as shown in Figure 4.2 (a). This design has a larger loading force area which allows excitation source with a larger forcing area. A wider loading area can be provided as well with the elongated base design. For example, a commercial sedan car with a wheel width between 175 to 245 cm range or a human foot length is capable to transmit all the energy to the PZT through this frame without any waste. In other words, it has a great advantage to ease the transformation of loading energy, especially from vehicle excitation and human foot strike. No additional plate or casing is needed for forcing excitation with a larger base area such as the wheel, making it more suitable for vehicle excitation application. Hence, this design is expected to have higher energy conversion efficiency and more suitable for high force roadway applications than other existing designs.

This inverted trapezoidal compressive design is named as Hull structure due to its similar shape with the front view of a boat hull. Based on the proposed cavity shape, the conceptual design of the Hull end cap is shown in Figure 4.2 (b). Two end caps are used to sandwich the PZT plate so that the compressive effect will be doubled as shown in

Figure 4.2 (c). The Hull structure end cap is bonded with the PZT plate at the joint. The loading force is applied at the top forcing area while the bottom base is fixed on the ground.
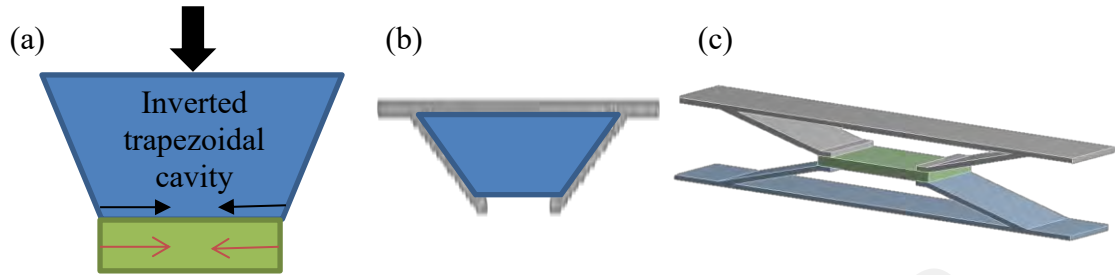


Figure 4.2 (a) Compressive effect on the PZT through the amplifier structure with inverted trapezoidal cavity; (b) Conceptual design of Hull structure based on inverted trapezoidal cavity; (c) Hull structure

Basic parameters such as inclined angle, linkage thickness, joint length, and cavity height, will be optimized. Each parametric effect on the amplification factor will be examined and discussed in Section 4.2. Additional features such as joint design, elongated base length, and fillet have been added and examined via FEA. It is believed that these features can enhance the previous design such as reducing the stress concentration issue with additional fillets at the corners. Unlike the conventional flextensional structures, the linkage length and cavity height of the Hull structure is not restricted by the frame design. Thus, the Hull structure has higher flexibility in the design dimension to suit many applications either to be huge or in a compact design.

### 4.1.1    Finite Element Analysis (FEA)

Before carrying out the FEA simulation for the proposed new structures, it is vital to validate the FEA setting with a benchmark study in order to ensure the accuracy of the FEA result. A commercial tensile-typed Rectangular Cymbal PEH study from (Kuang et al., 2017) is selected, not only to corroborate the FEA settings but also as a benchmark case for the comparison on the energy harvesting performance with the proposed Hull PEH at a later stage.

### 4.1.1.1 Validation of FEA setting

To verify the FEA setting, a Rectangular Cymbal PEH is constructed and optimized in the developed FEA environment. It is then compared with the benchmark study (Kuang et al., 2017) under the same forcing function, which is 1 kN sinusoidal force at 2 Hz. Figure 4.3 (a) and (b) shows the comparison between the stress distribution obtained from this study and the benchmark case (Kuang et al., 2017) by using the same substrates thickness of 0.6 mm.
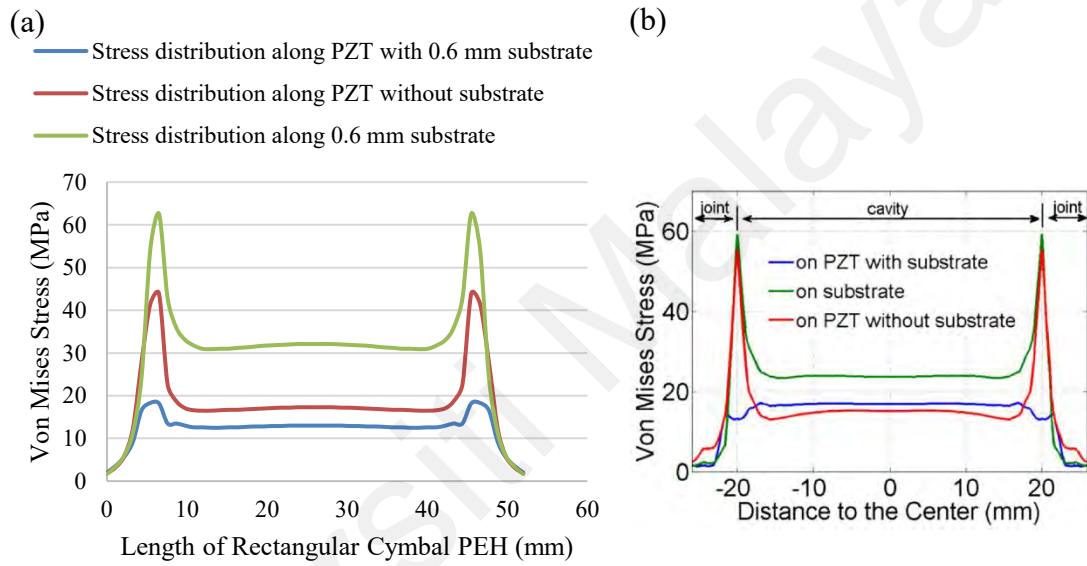


Figure 4.3 Comparison on the stress distribution of a Rectangular Cymbal PEH obtained from (a) this study and (b) a benchmark study (Kuang et al., 2017)

A similar trend of stress distribution is found in both studies, where it shows the presence of substrate has successfully shifted the stress concentration from the PZT plate to the substrate. However, a slight deviation of stress value is gained from this study, where the maximum stress on the PZT with 0.6 mm substrate is more than the stress limit of 17.5 MPa by taking a safety factor of 2. Hence, a thicker substrate is needed to protect the PZT from mechanical failure. This leads to a slightly different optimum substrate thickness, i.e., 0.7 mm in this study but 0.6 mm from (Kuang et al., 2017). It is due to a different version of ANSYS software, such as R18.2 has been used throughout this study but R14.5 is used in (Kuang et al., 2017). As a result, a Rectangular Cymbal PEH with a

thicker substrate will produce a lower power output of 3.68 mW, if compare with the benchmark study of 5.15 mW. Nonetheless, a higher version of FEA software used in this study should be more precise in the simulation with a finer meshing setting (proven in Section 4.4.1, corroboration with experimental impact result). Therefore, similar FEA settings will be used for the simulation of the proposed compressive Hull PEH. To ensure a fair comparison with the benchmark structure, the Rectangular Cymbal PEH with 0.7 mm optimum substrate thickness will be continually used throughout this study. Figure 4.4 shows the stress distribution of the PZT plate obtained from this study for the benchmark Rectangular Cymbal structure with 0.7 mm substrate.
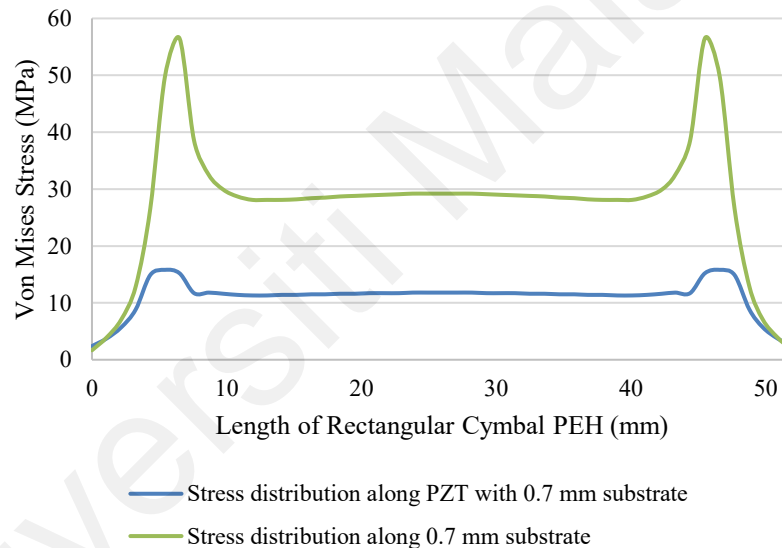


Figure 4.4 Stress distribution for the Rectangular Cymbal PEH to demonstrate the presence of 0.7 mm substrate in shifting the stress level of the PZT

### 4.1.1.2 FEA results for each proposed structural design

The FEA results for each proposed design and feature under 1kN sinusoidal force at 2 Hz are summarized in Table 4.1. The material yield strength is the first barrier to prevent any failure such as cracking or permanent plastic deformation. By taking a safety factor of 2, the PZT material has a tensile yield stress limit of 17.5 MPa and a compressive yield stress limit of 10 times its tensile value. The design with excessive maximum PZT or end cap stress will be eliminated.

Based on the power output and the PZT stress, the performance of each design is discussed and justified. In this study, the average nodal stress of the PZT is reported as many studies only focus on the maximum stress level to avoid failure occurs. In fact, the performance of the frame depends on the level of utilization of the PZT material which is indicated by the average nodal stress of the PZT. Hence, a linear relationship can be observed between power output and the PZT stress in Figure 4.5.

Table 4.1 FEA simulation results for each structural design

| Design description and illustration | Max. PZT stress (MPa) | Avg. PZT nodal stress (MPa) | Max. frame stress (MPa) | Power output (mW) | Pros (+) and cons (-) of the fame design and its justification |
|---|---|---|---|---|---|
| **(a) Tensile Rectangular Cymbal structure:** **(Benchmark case)**<br>• With dual-layer of 0.7 mm substrates<br>• 3.8 mm cavity height (Small)<br>• 6 mm joint length<br>• 14 mm apex length<br> | 17.5 | 8.74 | 124.41 | 3.68 | - Power generation of this design had reached its limit based on the maximum PZT stress value (17.5 MPa).<br>- Restricted cavity height and linkage length may limit the amplification effect.<br>- Only a small forcing area is provided at the apex of the end cap. Additional casing or plate is needed.<br>+ Suitable for limited space application such as under shoes. |
| **(b) Compressive Hull structure:** **i. Full covered joint design** | | | | | |
| • The cavity size is enlarged by a scale factor of 2.85 based on the benchmark structure<br>• 10.47 mm cavity height (Large)<br>• Total base length of 186.14 mm<br>• Extended 20 mm base at both ends<br> | 53. 3 | 9.87 | 389.51 | 2.15 | + Fully adhesive covered design at the entire joint leads to a stronger bonding effect.<br>+ Larger base area which is suitable for roadway application.<br>- Lower power output than the benchmark case even with a larger cavity size. The full covered joint design has restricted the compressive deformation of the linkage, causing less compressive energy transformed to the PZT. |
| • Shorter cavity height, 2 mm<br>• Extended 6 mm base at both ends<br> | 32.4 | 3.85 | 180.79 | 0.083 | - Much lower power output due to the restricted deformation design.<br>- Amplification effect is weak with a shorter cavity height, which can be observed from the low average PZT nodal stress value. |
| • Thinner joint design at the middle<br> | 29.0 | 4.57 | 181.26 | 0.091 | - Much lower power output due to the restricted deformation design even with a thinner joint.<br>- Amplification effect is weak which can be observed from the low average PZT nodal stress value. |

| Design description and illustration | Max. PZT stress (MPa) | Avg. PZT nodal stress (MPa) | Max. frame stress (MPa) | Power output (mW) | Pros (+) and cons (-) of the fame design and its justification |
|---|---|---|---|---|---|
| **(b) Compressive Hull structure:**<br>**ii. Partial bonded joint design** | | | | | |
| • The cavity size is enlarged by a scale factor of 2.85 based on the benchmark structure<br>• 10.47 mm cavity height (Large)<br>• Extended 20 mm base at both ends<br>• Total base length of 186.14 mm<br>• 6 mm joint length<br>• Standard dimension for other design<br> | 51.6 | 23.8 | 399.41 | 6.37 | + Almost double up the power output of the benchmark case. Average PZT nodal stress has been increased, showing a great amplification effect from the compression force.<br>+ Higher power output than the full covered joint design as the inclined linkages transmit the compressive force well through the two discrete joints.<br>+ Linkage length and cavity height are not restricted by the frame design.<br>+ Larger base area which is suitable for roadway application.<br>- Small joint area. (which can be solved by applying a good adhesive similar to the benchmark case) |
| • 7.2 mm cavity height (Medium)<br> | 34.2 | 18.6 | 312.76 | 5.21 | + Higher power output than the benchmark case.<br>- Lower power output than the large cavity design. (indicates the cavity height or linkage length is one of the main factors of power amplification) |
| • 3.8 mm cavity height (Small)<br> | 27.2 | 11.6 | 197.04 | 1.79 | - Lower power output than the benchmark case and the larger cavity design. |
| • Standard dimension with dual-layer of 0.6 mm substrates<br> | 35.4 | 14.4 | 398.52 | 3.15 | - Substrates have shielded some of the compressive energy that transmitted to the PZT, leading to lower power output.<br>+ Indicates substrate is unessential in compressive frame design as the PZT stress level is far from its compressive yield strength. |

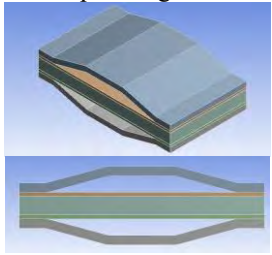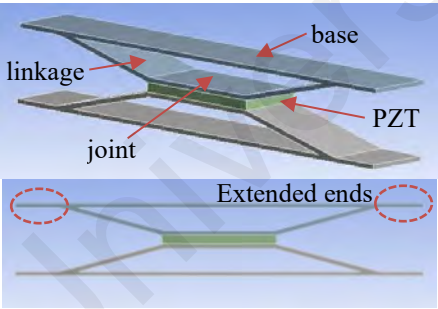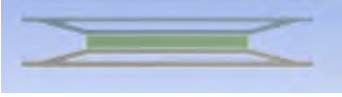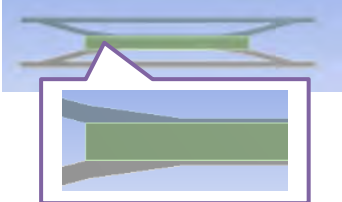| Design description and illustration | Max. PZT stress (MPa) | Avg. PZT nodal stress (MPa) | Max. frame stress (MPa) | Power output (mW) | Pros (+) and cons (-) of the fame design and its justification |
|---|---|---|---|---|---|
| **(b) Compressive Hull structure:**<br>**iii. Elongated base design** | | | | | |
| • Large cavity height<br>• Elongated 50 mm base length from the standard design at both ends<br> | 46.9 | 28.0 | 426.94 | 14.5 | + Almost 4 times higher than the power output of the benchmark case.<br>+ Elongation in base length will exert another moment which enhances the compressive effect.<br>+ Base length can be further extended. |
| • Medium cavity height<br>• Elongated base length to standard 186.14 mm<br> | 30.9 | 20.8 | 263.14 | 7.02 | + Higher power output than the large and medium cavity height cases.<br>+ Elongated base (the extended ends) will have greater amplification effect than increasing the cavity height. |
| **(b) Compressive Hull structure:**<br>**iv. Fillet design with constant standard dimension** | | | | | |
| • Add fillet at the contact area of the frame with PZT<br> | 54.8 | 24.1 | 383.96 | 7.38 | + Higher power output.<br>+ Higher PZT stress level.<br>+ Lower maximum frame stress.<br>+ Fillet reduces the stress concentration at the contact area. |
| • Add fillet at linkage part of the frame<br> | 55.9 | 24.4 | 377.58 | 6.80 | + Higher power output.<br>+ Higher PZT stress level.<br>+ Lower maximum frame stress.<br>+ Fillet reduces the stress concentration at the linkage part. |
| • Add fillet at both contact area with PZT & linkage part of the frame<br> | 57. 4 | 23. 2 | 1274.6 | 6.85 | + Higher power output than the benchmark case.<br>- Lower power output than the only add fillet at the contact area.<br>- Much higher maximum frame stress.<br>- Fillet at both areas does not produce higher power or reduce the frame stress as expected. |
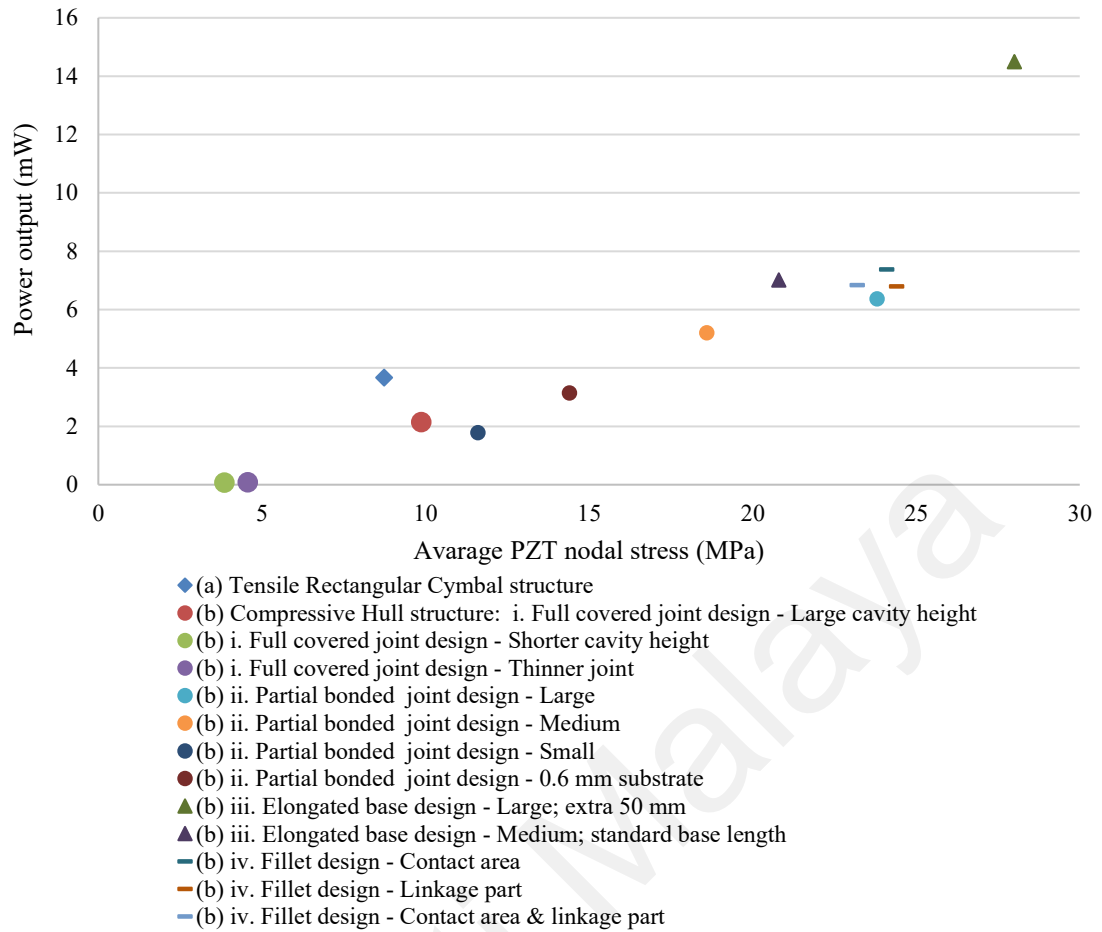
Figure 4.5 Power output versus average PZT nodal stress graph for different designs

In summary, the Hull structure with a fully covered joint design has the lowest power output as shown in Figure 4.5. This is because it restricts the compressive deformation of the frame which leads to less energy transformed to the PZT. In contrast, the partial bonded joint design has a great amplification effect as the inclined linkages transmit the amplified compressive force well to the PZT through the two discrete joints. A larger cavity height or longer linkage length is preferred to boost the power output. This is also another advantage of the new design over the benchmark case as the linkage length and cavity height are not restricted by the frame design. Moreover, it provides a larger base area, which is suitable for high force application. Further elongation on the base length also shows a positive effect on the power output. This is due to the applied moment on the PZT which enhances the compressive effect. The result shows that elongating the base

through the extended ends may have a greater amplification effect than increasing the cavity height.

Since the compressive yield strength of PZT is much higher than its tensile yield strength, the PZT plate with a compressive frame can be further compressed and optimized to achieve greater power output. An additional substrate is not necessary in this case as the PZT stress level is far from its compressive yield strength. Furthermore, adding fillet at the contact area and linkage part will reduce the stress concentration that happens at the frame due to discontinuity. Therefore, enlarged compressive energy can be transmitted to the PZT and greater power will be generated. A much higher level of utilization of the PZT material has been realized in the proposed Hull compressive structure (up to the level of 20 MPa if compared with the benchmark case which has only 8 MPa) within the stress limit of the frame and PZT material. It is believed that the Hull structure has a huge potential to be further optimized in order to harvest a greater power output.

### 4.1.2  Analytical Modeling

In this section, an analytical model is developed in order to determine the effectiveness of the compressive Hull structure in terms of its force amplification factor. The mathematic model is developed based on the kinematic theorem as well as the deformation of the frame, which is often ignored by some researchers (Wen et al., 2018). The parameters of the structure and the simplified mechanism are presented in Figure 4.6. A quarter of the amplifier structure is considered on its right upper flexure beam AB due to its double symmetry on the design.
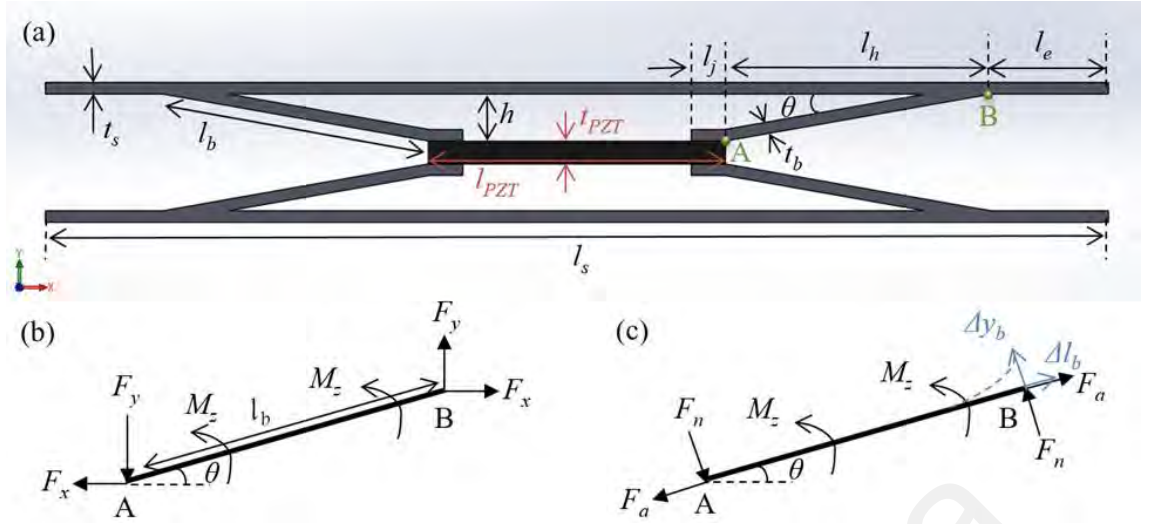
Figure 4.6 (a) Parameters of the Hull structure; (b) Simplified linkage quarter mechanism at xy-axis and (c) at its neutral axis

The normal force, $F_n$ and axial force, $F_a$ along the beam axis can be calculated from the vertical input force, $F_y$ and horizontal output force, $F_x$ by considering the force equilibrium at point A.

$$F_n = F_y \cos\theta - F_x \sin\theta \qquad [4.1]$$

$$F_a = F_y \sin\theta + F_x \cos\theta \qquad [4.2]$$

where $\theta$ is the inclined angle.

Considering the moment equilibrium at point A, $M_z$, which is the supplemented moment to ensure the deflection angles at both ends of the link AB remain zero, can be calculated as follow:

$$2M_z = F_x l_y - F_y l_x \qquad [4.3]$$

$$= F_x \, l_b \sin\theta - F_y \, l_b \cos\theta$$

$$M_z = \frac{(F_x \sin\theta - F_y \cos\theta)l_b}{2}$$

$$= -\frac{F_n l_b}{2} \qquad [4.4]$$

Based on the Euler-Bernoulli beam theory, the bending equation of the linkage is shown in equation [4.6] by considering $M(r)$, the moment at end point B.

$$M(r) = F_n r + M_z, \qquad 0 \le r \le l_b \qquad [4.5]$$

$$\frac{d^2 y_b}{dl^2} = \frac{M(r)}{EI} \qquad [4.6]$$

$$\Delta y_b = \frac{1}{EI} \int_0^{l_b} \int_0^r \left( F_n \xi - \frac{F_n l_b}{2} \right) d\xi dr$$

$$= -\frac{F_n l_b^3}{12EI} \qquad [4.7]$$

where $\Delta y_b$ is the perpendicular deflection of the beam from the neutral axis, $E$ is the Young's modulus of the frame material, and $I$ is the area moment of inertia. $r$ is the localized length function for the beam, while $\xi$ is the corresponding dummy variable.

Next, the deformation of the linkage with respect to the neutral axis caused by the input axial force can be obtained as follow. It is governed by the translational stiffness.

$$\Delta l_b = \frac{F_a l_b}{EA} \qquad [4.8]$$

where $A$ denotes the cross-sectional area of the linkage.

From the Hooke's law, the deformation of PZT plate in x-axis is calculated as:

$$\Delta x_{pzt} = \frac{F_x l_{pzt}}{E_{pzt} A_{pzt}} \qquad [4.9]$$

Lastly, the relationship between equations [4.7] – [4.9] can be linked since the total deformation along the x-axis is zero based on the theorem of compatibility condition.

$$\Delta y_b \sin\theta + \Delta x_{pzt} = \Delta l_b \cos\theta \qquad [4.10]$$

$$-\frac{l_b^3 \sin\theta}{12EI} \left( F_y \cos\theta - F_x \sin\theta \right) + \frac{F_x l_{pzt}}{E_{pzt} A_{pzt}} = \frac{l_b \cos\theta}{EA} \left( F_y \sin\theta + F_x \cos\theta \right)$$

The force amplification factor, $\alpha$ is derived from equation [4.10] as:

$$\alpha = \frac{F_x}{F_y} = \frac{-\dfrac{l_b{}^3 \sin\theta \cos\theta}{12EI} - \dfrac{l_b \cos\theta \sin\theta}{EA}}{\dfrac{l_b \cos^2\theta}{EA} - \dfrac{l_b{}^3 \sin^2\theta}{12EI} - \dfrac{l_{pzt}}{E_{pzt}A_{pzt}}} \qquad [4.11]$$

## 4.2    FEA Parametric Optimization

Parametric optimization has been carried out based on the conceptual design of the Hull structure to obtain an optimal design with enhanced power output. Parameters such as inclined angle, linkage length, joint length, base length, base thickness, and linkage thickness will be optimized one at a time while the other parameters will be kept constant. A safety factor of 2 is taken on the compressive yield strength for the PZT and frame as the design criteria in the FEA simulation. Thus, 175 MPa is set as the PZT stress limit while 380 MPa is set for the frame design by considering Ti or processed stainless steel as the frame material. The parameters of the Hull structure are illustrated in Figure 4.6 (a).

In the parametric optimization of flexcompressive or flextensional structure, the adjustments are mainly made on the cavity size. It is manipulated by four main variables, namely the inclined angle, cavity height, linkage length, and horizontal linkage length. These four variables are linked by a trigonometry relationship. In general, one variable is fixed at one time while changing the other three variables to investigate the effect of these parameters on the power amplification.

However, the optimization in the benchmark tensile-typed Rectangular Cymbal is different where it has a restricted frame design by the PZT size. The horizontal linkage length is restricted by its PZT length when the joint length and apex length are fixed. In other words, only the inclined angle (with the corresponding changes in cavity height and linkage length) has been optimised during the parametric optimization for the Rectangular

Cymbal structure since the horizontal linkage length is fixed (Kuang et al., 2017). An illustration on this optimization of inclined angle is shown in Figure 4.7.
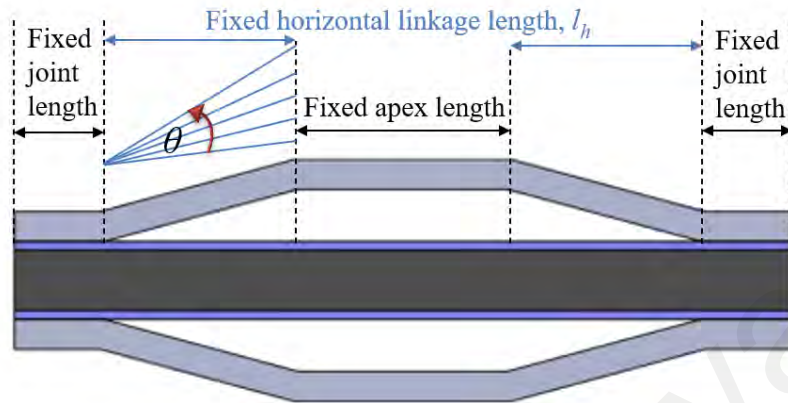
Figure 4.7 Optimization on the inclined angle of the Rectangular Cymbal structure

On the other hand, as mentioned in Section 4.1, one of the benefits of the Hull structure is that the frame size has no limit as long as the application can compromise. Hence, this makes the Hull structure different from the Rectangular Cymbal structure during the optimization. Figure 4.8 illustrates the four possible parametric optimizations on the Hull structure regarding the inclined angle and linkage length. One of the variables is fixed while altering the other three variables.
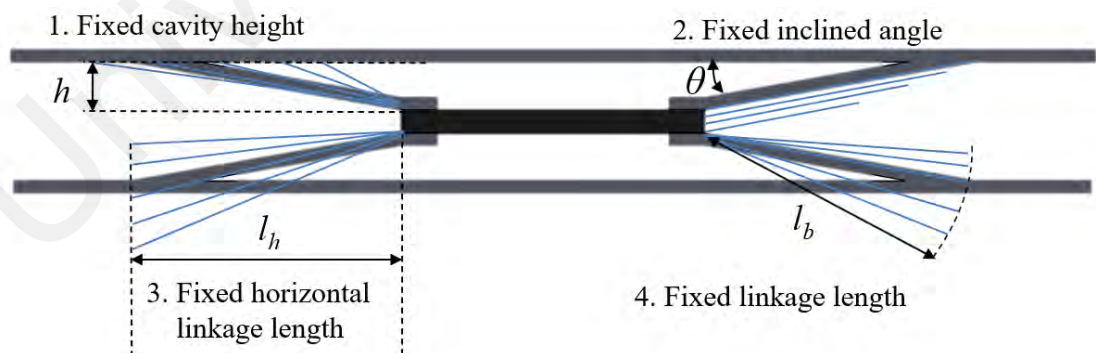
Figure 4.8 Four possible parametric optimizations on the Hull structure regarding the inclined angle and linkage length

The first adjustment is made on the inclined angle, linkage length, and horizontal linkage length by keeping the cavity height constant at 6 mm. An initial value is set for

other parameters such as 6 mm of joint length, 2 mm of base thickness, 2 mm of linkage thickness, and 20 mm of extended base length as listed in Table 4.2.

Table 4.2 Initial value for each parameter of a Hull structure

| Parameters | Symbol | Initial value |
|---|---|---|
| PZT length (mm) | $l_{PZT}$ | 52 |
| PZT thickness (mm) | $t_{PZT}$ | 4 |
| Width (mm) | $w$ | 30 |
| Base length (mm) | $l_s$ | 263.6 |
| Base thickness (mm) | $t_s$ | 2 |
| Linkage thickness (mm) | $t_b$ | 2 |
| Cavity height (mm) | $h$ | 6 |
| Linkage length (mm) | $l_b$ | 86 |
| Horizontal linkage length (mm) | $l_h$ | 85.8 |
| Extended base length (mm) | $l_e$ | 20 |
| Joint length (mm) | $l_j$ | 6 |
| Inclined angle (˚) | $\theta$ | 4 |

## 4.2.1 Relationship Between the Hull PEH's Structural Parameters and Its Harvesting Performance

The relationship of each parameter on the power output and amplification effect will be examined and discussed in this section.

### 4.2.1.1 Effect of inclined angle and linkage length with fixed cavity height

Table 4.3 shows the FEA results including the power output and maximum stress on the PZT as well as end cap (EC) for the adjustment on the inclined angle from 4˚ to 50˚ and the corresponding horizontal linkage length. The maximum stress values that exceed the stress limit are highlighted in red in Table 4.3 and eliminated first. Then, the combination with the highest power output among the remaining pairs is considered the optimum dimension. Even though the power output of a smaller angle with linkage length larger than 60 mm is greater, but higher stress is accumulated on the frame and caused it to fail. Hence, 6˚ is selected as the optimum inclined angle in this structure.

Table 4.3 FEA results with adjustment on the inclined angle and horizontal linkage length of the Hull structure with fixed cavity height

| Angle (°) | Corresponding horizontal linkage length (mm) | Corresponding linkage length (mm) | Power output (mW) | PZT's maximum stress (MPa) | EC's maximum stress (MPa) |
|---|---|---|---|---|---|
| 4 | 85.804 | 86.01 | 21.574 | 359.53* | 1388.70* |
| 5 | 68.580 | 68.84 | 10.819 | 95.30 | 441.87* |
| **6** | 57.086 | 57.40 | **6.132** | 71.09 | 319.38 |
| 7 | 48.866 | 49.23 | 4.084 | 69.15 | 260.75 |
| 8 | 42.692 | 43.11 | 3.395 | 62.33 | 235.57 |
| 10 | 34.028 | 34.55 | 1.951 | 55.46 | 223.90 |
| 20 | 16.485 | 17.54 | 0.334 | 38.50 | 182.35 |
| 30 | 10.392 | 12.00 | 0.105 | 29.97 | 134.19 |
| 40 | 7.151 | 9.33 | 0.037 | 24.33 | 125.46 |
| 50 | 5.035 | 7.83 | 0.012 | 20.14 | 116.41 |

*denotes value exceeded stress limit; 'bolded' value indicates the optimum dimension*
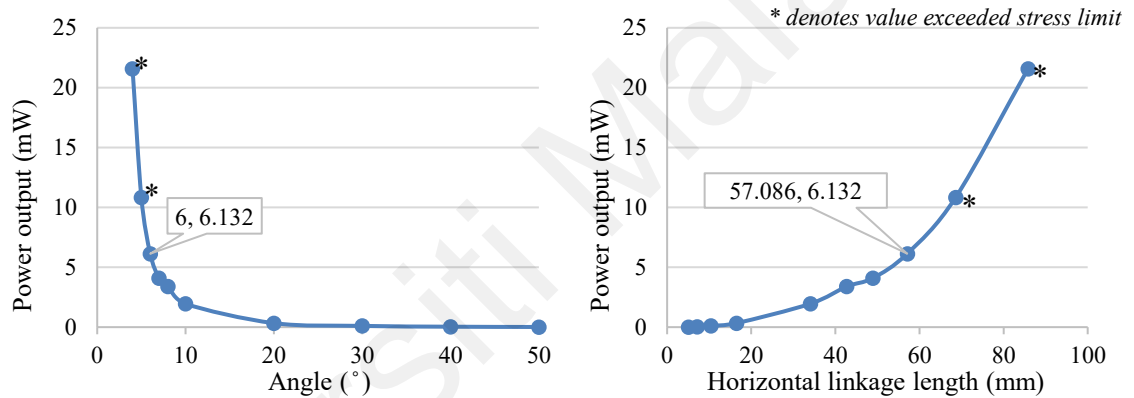


Figure 4.9 Power output of the PEH as a function of (a) inclined angle and (b) horizontal linkage length of a Hull structure with fixed cavity height

On the other hand, a drastic drop in power output can be observed from Figure 4.9 (a) as the angle increases, especially from 4° to 10°. This shows that the amplification effect is not obvious when the inclined angle is greater than 10°. Also, smaller angle with longer linkage has greater amplification factor when the cavity height is fixed. A magnified compressive force is transmitted to the PZT through the longer linkage which leads to higher power output.

### 4.2.1.2 Effect of inclined angle and linkage length with fixed inclined angle

The result for a range of cavity height from 3 to 8 mm is being investigated with its corresponding horizontal linkage length and corresponding linkage length as shown in

Table 4.4. Same initial values are used in this simulation except for the inclined angle which is fixed at 6˚.

Table 4.4 FEA results with adjustment on the cavity height and horizontal linkage length of the Hull structure with fixed inclined angle

| Cavity height (mm) | Corresponding horizontal linkage length (mm) | Corresponding linkage length (mm) | Power output (mW) | PZT's maximum stress (MPa) | EC's maximum stress (MPa) |
|---|---|---|---|---|---|
| 3 | 28.58 | 28.70 | 0.762 | 45.142 | 155.07 |
| 4 | 38.01 | 38.27 | 2.409 | 70.283 | 211.26 |
| 5 | 47.61 | 47.83 | 4.649 | 73.116 | 253.77 |
| **6** | 57.12 | 57.40 | **6.112** | 63.069 | 337.34 |
| 7 | 66.64 | 66.97 | 8.410 | 94.92 | 415.74* |
| 8 | 76.15 | 76.53 | 10.812 | 118.86 | 433.26* |

*\* denotes value exceeded stress limit; 'bolded' value indicates the optimum dimension*
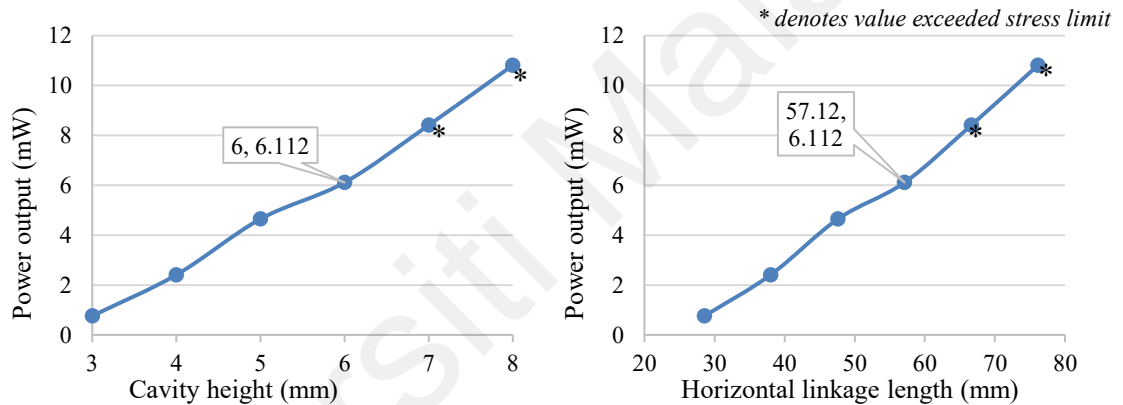


Figure 4.10 Power output of the PEH as a function of (a) cavity height and (b) horizontal linkage length of a Hull structure with fixed inclined angle

As the cavity height increases, a greater cavity size with longer linkage will be formed. Hence, the amplification effect and power output will be magnified. A linear relationship of these parameters can be observed in Figure 4.10. The structure with cavity height less than 6 mm has lower frame stress under 350 MPa. Again, structure with horizontal linkage length larger than 60 mm will fail as mentioned in the previous section. Based on the safety aspect, the PEH with 6 mm of cavity height has produced the highest power output. However, a shorter cavity height is favourable to ease the installation process. For example, it is more suitable for roadway application with shallower bury depth.

### 4.2.1.3 Effect of joint length

Next, the cavity height is fixed at 6 mm while the inclined angle is kept constant at 6°. The joint length is then increased from 3 to 10 mm and the FEA results are tabulated in Table 4.5 and plotted in Figure 4.11.

Table 4.5 FEA results with adjustment on the joint length of the Hull structure

| Joint length (mm) | Power output (mW) | PZT's maximum stress (MPa) | EC's maximum stress (MPa) |
|---|---|---|---|
| 3 | 6.04 | 87.50 | 311.46 |
| 4 | 6.11 | 78.25 | 316.08 |
| 5 | 6.15 | 74.44 | 319.20 |
| 6 | 6.13 | 71.09 | 319.38 |
| **7** | **6.16** | 74.02 | 316.19 |
| 8 | 6.04 | 80.31 | 319.22 |
| 9 | 5.89 | 77.84 | 319.21 |
| 10 | 5.86 | 76.69 | 318.82 |

*'bolded' value indicates the optimum dimension*
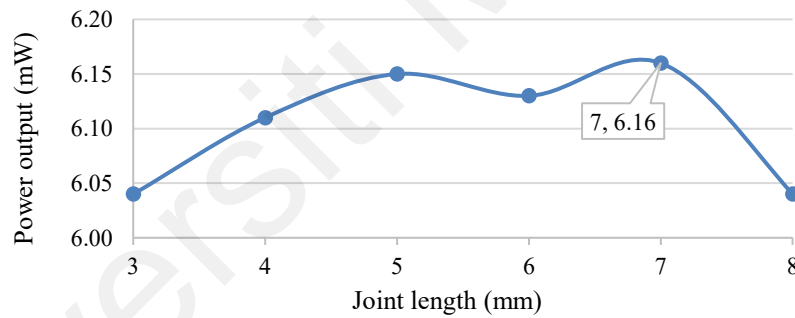


Figure 4.11 Power output of the PEH as a function of the joint length of a Hull structure

From Figure 4.11, there is an optimum joint length where an extremely short joint may lead to a weak bond. High stress concentration can be observed at the edge of PZT which bonded with the joint. In contrast, longer joint may cause a lower power output as the joining area is larger which restricts a larger portion of PZT from deformation. However, the joint length has a minor effect on power output and stress distribution if compared to other parameters in this design. Hence, an optimum joint length of 7 mm is selected based on the power output.

### 4.2.1.4 Effect of extended base length

With the optimum joint length obtained from the previous section, the joint length is fixed at 7 mm in this simulation. The Hull structure is then modified with an extended base at both ends. The effect of the extended base length is being investigated. The FEA results are shown in Table 4.6 and Figure 4.12.

Table 4.6 FEA results with adjustment on the extended base length of the Hull structure

| Extended base length (mm) | Power output (mW) | PZT's maximum stress (MPa) | EC's maximum stress (MPa) |
|---|---|---|---|
| 0 | 4.59 | 87.75 | 404.64* |
| 10 | 5.29 | 82.44 | 356.02 |
| **20** | **6.05** | 77.50 | 314.38 |
| 30 | 7.11 | 68.44 | 312.99 |
| 40 | 8.25 | 69.10 | 249.96 |

*\* denotes value exceeded stress limit; 'bolded' value indicates the optimum dimension*
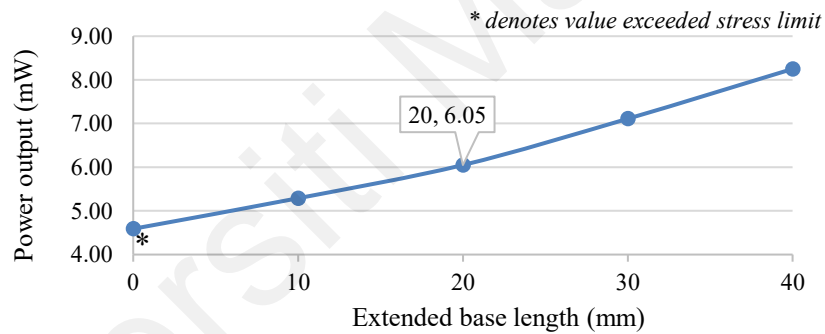


Figure 4.12 Power output of the PEH as a function of the extended base length of a Hull structure

Higher stress is observed at the frame with a smaller base area since the same forcing function is applied. However, the power output does not increase with the maximum stress values. This is because the maximum stress value is caused by the high stress concentration that is found at the PZT plate with the smaller base area, but the overall PZT stress distribution is uneven. The PZT is not fully utilized as the compressive force is not enhanced by the frame with shorter or non-extended base. Excessive frame stress of 404.64 MPa can be observed due to discontinuity of the frame when there is no extended base. Thus, the extended base is beneficial as a larger forcing area is provided to withstand larger stress.

Figure 4.12 shows that the power output increases as the extended base length increases. More even stress distribution can be observed throughout the PZT as the extended base length increases which amplify the power output at the meanwhile. However, 20 mm is chosen as the extended length so that a total base length which is less than 200 mm can be achieved. This is to ensure that the excitation force from the vehicle's tire can be fully transmitted through the amplifier structure to the PZT.

**4.2.1.5 Effect of base and linkage thickness**

After optimised the length of the base, linkage and joint of the Hull structure, the base and linkage thickness are optimised next. The thickness is adjusted from 1.5 to 3.0 mm with 0.5 mm increment for both parameters. The results are shown in Table 4.7 and Figure 4.13. The optimised thickness is found at 2 mm for both base and linkage thickness.

Table 4.7 The effect of base thickness, $t_s$ and linkage thickness, $t_b$ of the Hull structure on (a) PZT's maximum stress, (b) EC's maximum stress, and (c) power output

| (a) PZT's maximum stress (MPa) | | | | |
|---|---|---|---|---|
| $t_b$ (mm) / $t_s$ (mm) | 1.5 | 2.0 | 2.5 | 3.0 |
| 1.5 | 126.76 | 72.33 | 65.64 | 62.41 |
| 2.0 | 133.70 | 77.50 | 66.77 | 62.00 |
| 2.5 | 136.55 | 80.36 | 65.12 | 60.37 |
| 3.0 | 136.38 | 81.75 | 65.24 | 57.76 |

| (b) EC's maximum stress (MPa) | | | | |
|---|---|---|---|---|
| $t_b$ (mm) / $t_s$ (mm) | 1.5 | **2.0** | 2.5 | 3.0 |
| 1.5 | 489.17* | 427.00* | 426.08* | 376.70* |
| **2.0** | 590.85* | **314.38** | 277.74 | 226.21 |
| 2.5 | 580.56* | 337.83 | 195.45 | 159.85 |
| 3.0 | 602.78* | 352.11 | 192.29 | 129.80 |

| (c) Power output (mW) | | | | |
|---|---|---|---|---|
| $t_b$ (mm) / $t_s$ (mm) | 1.5 | **2.0** | 2.5 | 3.0 |
| 1.5 | 12.61 | 7.05 | 5.40 | 3.46 |
| **2.0** | 11.88 | **6.05** | 4.56 | 2.94 |
| 2.5 | 11.84 | 5.61 | 4.11 | 2.73 |
| 3.0 | 11.37 | 5.46 | 3.90 | 2.51 |

*denotes value exceeded stress limit; 'bolded' value indicates the optimum dimension*
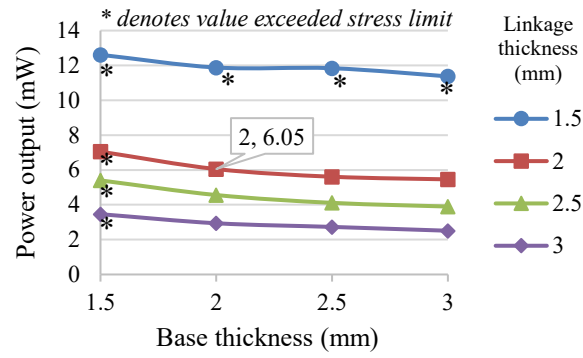
Figure 4.13 Power output of the PEH as a function of the base thickness with different linkage thickness of a Hull structure

As shown in Table 4.7 (a), the PZT works safely under 1.5 to 3.0 mm range of frame thickness. But the maximum frame stress with 1.5 mm linkage thickness or base thickness has exceeded the stress limit as shown in Table 4.7 (b). Hence, 2 mm is selected as the base and linkage thickness since it has the highest power output of 6.05 mW. Both the linkage and base thickness have a greater effect on the stress level as the thickness will directly affect the cross-sectional area. Hence, a thicker base or linkage will result in a lower maximum stress value. In other words, thicker base or linkage can withstand a higher force.

However, increment in thickness will shield most of the stress from the PZT, causing less PZT deformation and power output as shown in Figure 4.13. Linkage thickness has a greater effect as compared with the base thickness in terms of both the stress level and the power output. This is because the internal force at the linkage has been magnified through the inclined angle while the base is only applied with the unamplified input force.

### 4.2.1.6 Effect of inclined angle and linkage length with fixed horizontal linkage length

After determining the optimum dimension for all parameters, the optimum angle is proven again by keeping the horizontal linkage length as constant. The suitable corresponding cavity height is investigated at the same time since a lower height is always preferred in the application. Hence, all the parameter is fixed with the optimised dimension, except

for the inclined angle and its corresponding cavity height and linkage length. The inclined angle is adjusted from 3° to 55°. To maintain a suitable base length for the vehicle excitation, the horizontal linkage length is fixed at 46.5 mm and a total base length of 186 mm with 20 mm of extended base length. The results are shown in Table 4.8 and Figure 4.14.

Table 4.8 FEA results with adjustment on the inclined angle and the cavity height of the Hull structure with fixed horizontal linkage length

| Angle (°) | Corresponding cavity height (mm) | Corresponding linkage length (mm) | Power output (mW) | PZT maximum stress (MPa) |
|---|---|---|---|---|
| 3 | 2.44 | 46.62 | 6.33 | 63.82 |
| 5 | 4.07 | 46.70 | 10.54 | 68.76 |
| **6** | **4.89** | **46.78** | **11.34** | 64.20 |
| 7 | 5.71 | 46.85 | 11.15 | 62.81 |
| 10 | 8.21 | 47.28 | 8.64 | 56.99 |
| 20 | 16.94 | 49.53 | 4.37 | 54.22 |
| 25 | 21.70 | 51.35 | 2.82 | 50.39 |
| 35 | 32.58 | 56.80 | 1.10 | 44.22 |
| 55 | 66.46 | 81.13 | 0.24 | 40.43 |

*'bolded' value indicates the optimum dimension*
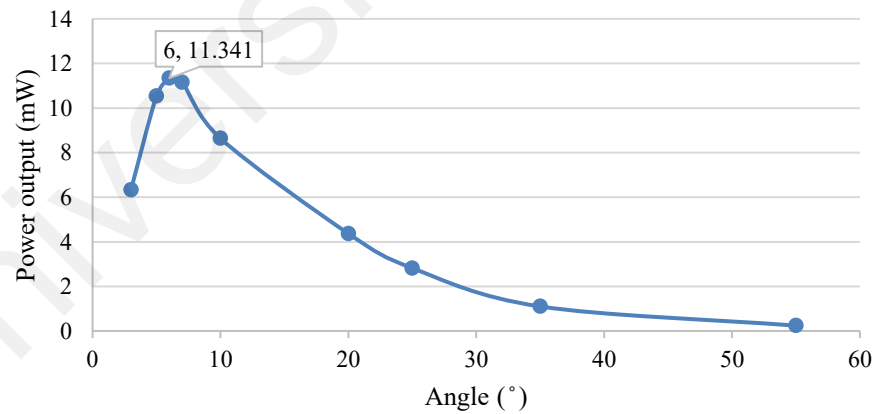


Figure 4.14 Power output of the PEH as a function of inclined angle of a Hull structure with fixed horizontal linkage length

Figure 4.14 shows that there is an optimum inclined angle at 6°. Normally, the force amplification effect will increase when the inclined angle is getting smaller. However, the inclined linkages will be shortened by the large amplified forces at an extremely small internal angle (Kuang et al., 2017). Consequently, less compressive deformation is

formed in the frame and the PZT, causing a reduction in the power output as mentioned in Section 2.3.4. This reduction in linkage length effect is getting stronger especially when the cavity height and the horizontal linkage length are extremely small. The same effect is noticed in the analytical model presented in Section 4.1.2. Eventually, 6° of inclined angle with a moderate cavity height of 4.89 mm is selected as the optimum dimension. This cavity height agrees well with the result mentioned in Section 4.2.1.2 where a frame will work safely with less than 6 mm of cavity height.

### 4.2.1.7 Effect of inclined angle and linkage length with fixed linkage length

The optimization is then carried out with the last manipulating variable, that is by keeping the linkage length as constant at 46.78 mm. The inclined angle is adjusted from 3° to 55°. The results are shown in Table 4.9 and Figure 4.15. Once again, an optimum inclined angle at 6° is proven with the highest power output of 11.34 mW.

Table 4.9 FEA results with adjustment on the inclined angle and the cavity height of the Hull structure with fixed linkage length

| Angle (°) | Corresponding cavity height (mm) | Corresponding horizontal linkage length (mm) | Power output (mW) | PZT maximum stress (MPa) |
|---|---|---|---|---|
| 3 | 2.45 | 46.72 | 4.34 | 84.23 |
| 4 | 3.26 | 46.67 | 7.87 | 81.60 |
| 5 | 4.08 | 46.70 | 10.71 | 65.86 |
| **6** | **4.89** | **46.52** | **11.34** | 64.20 |
| 7 | 5.70 | 46.43 | 11.15 | 58.40 |
| 10 | 8.12 | 47.07 | 8.47 | 56.03 |
| 20 | 16.00 | 43.96 | 2.89 | 55.39 |
| 25 | 19.77 | 42.40 | 1.84 | 49.59 |
| 35 | 26.83 | 38.71 | 0.82 | 37.10 |
| 55 | 38.32 | 26.83 | 0.14 | 22.11 |

*'bolded' value indicates the optimum dimension*
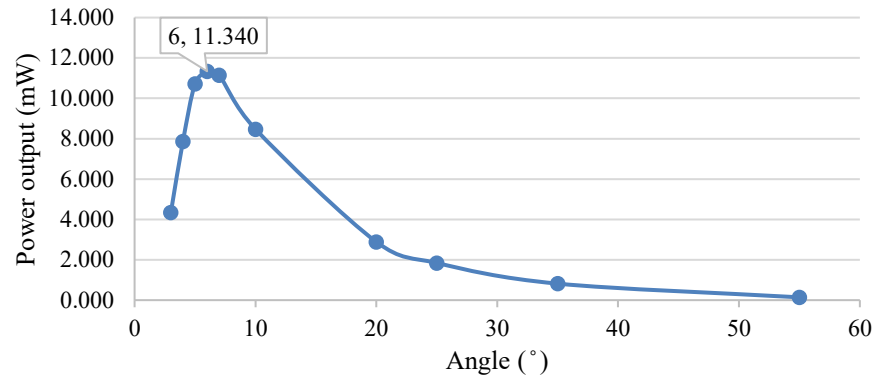
Figure 4.15 Power output of the PEH as a function of inclined angle of a Hull structure with fixed linkage length

Figure 4.16 presents the calculated amplification factor of the Hull structure through equation [4.11] at various inclined angles with fixed linkage length. It shows a force amplification factor of 9.72 at 6˚. The analytical model does not show the reduction in amplification factor when the inclined angle is less than 6˚, but a continuous increment as the angle decreases. This is because the analytical model does not consider the linkage shorten effect due to high amplified input force. However, at least 9.72 of the force amplification factor has been proven in the Hull structure theoretically. The analytical model shows agreement to the effects of other parameters, such as increasing linkage length, decreasing thickness, and decreasing Young's Modulus (decreasing stiffness) with increasing force amplification factor. In other words, the model could reveal these dimensional dependencies for this design only. Hence, to study other parametric effects that cannot be predicted by this analytical model or to further optimize the Hull structure, the CPC-FEM should be used.
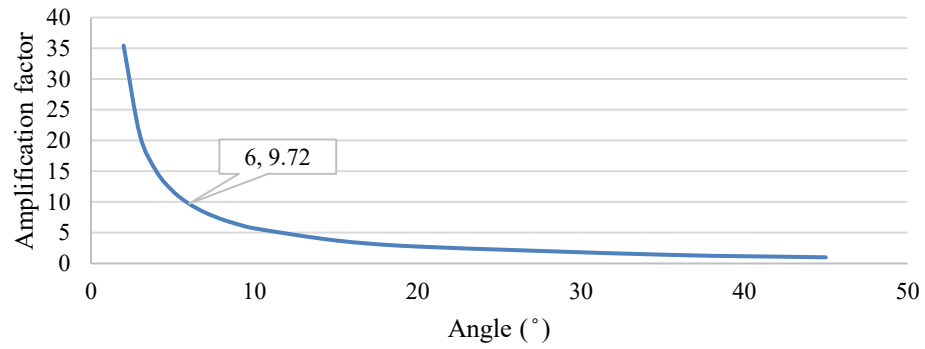
Figure 4.16 Theoretical amplification factor of the Hull PEH at various inclined angles

### 4.2.2    Overall Performance of an Optimized Hull PEH

Table 4.10 shows the final optimized value for each parameter of the Hull structure. An optimized Hull PEH with a total height of 17.8 mm has been developed which is suitable for the roadway application as it reduces the bury depth and eases the installation process.
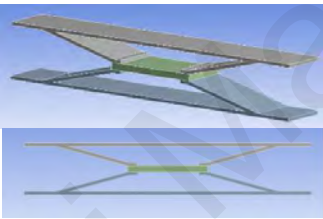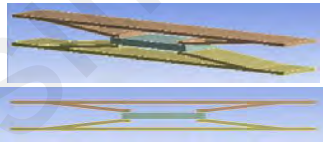
Table 4.10 Final value for each parameter of a Hull structure

| Parameters | Symbol | Final value |
|---|---|---|
| PZT length (mm) | $l_{PZT}$ | 52 |
| PZT thickness (mm) | $t_{PZT}$ | 4 |
| Width (mm) | $w$ | 30 |
| Base length (mm) | $l_s$ | 186 |
| Base thickness (mm) | $t_s$ | 2 |
| Linkage thickness (mm) | $t_b$ | 2 |
| Cavity height (mm) | $h$ | 4.89 |
| Linkage length (mm) | $l_b$ | 46.8 |
| Horizontal linkage length (mm) | $l_h$ | 46.5 |
| Extended base length (mm) | $l_e$ | 20 |
| Joint length (mm) | $l_j$ | 7 |
| Inclined angle (˚) | $\theta$ | 6 |

The average PZT nodal stress has been increased from 23.8 MPa to 32.3 MPa, which is a sign of a higher amplification effect and more PZT deformation has been achieved through parametric optimization. The optimized PEH has maximum frame stress of 315.12 MPa and a maximum PZT stress of 64.2 MPa, which are both within the material stress limit with safety factor of 2.

An improved power output of 11.34 mW is generated which is 1.78 times (178%) larger than the unoptimized Hull structure of 6.37 mW. Thus, with the enhanced amplification effect and sufficient power output, a sustainable energy source for low-powered wireless electronic devices can be realized under such forcing conditions. The comparison of the optimized and unoptimized Hull structures is summarized in Table 4.11.

Table 4.11 Comparison of the optimized Hull structure with the unoptimized case
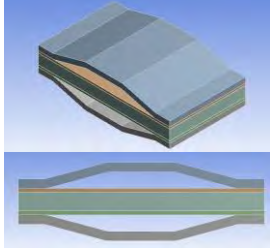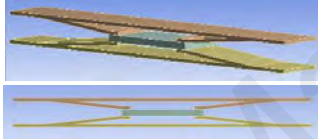
| Design description | Illustration | Max. PZT stress (MPa) | Avg. PZT nodal stress (MPa) | Max. frame stress (MPa) | Power output (mW) |
|---|---|---|---|---|---|
| (a) Unoptimized Compressive Hull structure:<br>• 15˚ inclined angle<br>• 10.47 mm cavity height<br>• Total height of 28.9 mm<br>• Total base length of 186.14 mm<br>• 6 mm joint length |  | 51.6 | 23.8 | 399.41 | 6.37 |
| (b) Optimized Compressive Hull structure:<br>• 6˚ inclined angle<br>• 4.89 mm cavity height<br>• Total height of 17.8 mm<br>• Total base length of 185 mm<br>• 7 mm joint length |  | 64.2 | 32.3 | 315.51 | 11.34 |

### 4.2.3 Comparison of the Optimized Hull Structure and a Benchmark Rectangular Cymbal Structure

The optimized Hull PEH is then compared with a benchmark optimized Rectangular Cymbal PEH of the same PZT's size under the same forcing environment. The comparison is first made based on their structural design and characteristic as listed in Table 4.12. This also includes the important key point that has been discussed in Section 4.1, which typically describes the advantages of the Hull structure over the conventional amplifier structure. Then, their functionality and performance will be compared and further discussed in terms of load capacity, energy harvesting performance, cost-

effectiveness, and energy transmission efficiency. The comparison of the FEA result is summarized in Table 4.13.

Table 4.12 Structural design comparison on the optimized Hull structure and the benchmark Rectangular Cymbal structure

| Design description | Illustration | Attributes |
|---|---|---|
| **(a) Optimized Benchmark Tensile Rectangular Cymbal structure:**<br>• With dual-layer 0.7 mm substrates<br>• 15˚ inclined angle<br>• 3.8 mm cavity height<br>• 14 mm apex length<br>• 6 mm joint length<br>• Total height of 17.2 mm |  | ✗ PZT works in tension with lower tensile yield strength.<br>✗ Additional substrate is necessary to prevent high stress concentration.<br>✗ Restricted cavity height and linkage length design.<br>✗ Small forcing area ($14 \times 30$ mm$^2$).<br>✗ Additional plate or casing is needed for excitation force with larger loading area. |
| **(b) Optimized Compressive Hull structure:**<br>• Extended 20 mm base at both ends<br>• 6˚ inclined angle<br>• 4.89 mm cavity height<br>• 185 mm base length<br>• 7 mm joint length<br>• Total height of 17.8 mm |  | ✓ PZT works under compression with higher compressive yield strength.<br>✓ Additional substrate is not necessary.<br>✓ Flexible cavity height and linkage length design.<br>✓ Large forcing area ($185 \times 30$ mm$^2$).<br>✓ No additional plate or casing is needed. |

Since the compressive yield strength of PZT is much higher than its tensile yield strength, the PZT plate with a compressive Hull frame can be further compressed to achieve greater power output. An additional substrate is not necessary for the developed Hull structure as the PZT stress level is far from its compressive stress limit. On the other hand, a larger forcing area is provided by the Hull structure as the size of the Hull end cap is not restricted by the size of PZT as the Rectangular Cymbal structure does. It is beneficial especially in the foot strike underground or vehicular roadway PEH application. This is because more energy can be transferred through the Hull structure to the PZT directly with minimum loss. It is another advantage over the Flexcompressive structure which requires an additional forcing platform to work underground.

Table 4.13 FEA result comparison on the optimized Hull structure and the benchmark Rectangular Cymbal structure

| Design criteria & the corresponding variables | Type of PEH | Optimized Tensile Rectangular Cymbal PEH | Optimized Compressive Hull PEH |
|---|---|---|---|
| **Loading capacity** | Maximum PZT stress (MPa) | 17.47 | 64.20 |
| | Maximum frame stress (MPa) | 124.41 | 315.51 |
| **Level of PZT's utilization** | Average PZT nodal stress (MPa) | 8.74 | 32.30 |
| **Energy harvesting performance** | Power output (mW) | 3.68 | 11.34 |
| | Volume power density (kW/m$^3$) | 0.59 | 1.82 |
| **Strain energy transmission efficiency** | Average PZT elemental strain energy ($\mu$J) | 1.60 | 88.10 |
| | Overall average elemental strain energy ($\mu$J) | 3.48 | 143.00 |
| | Total PZT elemental strain energy (J) | 0.003 | 0.042 |
| | Overall total elemental strain energy (J) | 0.022 | 0.287 |
| | Energy transmission efficiency (%) | 15.18 | 14.74 |

From the FEA result, it can be observed that both the PZT and the amplification frame of the Hull PEH are having higher maximum stress but within the stress limit. However, the PZT in Rectangular Cymbal PEH has reached its stress limit of 17.5 MPa due to its lower tensile yield strength. Thus, it will fail to work under a larger forcing environment. The compressive Hull PEH has a higher loading capacity which is ideal for a large force environment. The overall Von-Mises stress distribution of both structures is illustrated in Figure 4.17.
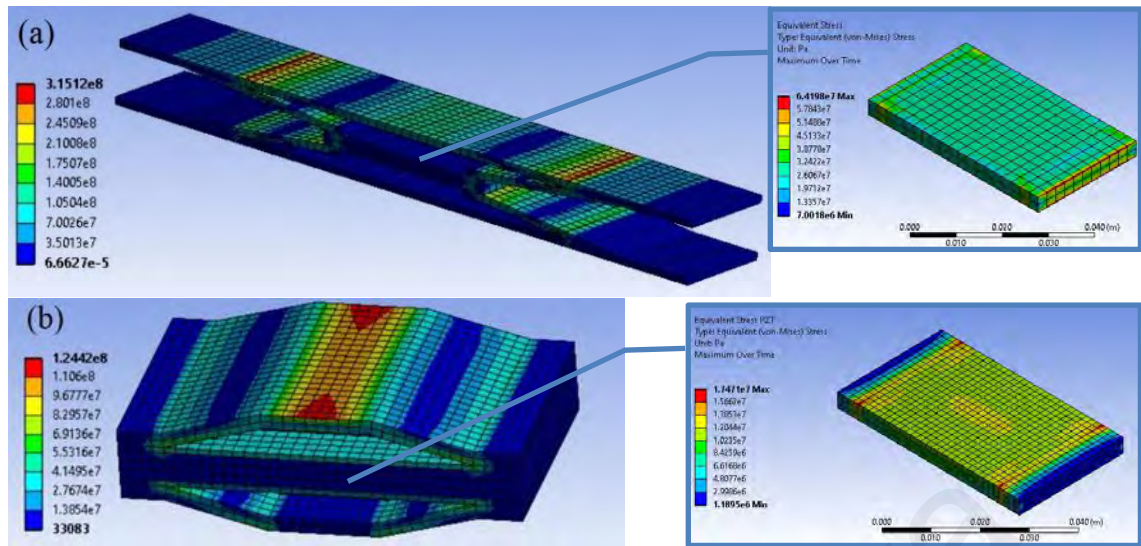
Figure 4.17 Stress distribution of (a) the developed compressive Hull PEH and (b) the benchmarking tensile-typed Rectangular Cymbal PEH under same boundary conditions

From another aspect, the optimized Hull PEH has 32.3 MPa of PZT's average nodal stress, which is much higher than the Rectangular Cymbal PEH with only 8.74 MPa under the same force. This is because the optimized Hull structure has amplified the input force in a larger scale and transmitted to the PZT, leading to larger stress and deformation created in the PZT material. The optimized Hull PEH is concluded to have a higher level of utilization on the PZT material. It is demonstrated by its higher power output of 11.34 mW as the amount of harvested energy is proportional to the PZT's stress level. Hence, the optimized Hull PEH has a better energy harvesting performance, which is 3.08 times (308%) larger than the Rectangular Cymbal structure. The developed Hull PEH has volume power density and volume-force power density of 1.817 kW/m$^3$ and 1.817 W/Nm$^3$, respectively. From Table 2.2, this power output is comparatively higher among the single-stage amplifier structure PEH with only a single PZT plate at low frequency. A summary on the comparison of existing PEHs with similar forcing function in term of force magnitude and frequency are extracted and listed in Table 4.14. Thus, with the enhanced amplification effect and sufficient power output, a sustainable energy source for low-powered wireless electronic devices can be realized under such forcing conditions.

Table 4.14 Comparison of energy harvesting performance between the proposed Hull PEH and the existing PEHs with similar forcing function

| Amplifier structure | Piezo material | Piezo size (mm³) | Excitation amplitude (kN or *g*) | Frequency (Hz) | Load (Ω) | Average power output (mW) | Volume power density (kW/m³) | Reference |
|---|---|---|---|---|---|---|---|---|
| Rectangular cantilever | d15 PZT-51 | (13.0×2.5×1.0) ×2 | 1.48 *g* | 73.0 | 2.2 M | 0.009 | 0.13* | (J. Zhao et al., 2012) |
| Multibranch cantilever | MFC (2814-P2) | 28.0×14.0×0.3 | 0.02 *g* | 25.0 | 255.0 k | 0.032 | 0.27* | (Xiangyang Li et al., 2019) |
| Unimorph Cymbal | PZT-5H | Ø ≈ 25.0, *t* ≈ 0.2 | 1.94 kN | 1.0 | 3.3 M | 0.121 | 1.29* | (Mo et al., 2013) |
| Compressive mode Rhombus | d33 PZT stack | 1 stack: 130 layers = 16.0×5.0×5.0 | 0.22 kN | 2.8 | 19.2 k | 0.400 | 1.00* | (Feenstra et al., 2008) |
| Flexcompressive | SONOX SP505 stack | 1 stack: 300 layers = 32.3×7.0×7.0 | 0.10 kN | 1.4 | 50.0 k | 0.650 | 0.41* | (W. S. Chen et al., 2017) |
| Improved Flexcompressive | SONOX SP505 stack | (1 stack: 300 layers = 32.3×7.0×7.0) ×2 | 0.10 kN | 1.4 | 30.0 k | 4.500 | 1.42* | (W. S. Chen et al., 2017) |
| Tensile Cymbal (Benchmark structure) | DL-53HD PZT | 52.0×30.0×4.0 | 1.00 kN | 2.0 | 5.9 M | 3.680 | 0.59 | Current work |
| Compressive Hull (New structure) | DL-53HD PZT | 52.0×30.0×4.0 | 1.00 kN | 2.0 | 5.9 M | 11.340 | 1.82 | Current work |

From cost-effectiveness perspective, three Rectangular Cymbal PEHs are required to achieve the same power output as a Hull PEH under the same forcing environment. In other words, almost the same volume of frame material is involved in the fabrication but two more PZT plates are needed in the Rectangular Cymbal PEHs to accomplish the same effect as the Hull PEH. Hence, the Hull structure is said to be cost-effective.

The next design criterion is the energy transmission efficiency, which is defined as the ratio of strain energy in the piezoelectric materials and the total strain energy in the piezoelectric and amplification frame. The energy transmission efficiency is derived by summing the elemental strain energy rather than directly using the maximum strain energy value as shown in Figure 4.18. Table 4.13 shows that the Hull PEH has lower efficiency than the Rectangular Cymbal structure (i.e., 14.74% vs 15.18%) even though the Hull PEH has greater average and total elemental strain energy. However, the

efficiency is still within the reasonable range of 1 – 23% as the existing PEHs have (L. Wang et al., 2016).

Lower efficiency is due to most of the energy being stored in the amplifier structure as potential energy, instead of transmitting to the PZT plate. This remaining stored energy could protect the structure from damage which increases the loading capacity and safety factor of the PEH. A similar case can be found in the two-stage Flexcompressive PEH which has a lower efficiency but higher power output than the single stage Flexcompressive structure. Hence, higher energy transmission efficiency could not guarantee a higher power output. 74.9 mW/g$^2$

In short, energy transmission efficiency in terms of strain energy is not a comprehensive evaluating factor in assessing the PEH's energy harvesting performance. Energy conversion efficiency in terms of input force energy and output power energy would be comparatively more reliable to check on the harvesting performance of the PEH. Also, this efficiency is obtained experimentally as presented in Section 4.4.2.
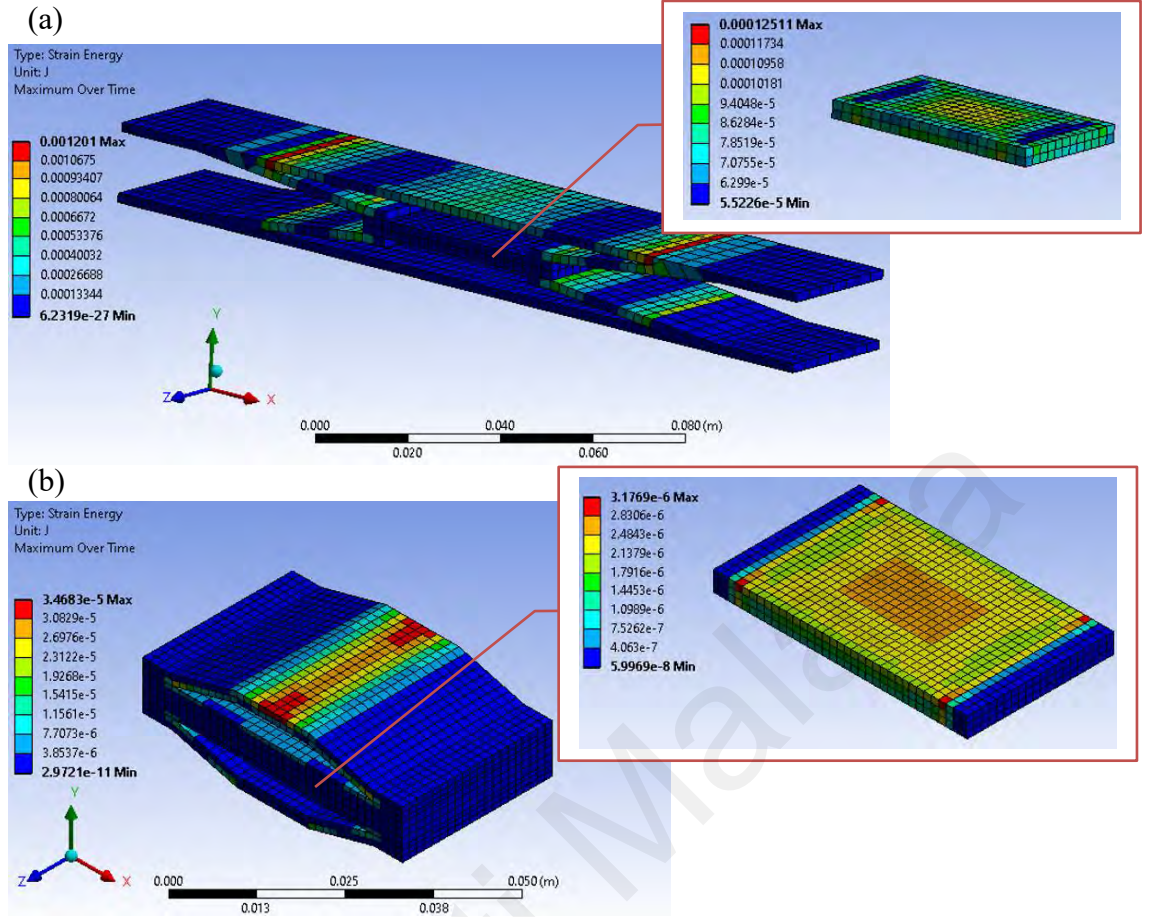
Figure 4.18 Maximum strain energy of (a) the optimized Hull PEH and (b) the optimized benchmark Rectangular Cymbal PEH

### 4.2.3.1 Comparison under impact force

Next, an impact force is applied and the performance of the proposed PEH is studied since it could represent the actual forcing environment better than the sinusoidal force in this study. This is because the impact force has a much similar forcing profile with the targeted environment to demonstrate a foot strike or wheel rolling (W. S. Chen et al., 2017; Y. Wang et al., 2016). Therefore, the Hull PEH is tested with impact force in the subsequent experiments.

The parametric optimization result is valid for both impact and harmonic force. This is because the structural optimization of the Hull design is not affected by the excitation frequency but mainly relies on the magnitude of force, especially the thickness. Moreover, the modal analysis shows that the Hull PEH has a high natural frequency of over 300 Hz.

Figure 4.19 shows its first mode happens at 356.10 Hz, followed by 633.09, 772.75, 797.36, 1293.80, and lastly 1569.60 Hz. In fact, the proposed Hull PEH is aiming at high force low frequency environment, such as human foot strike, vehicular excitation from roadway pavement, or load weighing on the conveyor belt of the production line, etc. In other words, the proposed PEH will be operated at a low and safe frequency range, which is less than 10 Hz (Avvari, Yang, & Soh, 2016). Hence, the optimization result would remain the same for both forcing functions. In addition, the fatigue issue is negligible as the non-resonator Hull PEH operates at a frequency that is much smaller and far away from its natural frequency (Buscarello, 1987). Since a safety factor of 2 is maintained throughout the FEA, low stress that is below half of the material's fatigue limit can ensure the longevity and durability of the developed Hull PEH (Kuang, Chew, Dunville, Sibson, & Zhu, 2021).
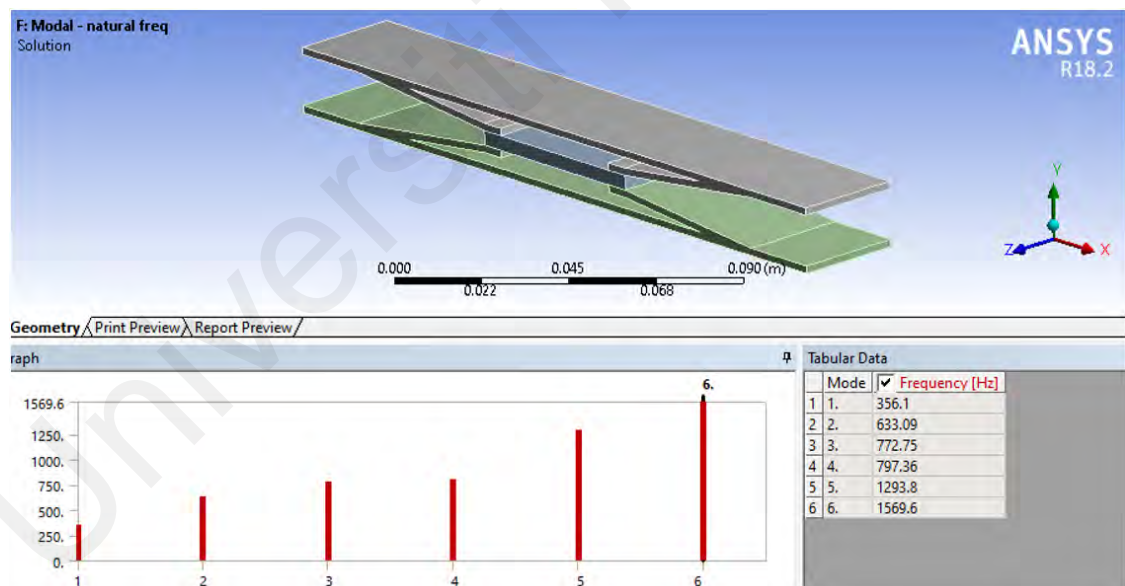


Figure 4.19 Natural frequencies of the Hull PEH from modal analysis

Figure 4.20 presents that both PEHs have similar stress distribution under the impact force if compared with the harmonic force of same 1 kN magnitude. The Hull PEH shows that the open-circuit peak voltage increases linearly with increasing impact force in Figure 4.21. The reason is that the stress and deformation levels in the PZT plate have been

increased as the force rises. The Hull structure has played its role in amplifying the input force, causing the output force acting on the PZT plate to increase constantly. According to the FEA, a high open-circuit peak voltage (i.e., 1031.12 V) has been achieved under 1kN of impact force. It shows that the Hull PEH has an excellent energy harvesting performance and force amplification effect under this range of force.
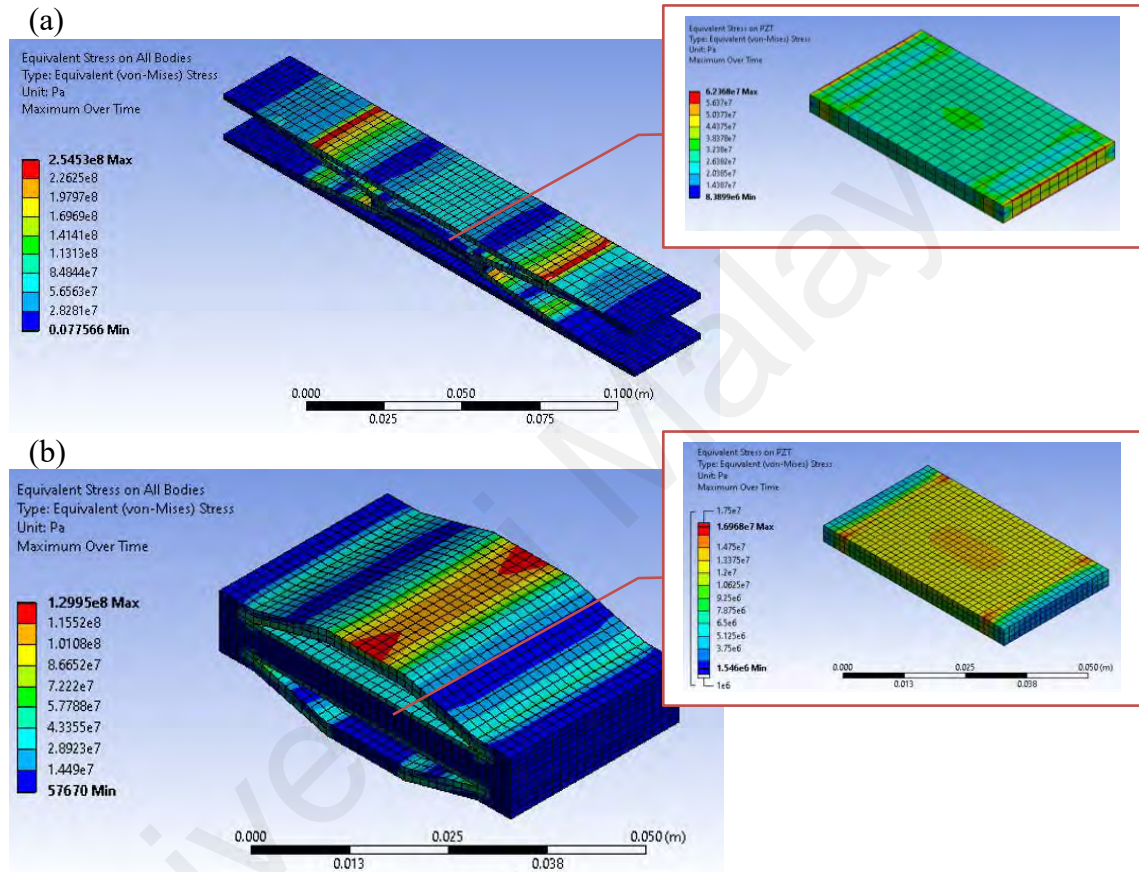


Figure 4.20 Stress distribution of (a) the Hull PEH and (b) the benchmark Rectangular Cymbal PEH under 1 kN impact force
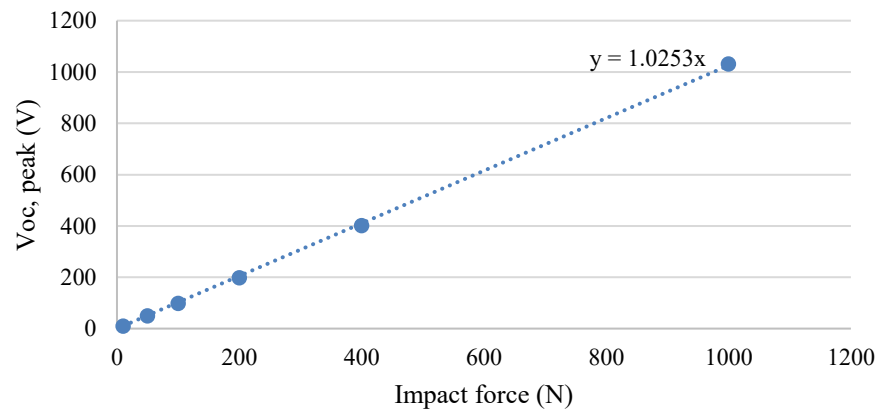


Figure 4.21 FEA voltage output of the Hull PEH under various impact forces

## 4.3 Fabrication of Hull and Benchmark PEH Prototypes

Figure 4.22 shows the fabricated optimised Hull structure. A Sodick A500W CNC wire electrical discharge machine is used to fabricate the end caps with high accuracy which is up to four decimal places in unit mm. The Rectangular Cymbal structure is fabricated with a stainless steel block using the same wire cutting method as shown in Figure 4.23. It is used as a benchmark case in the experiment.

The substrate is bonded to the Rectangular Cymbal end cap using a Rofin Starfire 300 laser welding machine with a laser power of 260 W and a laser speed of 2 mm/s. Two $52 \times 30 \times 4 \text{ mm}^3$ DL-53HD soft PZT plates are then bonded with the fabricated frames using double-sided conductive copper tape. 3M Scotch-Weld™ DP-460 structural adhesive is used to replace it at a later stage to ensure a strong bonding effect. Lastly, two wires are connected directly at the top and bottom surfaces of the PZT plate by using copper tape. Again, the copper tape can be replaced by using soldering to make a permanent wire connection. The fabrication of PEH prototypes is completed and ready for experimental testing.
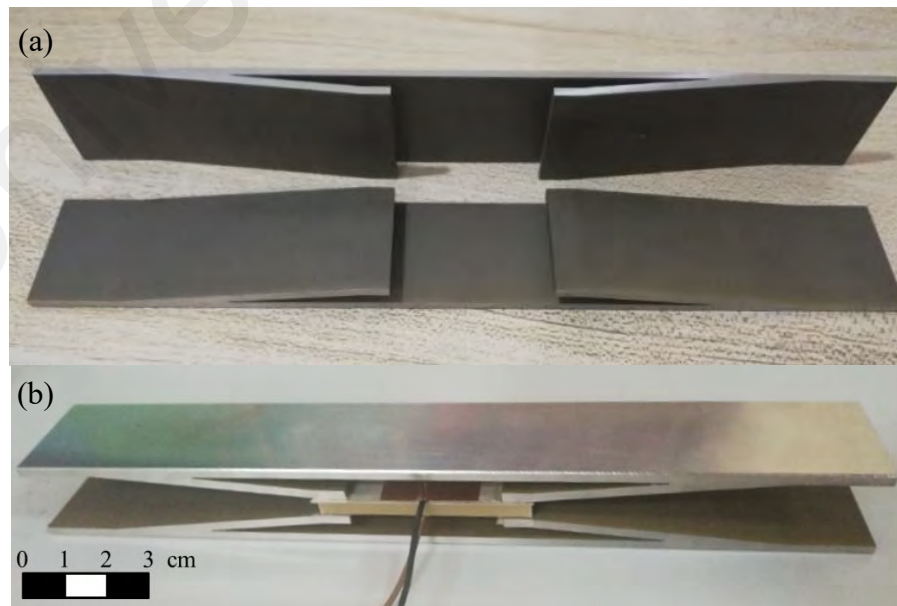


Figure 4.22 Fabricated (a) Hull structure end caps and (b) the overview of the Hull PEH
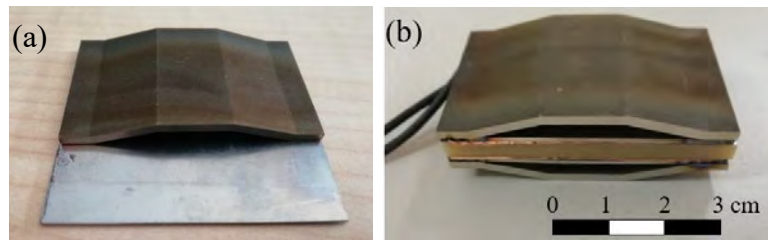
Figure 4.23 Fabricated (a) Rectangular Cymbal end cap and substrate;
(b) Rectangular Cymbal PEH

The fabricated prototype will be examined through several loading tests as mentioned in Section 3.5 to investigate the performance of the proposed PEH with optimized structure.

## 4.4 Experimental Validation of Prototypes under Different Loading Conditions

### 4.4.1 Impact Test to Examine the Energy Harvesting Performance of Hull PEH

In order to validate the FEA result, the impact force experiment is carried out on the fabricated Hull PEH, which can represent the actual forcing environment better than the sinusoidal force in this study. This is because the impact force has a much similar forcing profile with the targeted environment to demonstrate a footstrike or wheel rolling (W. S. Chen et al., 2017). Therefore, the Hull PEH was tested with impact force in the subsequent experiments while harmonic force was used to test for the charging performance as reported in Section 4.4.2.

The experimental open-circuit peak voltage result is plotted in Figure 4.24 with the best fit regression line. The influence of the amount of applied load force on the output voltage produced by the developed PEH has been examined. Figure 4.24 shows a positive correlation between the input impact force (ranging from 10 N – 1k N) and the output voltage. This result agrees well with the mechanism of PEH since more deformation and stress accumulate at the PZT when higher force is applied, leading to a higher output voltage.

The FEA and experimental open-circuit peak voltage results under 10 N, 50 N, 100 N, 200 N, 400 N, and 1 kN of impact forces are tabulated in Table 4.15. The experimental voltage for each force is interpolated based on the equation of the best fit line since it is difficult to achieve the exact amount of impact force from the hammer strike. The experimental result agrees well with the FEA simulation. This proves that the developed CPC-FEM has high accuracy and reliability to demonstrate the real condition with less than 5.2% of deviation.
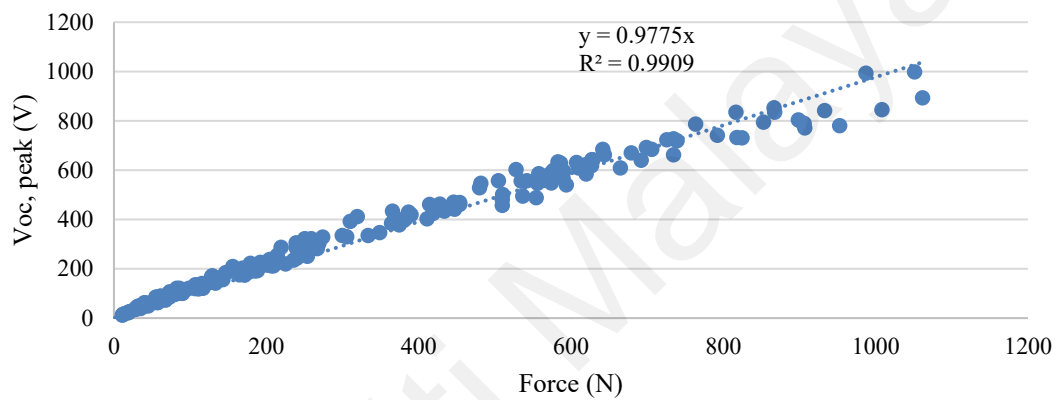


Figure 4.24 Experimental open-circuit peak voltage of the Hull PEH under various impact forces

Table 4.15 Experimental validation of open-circuit peak voltage of the Hull PEH under impact force

| Force (N) | 10 | 50 | 100 | 200 | 400 | 1,000 |
|---|---|---|---|---|---|---|
| FEA simulation $V_{oc, peak}$ (V) | 9.64 | 48.80 | 98.14 | 197.81 | 400.76 | 1,031.12 |
| Experimental $V_{oc, peak}$ (V) | 9.78 | 48.88 | 97.75 | 195.50 | 391.00 | 977.50 |
| Percentage error (%) | 1.40 | 0.15 | 0.39 | 1.17 | 2.44 | 5.20 |

On the other hand, the energy harvesting performances based on the output voltage of the Hull PEH, Rectangular Cymbal PEH, and standalone PZT plate are compared in Figure 4.25. It can be clearly observed that the Hull PEH has a higher gradient of graph (i.e., 0.9775) than the Rectangular Cymbal PEH of 0.1436. The Hull PEH exhibits at least 5 times (6.8 times based on the gradient of the graph) larger voltage output than the benchmark case. It also shows a great harvesting performance, which is at least 14 times greater than the standalone PZT. If referring the gradient of 0.0578, the Hull structure has

amplified the voltage output up to 16.9 times larger. Based on this direct comparison of the open-circuit peak voltage, the energy harvesting performance of the Hull PEH is very impressive and comparatively much powerful. The Hull amplifier structure is proven to have a great effect in magnifying the input force and compress the PZT in a larger scale.
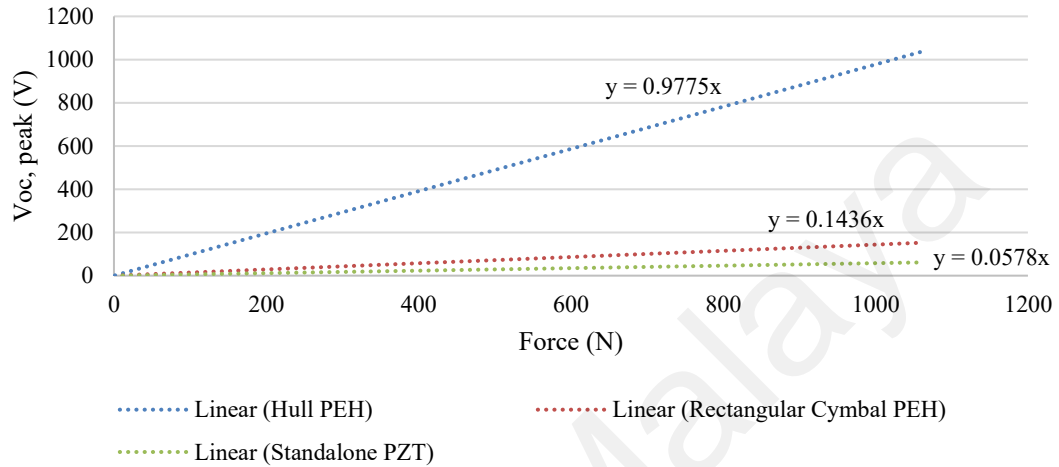


Figure 4.25 Experimental comparison of voltage output from the Hull PEH, the Rectangular Cymbal PEH and the standalone PZT plate under impact force

From this experimental output voltage result, the Hull structure shows an amplification ratio of 16.9 if compared to the standalone PZT plate. The theoretical result calculated through equation [4.11] is 9.72 at 6˚. The deviation of the result is caused by the different scale of amplification ratio in voltage, power output and force amplification effect as faced by other researches (Y. Wang et al., 2016). Hence, the developed structure is said to have a high amplification ratio if compared with the existing single stage amplifier structure in PEH as shown in Table 2.3.

Next, impedance matching has been done by varying the resistance across the Hull PEH from 10 kΩ - 1 MΩ to obtain the maximum power output. The maximum power output is gained at the optimum external resistance, which has been matched with the internal impedance and the source impedance. It is found that the optimum load resistance for Hull PEH remains the same throughout the range of impact force, which is at 50 kΩ. It is not affected by the amount of force applied at the Hull PEH. In other words, the Hull

PEH always produces the highest power output when it is connected across 50 kΩ of external load resistance under the impact force as shown in Figure 4.26. On the other hand, Figure 4.27 shows the peak voltage and maximum power output across different resistances under 500 N and 1 kN impact force respectively. Both graphs clearly show that 50 kΩ is the optimum resistance with the highest maximum power outputs, which are 1.77 W under 500 N and 7.16 W under 1 kN of impact force.

Besides, these maximum power outputs are higher than those of the Rectangular Cymbal structure, which are 0.04 W under 500 N and 0.19 W under 1 kN. The benchmark structure has the same optimum resistance at 50 kΩ as well under the impact force. The Hull PEH once again shows a better energy harvesting performance than the benchmark structure in the experiment. It produces 37.68 times greater power output under 1 kN of impact force, although the ratio of power output between Hull PEH and benchmark PEH is different from that of the harmonic force. The difference is caused by different optimum resistance used under harmonic and impact forces as the frequency varies.
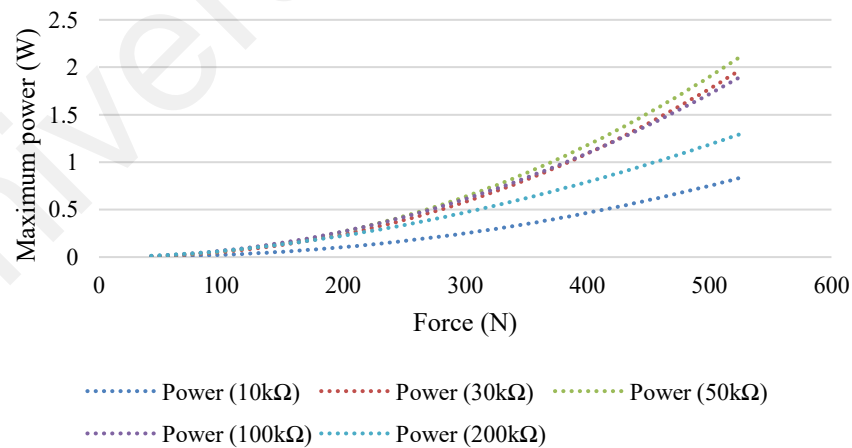


Figure 4.26 Maximum power output of Hull PEH across several load resistances under various impact forces
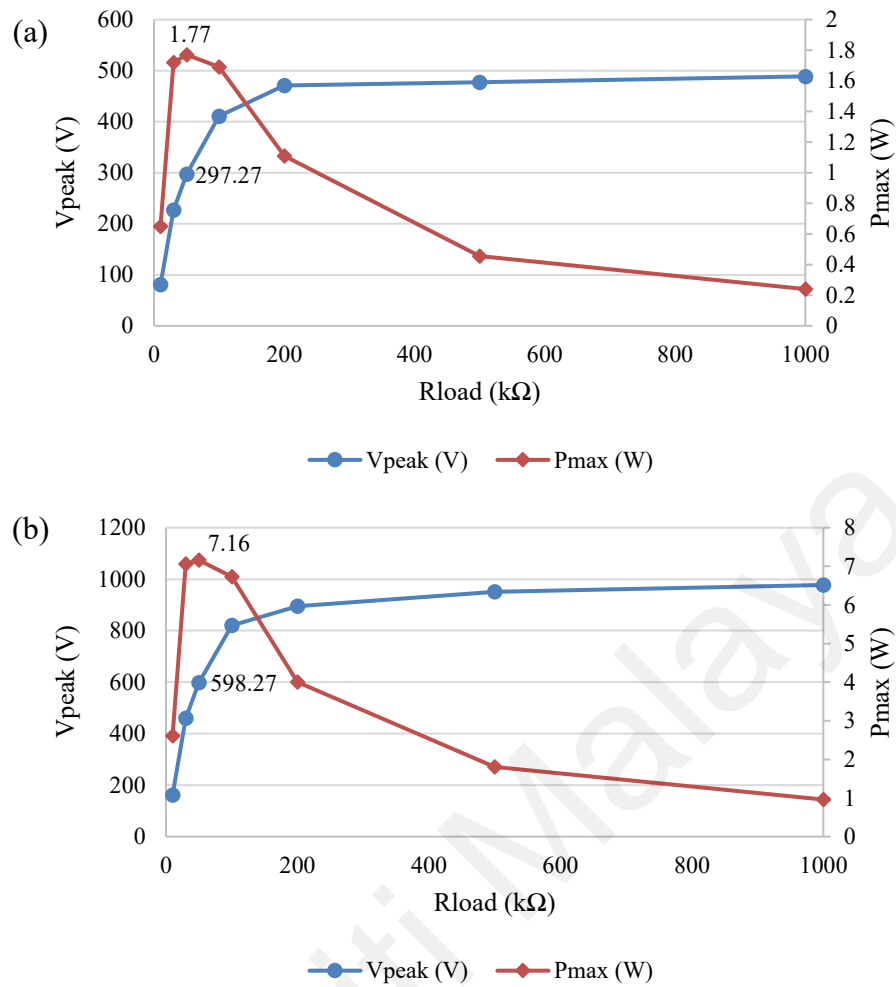
Figure 4.27 Impedance matching for Hull PEH under (a) 500 N and (b) 1 kN impact forces

After verifying the optimum resistance experimentally, a reverse FEA simulation is conducted to validate the power output and stress distribution. It shows a slight deviation of 3.5% in the peak voltage and 6.9% in the power output under 1 kN of impact force across 50 kΩ. The FEA is then done with a higher magnitude of force up to 2.5 kN to investigate the performance of the Hull PEH. The result is listed in Table 4.16. From the FEA result, the Hull PEH has a great advantage over the benchmark Rectangular Cymbal structure as its power output could keep increasing when the force increases up to 2.5 kN.

Table 4.16 FEA result of the Hull PEH across 50 kΩ under higher impact forces

| Force (kN) | 1.0 | 2.0 | 2.5 |
|---|---|---|---|
| $V_{peak}$ (V) | 619.96 | 1,163.94 | 1,624.14 |
| $P_{max}$ (W) | 7.69 | 27.10 | 52.76 |
| PZT max. stress (MPa) | 62.37 | 124.17 | 163.63 |
| EC max. stress (MPa) | 254.53 | 610.85 | 609.29 |
| PZT avg. nodal stress (MPa) | 33.10 | 56.20 | 88.30 |

In contrast, the structural design of the Rectangular Cymbal structure has to be adjusted so that it could work safely under higher force. However, even the thickness of the substrate and end cap has been increased to compensate for the increasing stress level, the Rectangular Cymbal PEH still meets its power output limitation. This is because the PZT material has reached the saturated state of its size under 2 kN impact force. For instance, the voltage and power output of the Rectangular Cymbal PEH stop increasing after 2 kN of impact force as shown in Figure 4.28. It saturates at around 11.5 MPa of average PZT nodal stress in the FEA. Therefore, the PZT is said to be fully utilized by reaching the saturated tensile stress limit of its size.
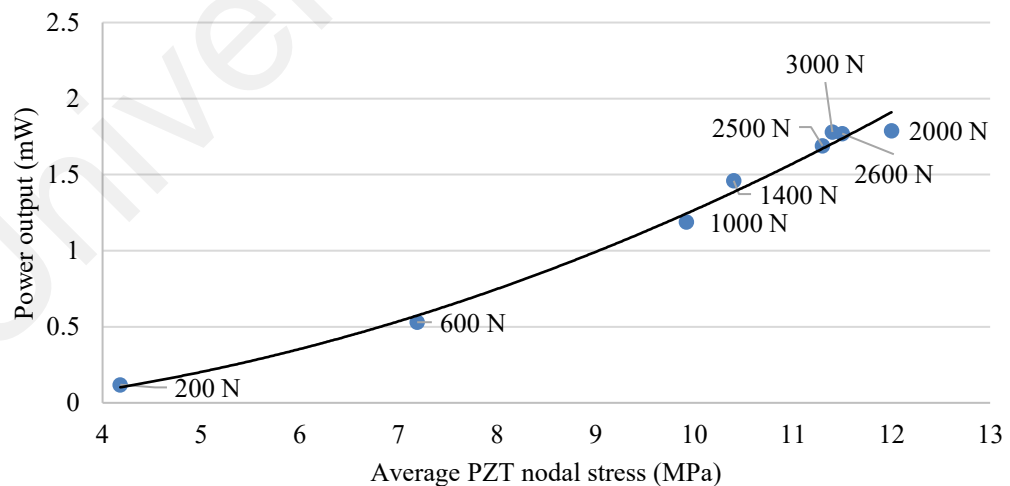


Figure 4.28 Power output and the average PZT nodal stress of the Rectangular Cymbal PEH under different loading forces

Therefore, the developed Hull structure is concluded to have a greater capability to work in a higher force environment since its PZT's stress limit is 10 times higher than that in the Rectangular Cymbal structure of 17.5 MPa. There is room for improvement on the stress level in the developed structure as the current design has an average PZT nodal stress of 33 MPa under 1 kN of impact force.

In addition, the energy conversion efficiency, $\eta$ of the Hull PEH is calculated via equations [2.9] – [2.11] with additional reference from (Shafer & Garcia, 2013) based on the average input and output energies. It has 84.38% of efficiency by retrieving the mechanical input response from the force sensor and accelerometer. Figure 4.29 and Figure 4.30 show the retrieved data and the calculation of the efficiency based on the input and output energy.



Figure 4.29 Raw data for Hull PEH's energy conversion efficiency calculation i.e., (a) force, (b) voltage, (c) acceleration, and (d) displacement under 1 kN impact force

Figure 4.30 (a) Force, (b) displacement, (c) input and (d) output energy curves per cycle extracted from the raw data, and (e) the efficiency calculation for Hull PEH under 1 kN impact force

## 4.4.2 Compression Loading Test Using Permanent Magnet Shaker V201 for Hull PEH

A permanent magnet shaker V201 is used to compare the performance of the proposed Hull PEH and the benchmark structure under harmonic force. However, due to the apparatus limitation, only a 10 N of sinusoidal force at 50 Hz is stably applied at both fabricated PEHs. The Hull PEH shows an open circuit AC peak voltage of 7.34 V which

is 5.28 times higher than the Rectangular Cymbal structure of 1.39 V as shown in Figure 4.31 (a) and (b). Again, this proves that the developed Hull PEH has a higher force amplification effect which causes the PZT to deform more and produce higher voltage than the benchmark structure under the same compression loading.

The Hull PEH is then undergone impedance matching with a range of resistance loads from 50 kΩ to 1 MΩ under this sinusoidal force. A full-bridge rectifier with four 1N5817 diodes across a 100 µF capacitor is used to convert the AC voltage output by the PEH to DC voltage. Figure 4.31 (c) presents the impedance matching result. The Hull PEH has the highest power output of 54 µW at 180 kΩ, which is slightly deviated in the same order from the calculated optimum resistance of 240 kΩ through equation [3.2].

To validate the experimental power output, an additional FEA testing at this force has been conducted and the estimated power output (i.e., 52 µW) is in the same order as the experimental value (54 µW) with a deviation of 3.8%. Therefore, the result of the FEA model is verified satisfactorily. The slightly deviation between the experimental and simulation results is due to the resistance effect of the external circuit and electronic devices. A similar FEA testing has been conducted for the benchmark Rectangular Cymbal PEH. It shows an output power of 24.2 µW under 10 N force, which is lower than that of the developed Hull PEH. Hence, the Hull PEH shows better harvesting performance in both simulation and experiment despite the loading environment either in high (1 kN) or low force (10 N).

The Hull PEH has a broadband energy harvesting efficiency, $\eta$ of 18.17% at a useful measured range of 5-700 Hz. It shows 3.24% of efficiency around 50 Hz after applying 45-55 Hz of band-pass filtering. Figure 4.32 - Figure 4.35 show the retrieved raw data and the calculation of these two efficiencies based on the input force, displacement, and output voltage. The efficiency under harmonic force is much lower than that of an impact

force. This is because there is probably energy lost from the input source, where the shaker does not transmit all the energy well to the Hull PEH. Energy may dissipate as heat energy due to a variety of effects such as structural damping, current leakage, and dielectric loss during the harmonic force excitation (Yang, Erturk, et al., 2017).
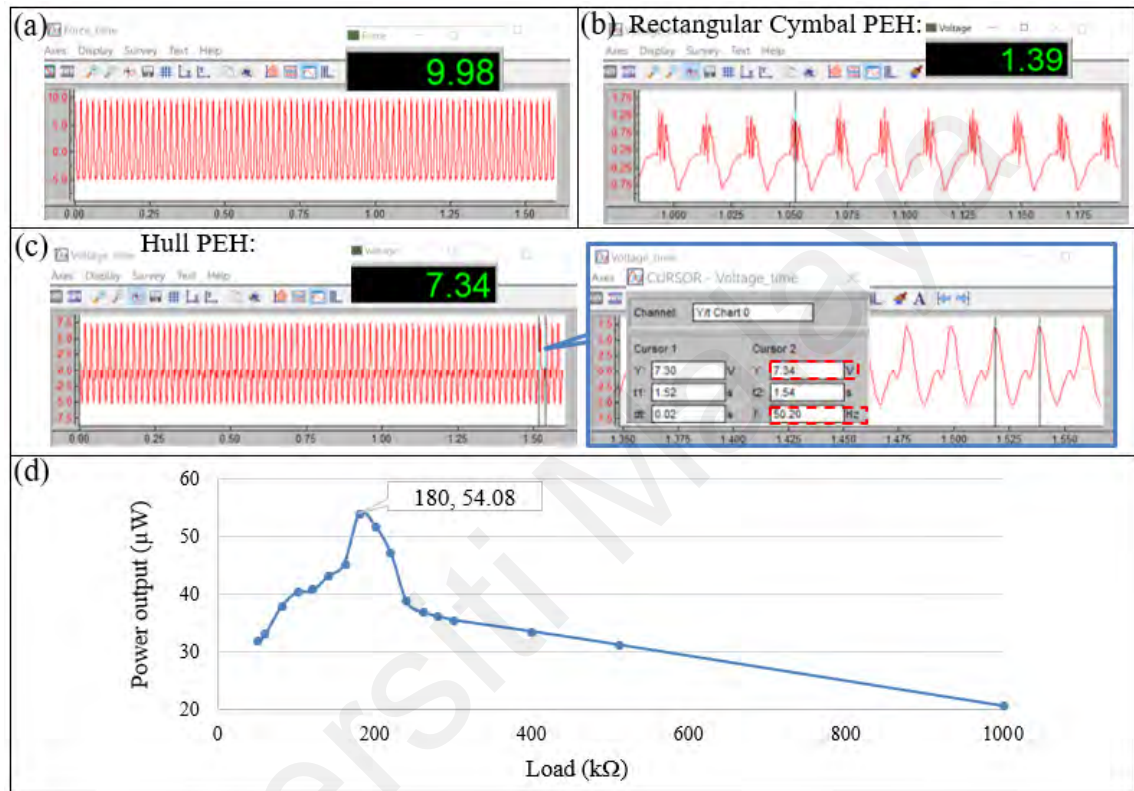


Figure 4.31 (a) Loading force measurement; Open circuit voltage output for
(b) Hull PEH and (c) Rectangular Cymbal PEH under 10 N of sinusoidal force at 50 Hz;
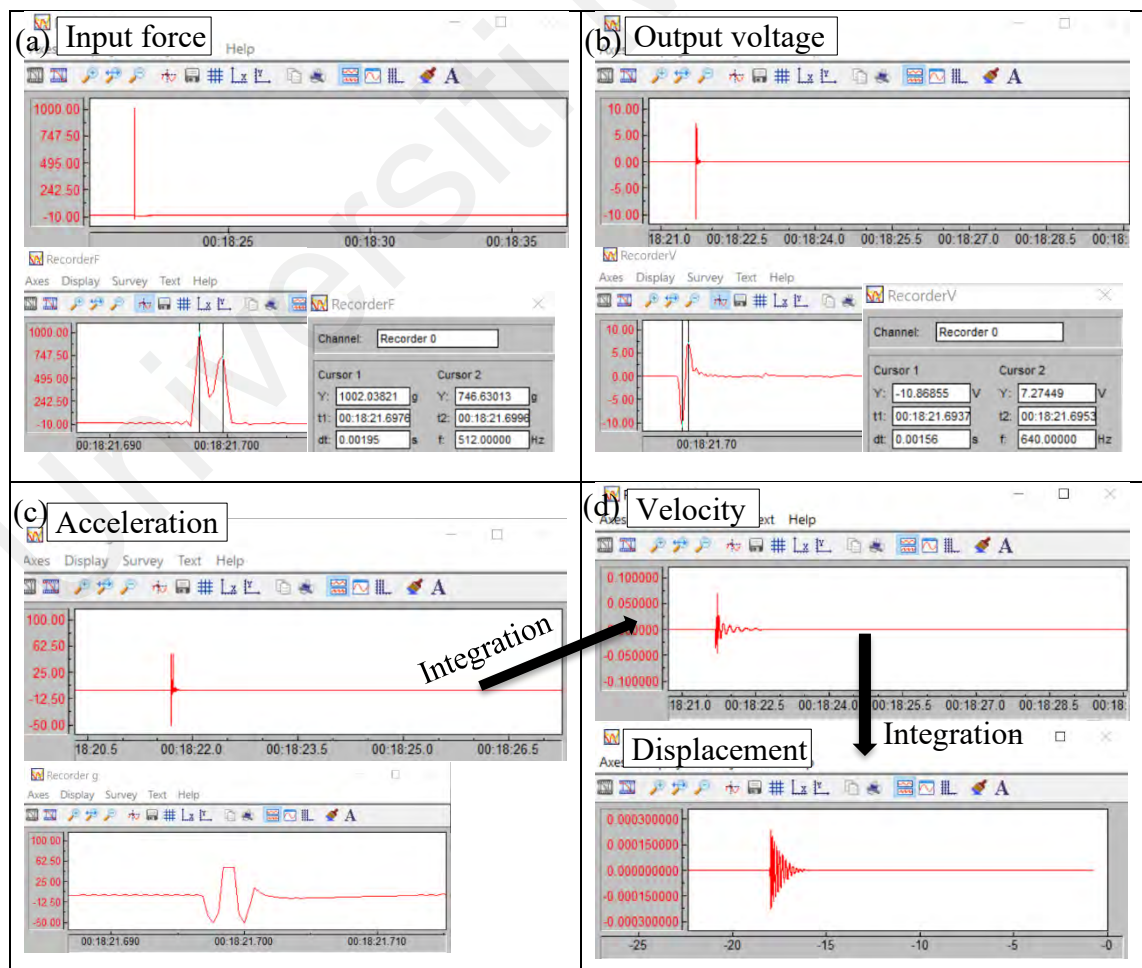(d) Impedance matching result of the Hull PEH
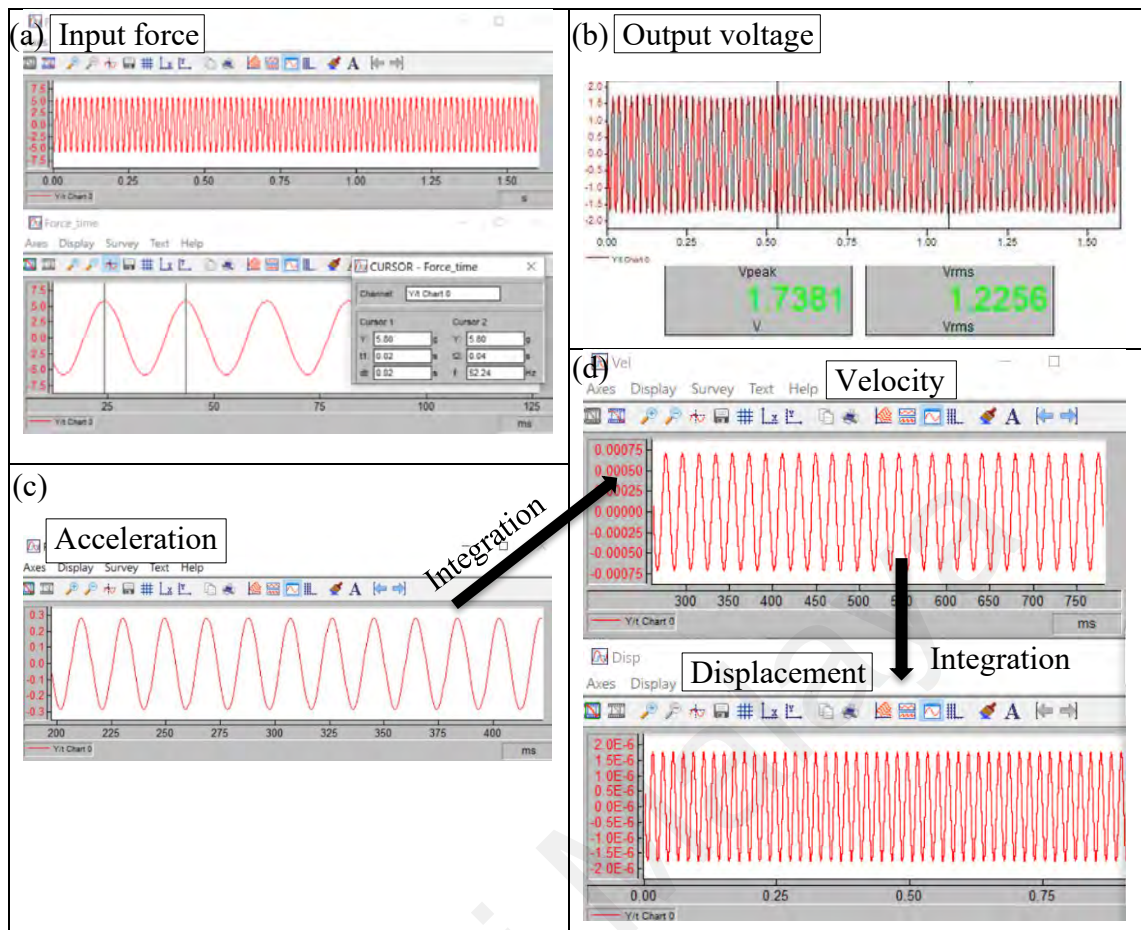
Figure 4.32 Raw data for Hull PEH's energy conversion efficiency calculation
i.e., (a) force, (b) voltage, (c) acceleration, and (d) displacement under
10 N, 50 Hz harmonic force with band filter between 45-55 Hz
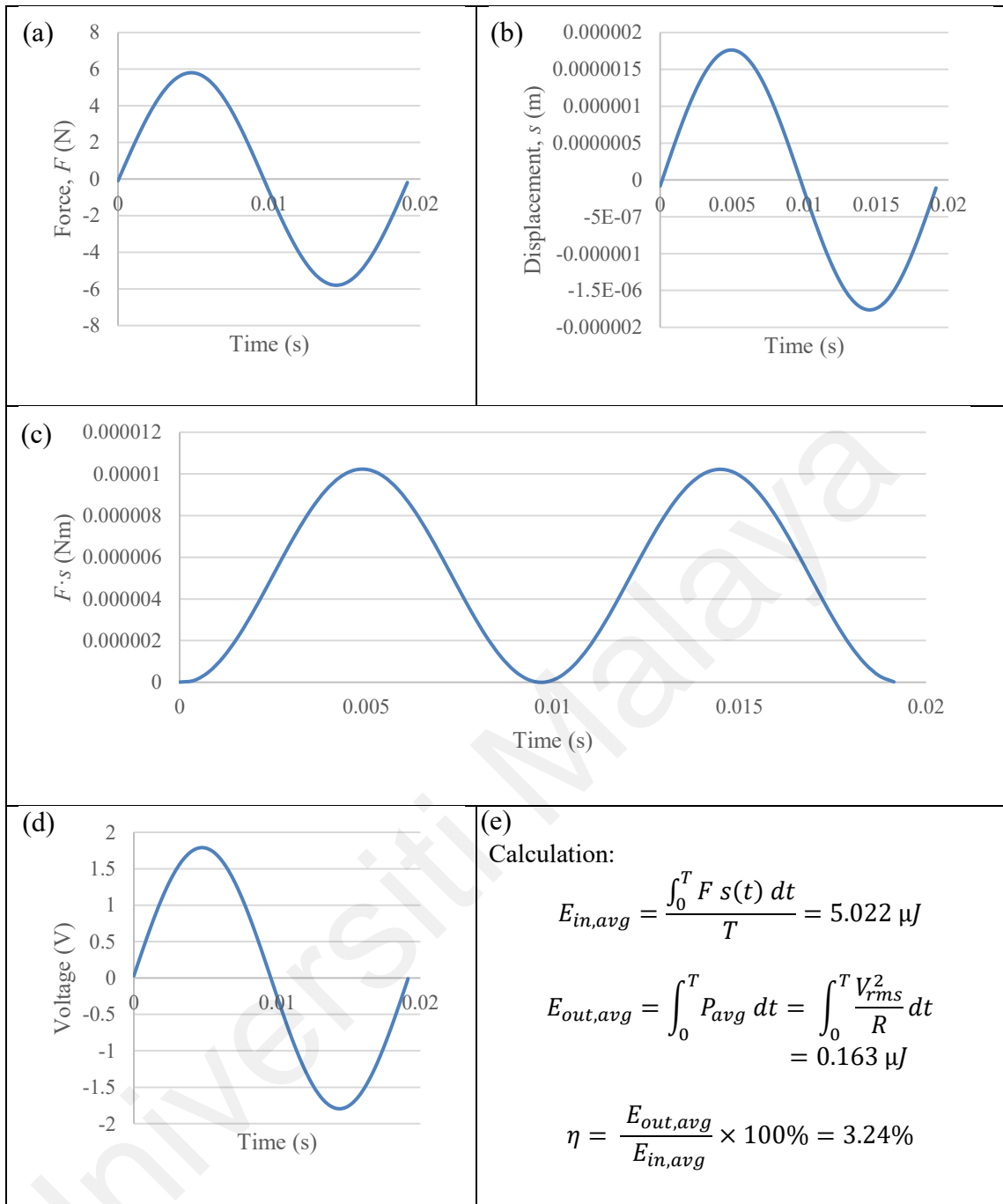
Figure 4.33 (a) Force, (b) displacement, (c) input and (d) output energy curves per cycle extracted from the raw data, and (e) the efficiency calculation for Hull PEH under 10 N, 50 Hz harmonic force with band filter between 45-55 Hz

(a)

- Graph of input force in frequency domain shows the normal phenomenon where the shaker excites the Hull PEH under several harmonic frequencies within the useful frequency range of 5-700 Hz.

(b) Input force
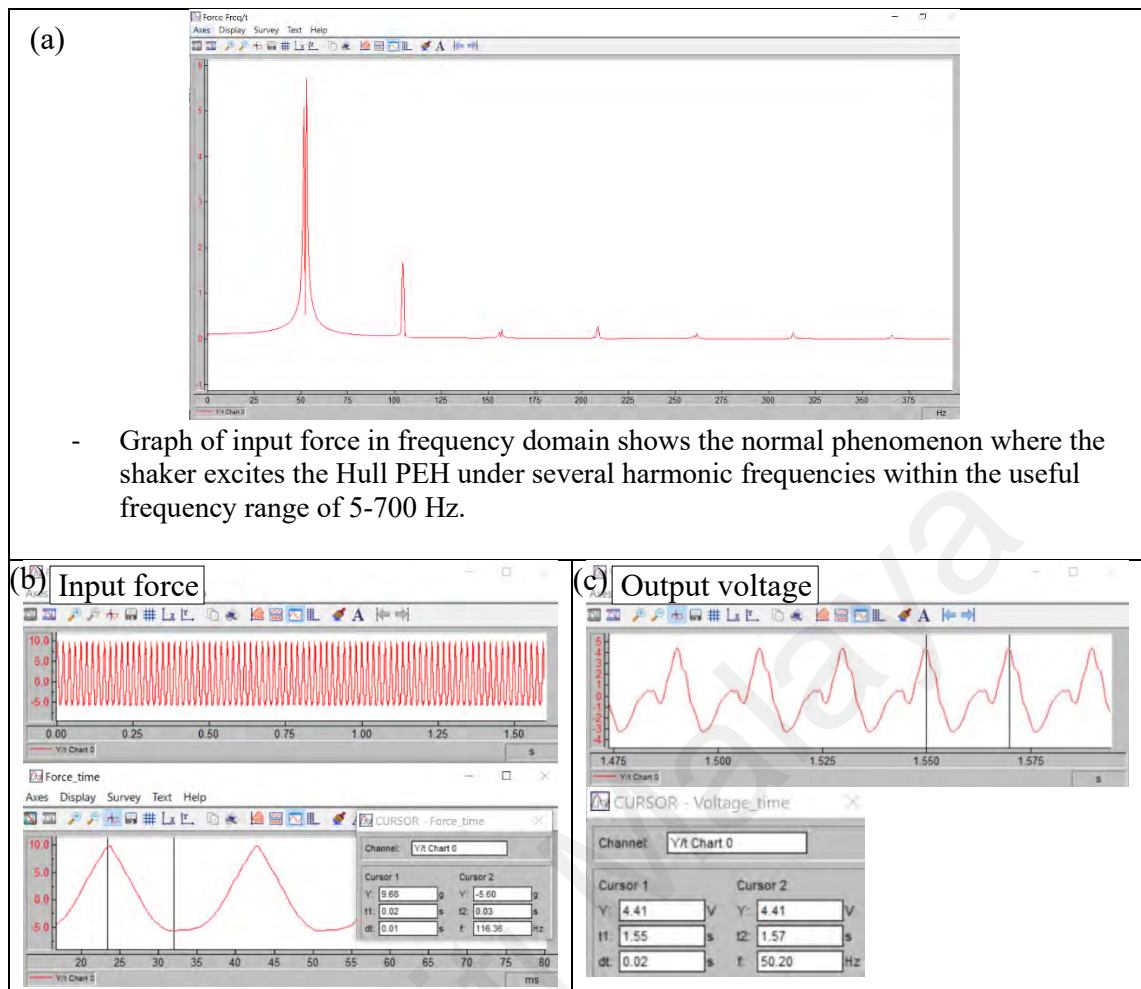
(c) Output voltage

Figure 4.34 (a) Graph of input force in frequency domain; Raw data for Hull PEH's energy conversion efficiency calculation i.e., (b) input force and (c) output voltage under 10 N, 50 Hz harmonic force with band filter between 5-700 Hz
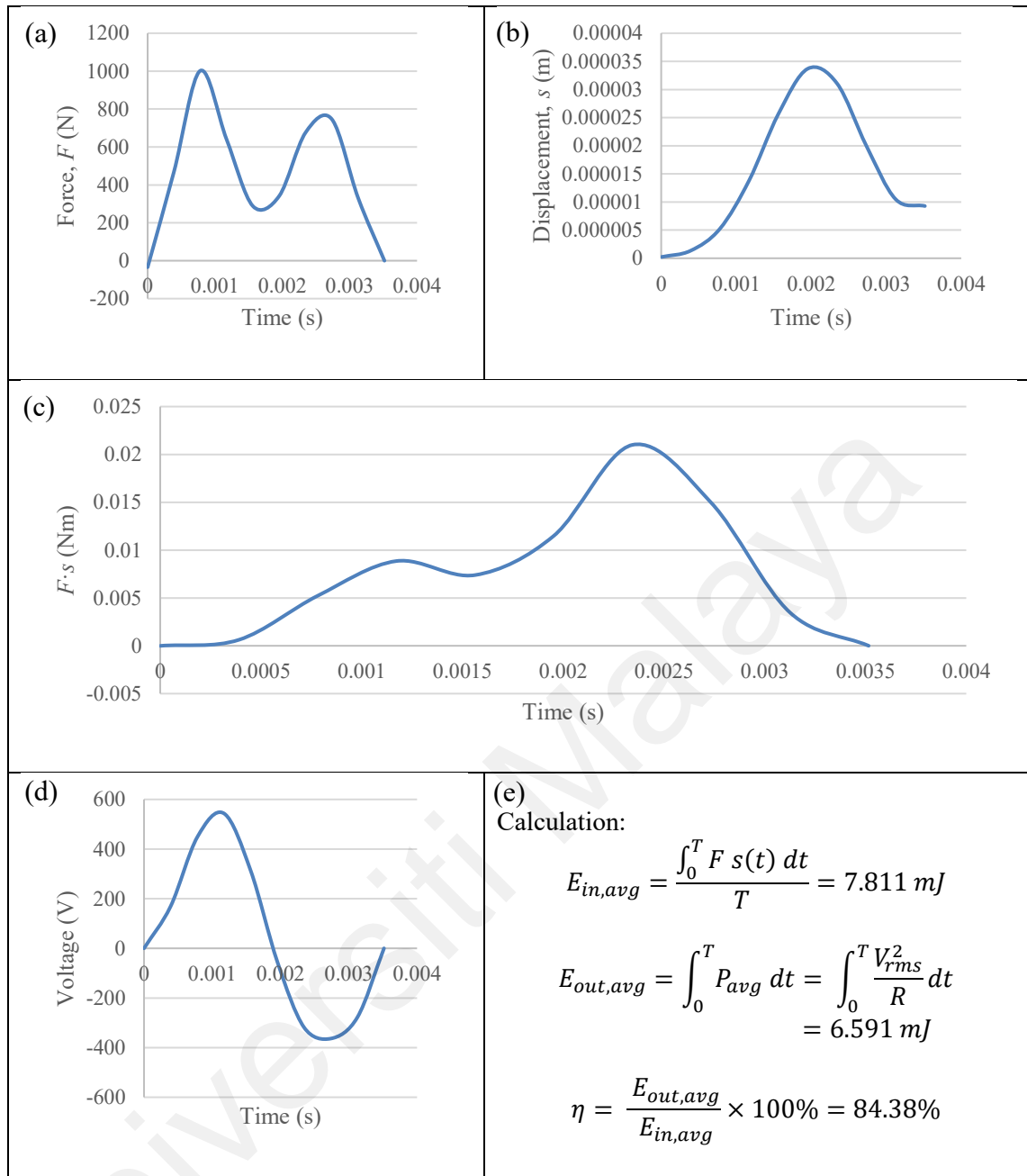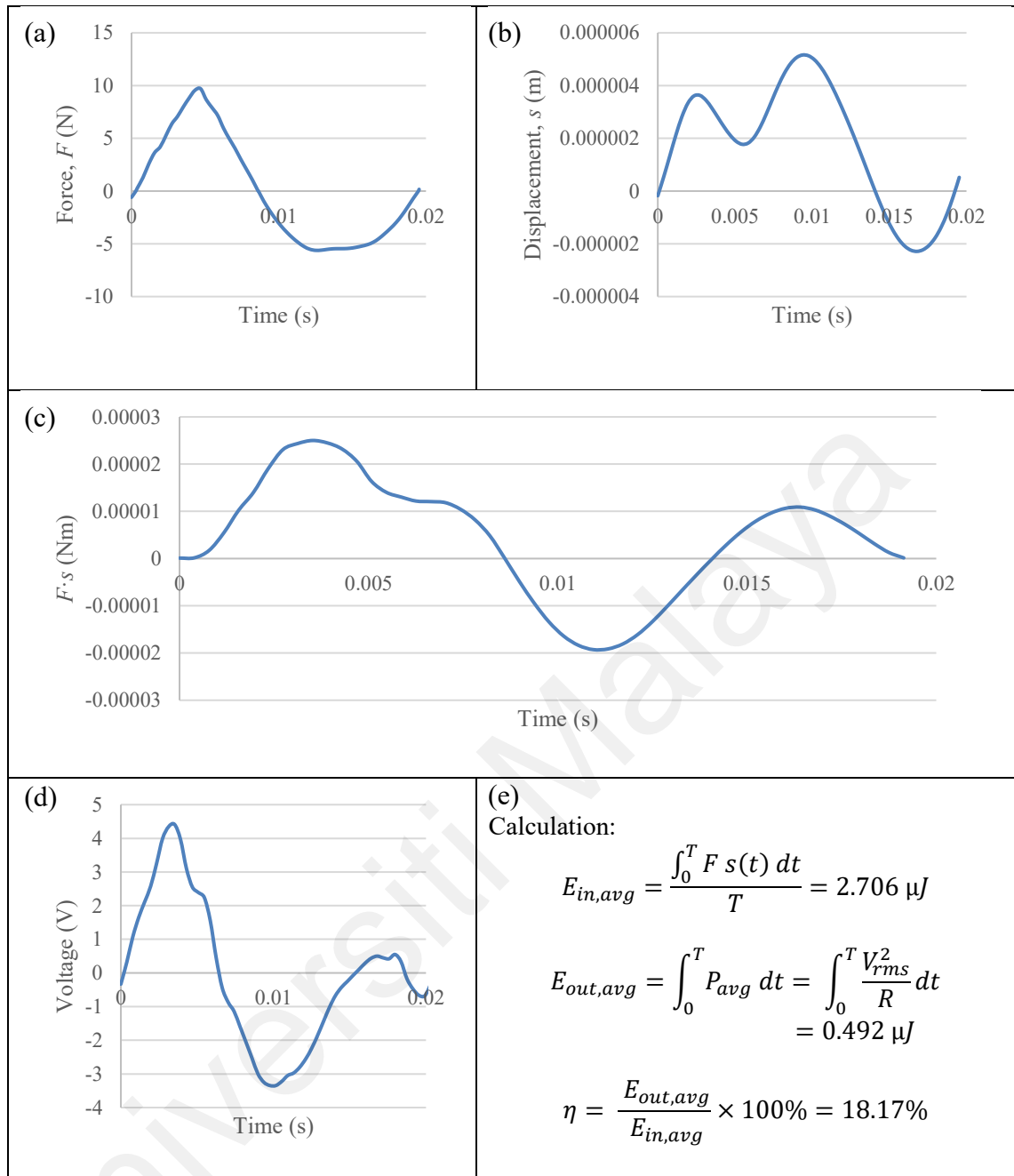
Figure 4.35 (a) Force, (b) displacement, (c) input and (d) output energy curves per cycle extracted from the raw data, and (e) the efficiency calculation for Hull PEH under 10 N, 50 Hz harmonic force with band filter between 5-700 Hz useful frequency range

Lastly, a rapid charging test has been carried out on the Hull PEH with an energy harvesting circuit under the higher frequency loading. The Hull PEH is excited under 10 N at 50 Hz with a connected LTC-3588 harvesting circuit. Figure 4.36 shows the rectified output voltage and the corresponding stored energy in the capacitor. The stored energy in the capacitor is calculated through equation [4.12].

140

$$E_s(t) = \frac{1}{2}C[V(t)]^2 \qquad\qquad [4.12]$$

where $E_s(t)$ = stored energy at instant time, $t$; $C$ = capacitance, and $V(t)$ = measured voltage across the capacitor at instant time, $t$ (Gharieb & Ibrahim, 2012).
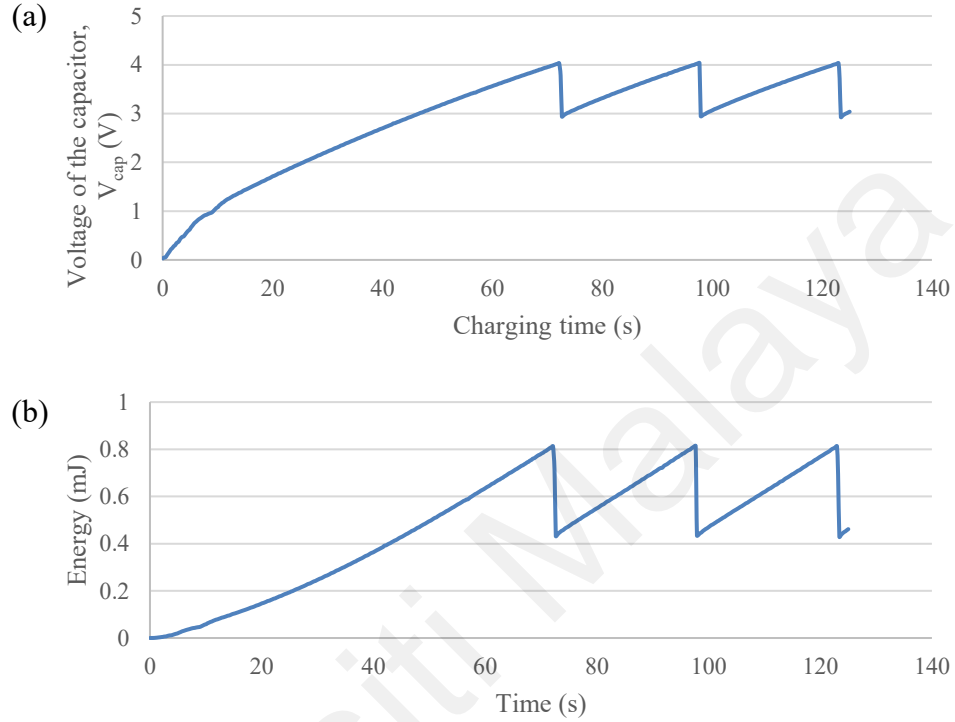


Figure 4.36 (a) Voltage across the 100 µF capacitor under 10 N at 50 Hz rapid charging process and (b) the corresponding stored energy in the capacitor

It requires 72 s to charge the 100 µF capacitor from 0 to 4 V. After the capacitor discharges to the 5 mm red LED, it requires 26 s for recharging the capacitor from 3 to 4 V in each cycle. The output voltage has been increased and stored with more than 3.3 V, which is practical to power up some microcontroller applications (Gharieb & Ibrahim, 2012). For example, the IoT development boards such as Arduino Nano 33 IoT or SparkFun ESP32 Thing have a 3.3 V or 2.2 V to 3.6 V operating voltage range. Hence, it is believed that a sustainable power source for the IoT system has been secured by having the developed Hull PEH to achieve a wireless real-time monitoring system in the future.

## CHAPTER 5: CONCLUSION AND RECOMMENDATIONS

### 5.1 Conclusion

In conclusion, a novel compressive mechanical amplifier structure (i.e., Hull structure) has been successfully designed and developed for a PEH in a high force environment. A CPC-FEM has been developed to evaluate the PEH in the FEA high forcing environment. A safety factor of 2 is implemented to ensure the durability and longevity of the proposed structure. The best compressive PEH design is selected based on the energy harvesting performance, in terms of stress analysis, loading capacity, and power generation. Parametric optimization has been carried out on the Hull structure, such as the inclined angle, linkage length, joint length, base length, base thickness, and linkage thickness. The relationship of each structural parameter on the power output has been investigated, where the optimum inclined angle plays the most important role in enhancing the power output of the Hull PEH. An improved FEA power output of 11.34 mW is obtained for the optimized Hull PEH under 1 kN of sinusoidal force at 2 Hz, which is 178% larger than the unoptimized case. It has a comparatively higher volume power density of 1.817 kW/m$^3$ than the existing designs.

On the other hand, the Hull PEH is tested under impact force experimentally, where its energy harvesting performance is firstly evaluated based on the open-circuit output voltage. The experimental result shows less than 5.2% of deviation with the FEA under 10 - 1 kN of impact forces. The Hull PEH exhibits at least 5 times larger voltage output than the benchmark case and at least 14 times greater than the standalone PZT. Thus, the Hull amplifier structure is proven to have a great effect in magnifying the input force and compressing the PZT on a larger scale. The power output of the Hull PEH under 1 kN of impact force is then evaluated by conducting impedance matching. A maximum peak power output of 7.16 W is produced across a 50 kΩ of optimum load resistance. It shows only a 3.5% of deviation in the peak voltage and 6.9% of deviation in the power output

with the FEA. Under 10 N of sinusoidal force at 50 Hz, the Hull PEH shows an average power output of 54 µW at 180 kΩ through impedance matching. Hence, the FEA result has been verified satisfactorily under both harmonic and impact forces. It also proves the high reliability of the developed CPC-FEM.

From the amplification effect aspect, an analytical force amplification factor of 9.72 is proven for the Hull structure from the kinematic theorem with the consideration of beam deformation. The Hull structure shows an amplification ratio of 16.9 if compared to the standalone PZT plate based on the experimental output voltage result. Hence, the Hull structure is said to have a high amplification ratio if compared with the existing single-stage amplifier structure. Besides, it achieves 84.38% of energy conversion efficiency under 1 kN impact force based on the average input and output energies. Under a rapid charging test, the Hull PEH can store more than 3.3 V with an LTC-3588 energy harvesting circuit under the higher frequency loading. Hence, it is capable to act as a sustainable energy source for some microcontroller applications.

Lastly, the performance of the proposed PEH has been compared with a benchmark tensile PEH (i.e., Rectangular Cymbal structure). They are compared under the same loading environment with the same size of PZT plate to ensure a fair comparison. An FEA power output of 11.34 mW is obtained from the Hull PEH across a theoretical optimum resistance of 5.99 MΩ. It is 3.08 times larger than the Rectangular Cymbal PEH under 1 kN of sinusoidal force at 2 Hz. In the experiment, the Hull PEH exhibits at least 5 times larger voltage output than the Rectangular Cymbal PEH under both harmonic and impact forces. Under 1 kN of impact force, the Hull PEH generates 7.16 W of power output across 50 kΩ, which is 37.68 times higher than that of the benchmark PEH. Thus, the Hull PEH exhibits better harvesting performance in terms of voltage and power output, despite the loading environment either in high or low force.

From another perspective, the Hull PEH has a lower stress concentration, higher loading capacity, higher amplification factor, and is more cost-effective than the Rectangular Cymbal PEH. It has a greater capability to work in a higher force environment since the PZT's compressive yield strength is 10 times higher than its tensile yield strength. It is also proven that the tensile-typed benchmark structure will reach the saturated stress at a lower force with limited power output if compare with the Hull PEH. In addition, the Rectangular Cymbal structure has a restricted cavity height and linkage length that may limit the amplification effect. Additional casing or substrate is needed to overcome the stress concentration issue in the benchmark case. In contrast, the Hull structure has higher flexibility in the design with a larger forcing area as well. In short, the Hull PEH is concluded to have a better overall performance than the benchmark Rectangular Cymbal PEH in both FEA and experiment. All in all, a novel Hull amplifier structure has been successfully developed by achieving all the objectives of this study.

## 5.2    Novelty and Contribution of Study

The main contribution of this study is the design and development of a novel compressive mechanical amplifier structure (i.e., Hull structure) for PEH with enhanced performance under a high force environment. It could overcome the drawbacks of the conventional tensile-typed structure by having higher efficiency in terms of loading capacity and power output.

Next, the developed analytical model could determine the performance of the proposed structure in terms of force amplification factor, prior to the experimental result. It could serve as a useful cross-reference to ease the parametric optimization of the Hull structure under another forcing environment in the future.

The proposed new performance indicator, (i.e., the level of PZT's utilization) shows better performance in FEA optimization instead of using the conventional indicators (i.e.,

maximum design stress limit and total strain energy transmission efficiency). This is because a higher value of PZT's average nodal stress indicates a higher level of PZT's utilization, which will lead to larger power output.

Moreover, this study contributes by presenting a comprehensive methodology to evaluate the energy harvesting performance of a PEH. The similar procedure can be used for other potential designs in future research. It shall act as a useful guideline for researchers who are new to this field.

Other than publishing the research findings in the ISI-indexed journal, this study has been presented and discussed at an international conference. It has attracted much attention from other researchers. Besides, this work has secured a gold award in an international competition recently which shows its high acceptability and recognition.

## 5.3    Recommendations for Future Work

From the structural design perspective, there is still room for improvement on the current design, although it has a great energy harvesting performance among the single-stage PEH. For example, it can be further improved by having a d33 PZT stack material with an additional outer Hull structure to achieve a multistage amplifier structure. More studies can be done to achieve a low-cost multistage Hull structure with a compact size. Additional features such as fillet can be included to further reduce the stress concentration.

Other than energy harvesting from the Hull PEH, further research on the suitable application on measurement is recommended. Since the output voltage result appears linearly to the input force, the Hull PEH shows a high potential to work as a WIM sensor, such as a transportation monitoring sensor in detecting the overloaded vehicle or applied in the load detection system in the conveyor belt of a production line. Useful information

such as the vehicle's speed, traffic flow volume, and WIM can be retrieved from the voltage signal.

For the experimental testing, another model of shaker could be used to test the Hull PEH and the benchmark PEH under a higher harmonic force. It is suggested to include field testing such as burying the Hull PEH under the pavement or embedding it in the conveyor belt so that the energy harvesting performance can be verified. Else, a scaled-down laboratory experiment can be carried out using a road traffic simulator, which is capable to simulate the vehicle excitation with various speeds and weight (Vázquez-Rodríguez, Jiménez, Pardo, González, & de Frutos, 2019). An illustration of the possible experimental setup is shown in Figure 5.1.
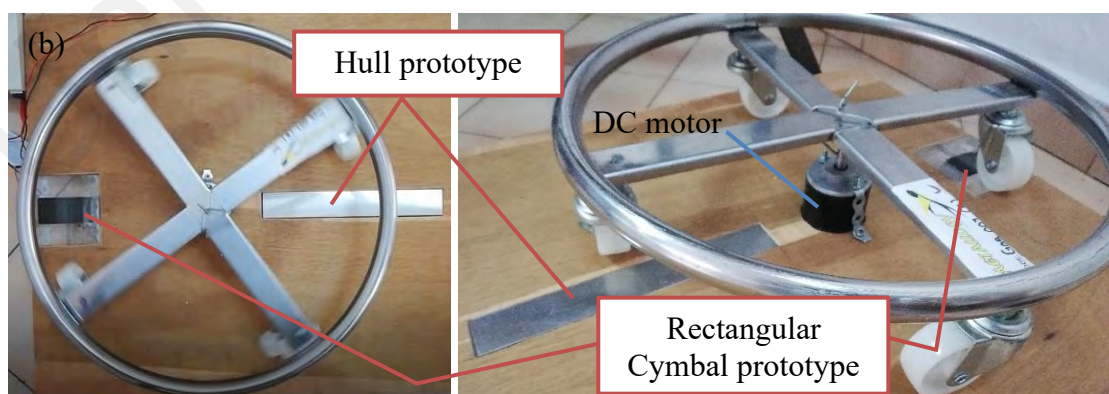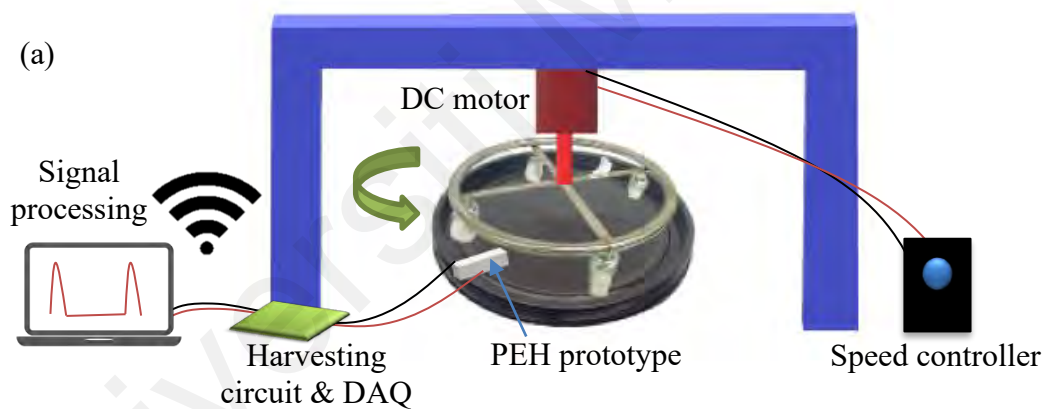


Figure 5.1 (a) Recommended road traffic simulator experimental setup with the (b) fabricated prototypes

A graphical method by using a slow-motion feature camera can be used to validate the reliability of the speed obtained. A tachometer can be used to verify the speed of rotation as well. In addition, the wireless transmission of data can be tested with a developed IoT technology in the future. Hence, the performance of the proposed PEH to work as a wireless self-powered real-time transportation monitoring sensor can be investigated.

Last but not least, this study can be utilized as a guideline in designing a high-efficiency mechanical amplifier structure for PEH. It can be served as a stepping stone towards the implementation of the piezoelectric energy harvesting technique in Malaysia especially under a high force environment.

# REFERENCES

Abdelkefi, A., Najar, F., Nayfeh, A. H., & Ayed, S. B. (2011). An energy harvester using piezoelectric cantilever beams undergoing coupled bending–torsion vibrations. *Smart Materials and Structures, 20*(11), 115007. doi:10.1088/0964-1726/20/11/115007

Analog Devices. (2019). LTC3588–1 Nanopower Energy Harvesting Power Supply. Retrieved from https://www.analog.com/en/products/ltc3588-1.html#product-overview

Arnold, D., Kinsel, W., Clark, W., & Mo, C. (2011). Exploration of New Cymbal Design in Energy Harvesting. *Proceedings of SPIE - The International Society for Optical Engineering, 7977*. doi:10.1117/12.880614

Avvari, P. V., Yang, Y., & Soh, C. K. (2016). Long-term fatigue behavior of a cantilever piezoelectric energy harvester. *Journal of Intelligent Material Systems and Structures, 28*(9), 1188-1210. doi:10.1177/1045389X16667552

Bejarano, F., Feeney, A., & Lucas, M. (2014). A cymbal transducer for power ultrasonics applications. *Sensors and Actuators A: Physical, 210*, 182-189. doi:https://doi.org/10.1016/j.sna.2014.02.024

Ben Ayed, S., Abdelkefi, A., Najar, F., & Hajj, M. R. (2013). Design and Performance of Variable Shaped Piezoelectric Energy Harvesters. *Journal of Intelligent Material Systems and Structures, 25*. doi:10.1177/1045389X13489365

Benasciutti, D., Moro, L., Zelenika, S., & Brusa, E. (2009). Vibration energy scavenging via piezoelectric bimorphs of optimized shapes. *Microsystem Technologies, 16*, 657-668. doi:10.1007/s00542-009-1000-5

Bencheikh, N., Pagès, A., Forissier, T., Porchez, T., Kras, A., Badel, A., & Formosa, F. (2014, 23e25 June). *A bistable piezoelectric harvester for wideband mechanical frequency excitation.* Paper presented at the 14th International Conference on New Actuators, Bremen, Germany.

Boisseau, S., Despesse, G., & Seddik, B. A. (2012). Electrostatic conversion for vibration energy harvesting. *Small-Scale Energy Harvesting*, 1-39.

Buscarello, R. T. (1987). *Practical Solutions of Machinery and Maintenance Vibration Problems*: Update International.

CEDRAT TECHNOLOGIES. (2020). Amplified Piezo Actuators. Retrieved from https://www.cedrat-technologies.com/en/products/actuators/amplified-piezo-actuators.html

Challa, V. R., Prasad, M. G., Shi, Y., & Fisher, F. T. (2008). A vibration energy harvesting device with bidirectional resonance frequency tunability. *Smart Material Structures, 17*, 015035. doi:10.1088/0964-1726/17/01/015035

Chen, J., Qiu, Q., Han, Y., & Lau, D. (2019). Piezoelectric materials for sustainable building structures: Fundamentals and applications. *Renewable and Sustainable Energy Reviews, 101*, 14-25. doi:https://doi.org/10.1016/j.rser.2018.09.038

Chen, W. S., Wang, Y., & Deng, W. (2017). Deformable force amplification frame promoting piezoelectric stack energy harvesting: Parametric model, experiments and energy analysis. *Journal of Intelligent Material Systems and Structures, 28*(7), 827-836. doi:10.1177/1045389x16657426

Cho, J. Y., Kim, K.-B., Hwang, W. S., Yang, C. H., Ahn, J. H., Hong, S. D., . . . Sung, T. H. (2019). A multifunctional road-compatible piezoelectric energy harvester for autonomous driver-assist LED indicators with a self-monitoring system. *Applied Energy, 242*, 294-301. doi:https://doi.org/10.1016/j.apenergy.2019.03.075

Choi, K.-B., Lee, J. J., Kim, G. H., Lim, H. J., & Kwon, S. G. (2018). Amplification ratio analysis of a bridge-type mechanical amplification mechanism based on a fully compliant model. *Mechanism and Machine Theory, 121*, 355-372. doi:https://doi.org/10.1016/j.mechmachtheory.2017.11.002

Chua, H., Kok, B., & Goh, H. (2014). Modelling and design analyses of a piezoelectric cymbal transducer (PCT) structure for energy harvesting application. *Energy and Sustainability V, 186*, 103.

Clark, L., Shirinzadeh, B., Pinskier, J., Tian, Y., & Zhang, D. (2018). Topology optimisation of bridge input structures with maximal amplification for design of flexure mechanisms. *Mechanism and Machine Theory, 122*, 113-131. doi:https://doi.org/10.1016/j.mechmachtheory.2017.12.017

Covaci, C., & Gontean, A. (2020). Piezoelectric Energy Harvesting Solutions: A Review. *Sensors, 20*(12), 3512.

Daniels, A., Zhu, M., & Tiwari, A. (2013). Design, analysis and testing of a piezoelectric flex transducer for harvesting bio-kinetic energy. *Journal of Physics Conference Series, 476*, 2047. doi:10.1088/1742-6596/476/1/012047

Dietl, J., & Garcia, E. (2010). Beam Shape Optimization for Power Harvesting. *Journal of Intelligent Material Systems and Structures - J INTEL MAT SYST STRUCT, 21*, 633-646. doi:10.1177/1045389X10365094

Dutoit, N. E., Wardle, B. L., & Kim, S.-G. (2005). DESIGN CONSIDERATIONS FOR MEMS-SCALE PIEZOELECTRIC MECHANICAL VIBRATION ENERGY HARVESTERS. *Integrated Ferroelectrics, 71*(1), 121-160. doi:10.1080/10584580590964574

Erturk, A., Hoffmann, J., & Inman, D. J. (2009). A piezomagnetoelastic structure for broadband vibration energy harvesting. *Applied Physics Letters, 94*(25), 254102. doi:10.1063/1.3159815

Evans, M., Tang, L., Tao, K., & Aw, K. (2019). Design and optimisation of an underfloor energy harvesting system. *Sensors and Actuators A: Physical, 285*, 613-622. doi:https://doi.org/10.1016/j.sna.2018.12.002

Evans, M., Tang, L. H., & Aw, K. C. (2018). Modelling and optimisation of a force amplification energy harvester. *Journal of Intelligent Material Systems and Structures, 29*(9), 1941-1952. doi:10.1177/1045389x18754352

Fan, K., Tan, Q., Liu, H., Zhang, Y., & Cai, M. (2019). Improved energy harvesting from low-frequency small vibrations through a monostable piezoelectric energy harvester. *Mechanical Systems and Signal Processing, 117*, 594-608. doi:https://doi.org/10.1016/j.ymssp.2018.08.001

Feenstra, J., Granstrom, J., & Sodano, H. (2008). Energy harvesting through a backpack employing a mechanically amplified piezoelectric stack. *Mechanical Systems and Signal Processing, 22*(3), 721-734. doi:https://doi.org/10.1016/j.ymssp.2007.09.015

Gao, X. (2011). *Vibration and flow energy harvesting using piezoelectric cantilevers.* (Ph.D. thesis), Ph.D. thesis, Drexel University, Philadelphia, PA.

Gharieb, W., & Ibrahim, S. (2012). Power Analysis for Piezoelectric Energy Harvester. *Energy and Power Engineering, 04*, 496-505. doi:10.4236/epe.2012.46063

Glynne-Jones, P., Beeby, S. P., & White, N. M. (2001). Towards a piezoelectric vibration-powered microgenerator. *IEE Proceedings - Science, Measurement and Technology, 148*(2), 68-72. doi:10.1049/ip-smt:20010323

Guan, M., & Liao, W.-H. (2006). *On the energy storage devices in piezoelectric energy harvesting - art. no. 61690C* (Vol. 6169).

Haertling, G. H. (1999). Ferroelectric Ceramics: History and Technology. *Journal of the American Ceramic Society, 82*(4), 797-818. doi:10.1111/j.1151-2916.1999.tb01840.x

Harne, R. L., & Wang, K. W. (2013). A review of the recent research on vibration energy harvesting via bistable systems. *Smart Materials and Structures, 22*(2), 023001. doi:10.1088/0964-1726/22/2/023001

Hu, G., Tang, L., Das, R., & Marzocca, P. (2018). A two-degree-of-freedom piezoelectric energy harvester with stoppers for achieving enhanced performance. *International Journal of Mechanical Sciences, 149*, 500-507. doi:https://doi.org/10.1016/j.ijmecsci.2017.07.051

Huang, D., Zhou, S., & Litak, G. (2019). Theoretical analysis of multi-stable energy harvesters with high-order stiffness terms. *Communications in Nonlinear Science and Numerical Simulation, 69*, 270-286. doi:https://doi.org/10.1016/j.cnsns.2018.09.025

Jasim, A., Wang, H., Yesner, G., Safari, A., & Maher, A. (2017). Optimized design of layered bridge transducer for piezoelectric energy harvesting from roadway. *Energy, 141*, 1133-1145. doi:https://doi.org/10.1016/j.energy.2017.10.005

Kang, G.-d., & Cao, Y.-m. (2014). Application and modification of poly (vinylidene fluoride)(PVDF) membranes–a review. *Journal of membrane science, 463*, 145-165.

Karim, M. R., Ibrahim, N. I., Saifizul, A. A., & Yamanaka, H. (2014). Effectiveness of vehicle weight enforcement in a developing country using weigh-in-motion sorting system considering vehicle by-pass and enforcement capability. *IATSS research, 37*(2), 124-129.

Kaur, S., Graak, P., Gupta, A., Chhabra, P., Kumar, D., & Shetty, A. (2016). Effect of various shapes and materials on the generated power for piezoelectric energy harvesting system. *AIP Conference Proceedings, 1724*(1), 020076. doi:10.1063/1.4945196

Keshmiri, A., Deng, X., & Wu, N. (2019). New energy harvester with embedded piezoelectric stacks. *Composites Part B: Engineering, 163*, 303-313. doi:https://doi.org/10.1016/j.compositesb.2018.11.028

Keshmiri, A., & Wu, N. (2018). Structural stability enhancement by nonlinear geometry design and piezoelectric layers. *Journal of Vibration and Control, 25*(3), 695-710. doi:10.1177/1077546318794540

Kim, H., Tadesse, Y., & Priya, S. (2009). Piezoelectric Energy Harvesting. In S. Priya & D. J. Inman (Eds.), *Energy Harvesting Technologies* (pp. 3-39). Boston, MA: Springer US.

Kim, H. W., Batra, A., Priya, S., Uchino, K., Markley, D., Newnham, R. E., & Hofmann, H. F. (2004). Energy Harvesting Using a Piezoelectric "Cymbal" Transducer in Dynamic Environment. *Japanese Journal of Applied Physics, 43*(9A), 6178-6183. doi:10.1143/jjap.43.6178

Kim, S., Clark, W. W., & Wang, Q.-M. (2005). Piezoelectric Energy Harvesting with a Clamped Circular Plate: Experimental Study. *Journal of Intelligent Material Systems and Structures, 16*(10), 855-863. doi:10.1177/1045389X05054043

Kuang, Y., Chew, Z. J., Dunville, J., Sibson, J., & Zhu, M. (2021). Strongly coupled piezoelectric energy harvesters: Optimised design with over 100 mW power, high durability and robustness for self-powered condition monitoring. *Energy Conversion and Management, 237*, 114129. doi:https://doi.org/10.1016/j.enconman.2021.114129

Kuang, Y., Chew, Z. J., & Zhu, M. (2020). Strongly coupled piezoelectric energy harvesters: Finite element modelling and experimental validation. *Energy Conversion and Management, 213*, 112855. doi:https://doi.org/10.1016/j.enconman.2020.112855

Kuang, Y., Daniels, A., & Zhu, M. (2017). A sandwiched piezoelectric transducer with flex end-caps for energy harvesting in large force environments. *Journal of Physics D: Applied Physics, 50*. doi:10.1088/1361-6463/aa7b28

Kuang, Y., Yang, Z., & Zhu, M. (2016). Design and characterisation of a piezoelectric knee-joint energy harvester with frequency up-conversion through magnetic plucking. *Smart Materials and Structures, 25*(8), 085029. doi:10.1088/0964-1726/25/8/085029

Lee, H. J., Sherrit, S., Tosi, L. P., Walkemeyer, P., & Colonius, T. (2015). Piezoelectric Energy Harvesting in Internal Fluid Flow. *Sensors, 15*(10). doi:10.3390/s151026039

Lee, Y.-L., & Barkey, M. E. (2012). Chapter 4 - Stress-Based Uniaxial Fatigue Analysis. In Y.-L. Lee, M. E. Barkey, & H.-T. Kang (Eds.), *Metal Fatigue Analysis Handbook* (pp. 115-160). Boston: Butterworth-Heinemann.

Leinonen, M., Palosaari, J., Juuti, J., & Jantunen, H. (2013). Combined electrical and electromechanical simulations of a piezoelectric cymbal harvester for energy harvesting from walking. *Journal of Intelligent Material Systems and Structures, 25*(4), 391-400. doi:10.1177/1045389X13500573

Li, H., Tian, C., & Deng, Z. D. (2014). Energy harvesting from low frequency applications using piezoelectric materials. *Applied physics reviews, 1*(4), 041301.

Li, L., Xu, J., Liu, J., & Gao, F. (2018). Recent progress on piezoelectric energy harvesting: structures and materials. *Advanced Composites and Hybrid Materials, 1*(3), 478-505. doi:10.1007/s42114-018-0046-1

Li, X., Guo, M., & Dong, S. (2011). A Flex-Compressive-Mode Piezoelectric Transducer for Mechanical Vibration/Strain Energy Harvesting. *IEEE transactions on ultrasonics, ferroelectrics, and frequency control, 58*, 698-703. doi:10.1109/TUFFC.2011.1862

Li, X., Yu, K., Upadrashta, D., & Yang, Y. (2019). Multi-branch sandwich piezoelectric energy harvester: mathematical modeling and validation. *Smart Materials and Structures, 28*(3), 035010. doi:10.1088/1361-665x/aaf8bf

Li, Z., Zu, J., & Yang, Z. (2018). Introducing hinge mechanisms to one compressive-mode piezoelectric energy harvester. *Journal of Renewable and Sustainable Energy, 10*(3), 034704. doi:10.1063/1.4997184

Lin, L., Hu, Y., Xu, C., Zhang, Y., Zhang, R., Wen, X., & Wang, Z. L. (2013). Transparent flexible nanogenerator as self-powered sensor for transportation monitoring. *Nano Energy, 2*(1), 75-81.

Ling, M., Cao, J., Zeng, M., Lin, J., & Inman, D. J. (2016). Enhanced mathematical modeling of the displacement amplification ratio for piezoelectric compliant mechanisms. *Smart Materials and Structures, 25*(7), 075022.

Liu, H., Hua, R., Lu, Y., Wang, Y., Salman, E., & Liang, J. (2019). Boosting the efficiency of a footstep piezoelectric-stack energy harvester using the synchronized switch technology. *Journal of Intelligent Material Systems and Structures, 30*(6), 813-822. doi:10.1177/1045389X19828512

Liu, W., Badel, A., Formosa, F., Wu, Y., & Agbossou, A. (2013a). *Novel piezoelectric bistable oscillator architecture for wideband vibration energy harvesting* (Vol. 22).

Liu, W., Badel, A., Formosa, F., Wu, Y., & Agbossou, A. (2013b). *Wideband energy harvesting using the combination of optimized synchronous electric charge extraction circuit and bistable harvester* (Vol. 22).

Liu, X., & Wang, J. (2019). Performance Exploration of A Radially Layered Cymbal Piezoelectric Energy Harvester under Road Traffic Induced Low Frequency Vibration. *IOP Conference Series: Materials Science and Engineering, 542*, 012075. doi:10.1088/1757-899x/542/1/012075

Luo, L., Liu, D., Zhu, M., & Ye, J. (2017). Metamodel-assisted design optimization of piezoelectric flex transducer for maximal bio-kinetic energy conversion. *Journal of Intelligent Material Systems and Structures, 28*(18), 2528-2538. doi:10.1177/1045389X17689943

M'boungui, G., Adendorff, K., Naidoo, R., Jimoh, A. A., & Okojie, D. E. (2015). A hybrid piezoelectric micro-power generator for use in low power applications. *Renewable and Sustainable Energy Reviews, 49*, 1136-1144. doi:https://doi.org/10.1016/j.rser.2015.04.143

Ma, H.-W., Yao, S.-M., Wang, L.-Q., & Zhong, Z. (2006). Analysis of the displacement amplification ratio of bridge-type flexure hinge. *Sensors and Actuators A: Physical, 132*(2), 730-736. doi:https://doi.org/10.1016/j.sna.2005.12.028

Ma, T., Chen, N., Wu, X., Du, F., & Ding, Y. (2019). Investigation on the design and application of 3-dimensional wide-band piezoelectric energy harvester for low amplitude vibration sources. *Smart Materials and Structures, 28*(10), 105013. doi:10.1088/1361-665x/ab377a

Mateu, L., & Moll, F. (2005). Optimum Piezoelectric Bending Beam Structures for Energy Harvesting using Shoe Inserts. *Journal of Intelligent Material Systems and Structures, 16*. doi:10.1177/1045389X05055280

Mei, J., & Li, L. (2013). Split-electrode piezoelectric scavengers for harvesting energy from torsional motions. *Journal of Physics: Conference Series, 476*, 012136. doi:10.1088/1742-6596/476/1/012136

Mo, C., Arnold, D., Kinsel, W. C., & Clark, W. W. (2013). Modeling and experimental validation of unimorph piezoelectric cymbal design in energy harvesting. *Journal of Intelligent Material Systems and Structures, 24*(7), 828-836.

Mohammadi, M. M. (2013). A Comparison Between Quartz and PZT Ceramic for Sensoric Applications. *Research Desk, Oct-Dec* (2(4).), 321-325.

Mossi, K. M., Selby, G. V., & Bryant, R. G. (1998). Thin-layer composite unimorph ferroelectric driver and sensor properties. *Materials Letters, 35*(1), 39-49. doi:https://doi.org/10.1016/S0167-577X(97)00214-0

Mottard, P., & St-Amant, Y. (2009). Analysis of flexural hinge orientation for amplified piezo-driven actuators. *Smart Materials and Structures, 18*, 035005. doi:10.1088/0964-1726/18/3/035005

Moure, A., Izquierdo Rodríguez, M. A., Rueda, S. H., Gonzalo, A., Rubio-Marcos, F., Cuadros, D. U., . . . Fernández, J. F. (2016). Feasible integration in asphalt of piezoelectric cymbals for vibration energy harvesting. *Energy Conversion and Management, 112*, 246-253. doi:https://doi.org/10.1016/j.enconman.2016.01.030

Mouser Electronics. (2020). Advanced Linear Devices EH300A. Retrieved from https://my.mouser.com/ProductDetail/Advanced-Linear-Devices/EH300A?qs=NoieiqYAh1BN72EyvUOqOw%3D%3D

Ottman, G. K., Hofmann, H. F., & Lesieutre, G. A. (2003). Optimized piezoelectric energy harvesting circuit using step-down converter in discontinuous conduction mode. *IEEE Transactions on Power Electronics, 18*(2), 696-703. doi:10.1109/TPEL.2003.809379

Ouyang, P., Zhang, W., & Gupta, M. (2005). *Design of a New Compliant Mechanical Amplifier*.

Palosaari, J., Leinonen, M., Hannu, J., Juuti, J., & Jantunen, H. (2012). Energy harvesting with a cymbal type piezoelectric transducer from low frequency compression. *Journal of Electroceramics, 28*(4), 214-219. doi:10.1007/s10832-012-9713-8

Purviance, T., Wickler, S., Clayson, K., Barnes, T., & Mo, C. (2013). *Development of low-profile piezoelectric energy harvester for high load application.* Paper presented at the 2013 1st IEEE Conference on Technologies for Sustainability (SusTech).

Qi, K.-Q., Xiang, Y., Fang, C., Zhang, Y., & Yu, C.-s. (2015). Analysis of the displacement amplification ratio of bridge-type mechanism. *Mechanism and Machine Theory, 87*. doi:10.1016/j.mechmachtheory.2014.12.013

Qian, F., Xu, T.-B., & Zuo, L. (2019). Piezoelectric energy harvesting from human walking using a two-stage amplification mechanism. *Energy, 189*, 116140. doi:10.1016/j.energy.2019.116140

Qian, F., Xu, T. B., & Zuo, L. (2018). Design, optimization, modeling and testing of a piezoelectric footwear energy harvester. *Energy Conversion and Management, 171*, 1352-1364. doi:10.1016/j.enconman.2018.06.069

Ren, B., Or, S. W., Zhao, X., & Luo, H. (2010). Energy harvesting using a modified rectangular cymbal transducer based on 0.71Pb(Mg1/3Nb2/3)O3–0.29PbTiO3 single crystal. *Journal of Applied Physics, 107*(3), 034501. doi:10.1063/1.3296156

Roundy, S., Leland, E. S., Baker, J., Carleton, E., Reilly, E., Lai, E., . . . Sundararajan, V. (2005). Improving power output for vibration-based energy scavengers. *IEEE Pervasive Computing, 4*(1), 28-36. doi:10.1109/MPRV.2005.14

Roundy, S., & Wright, P. K. (2004). A piezoelectric vibration based generator for wireless electronics. *Smart Materials and Structures, 13*(5), 1131-1142. doi:10.1088/0964-1726/13/5/018

Salazar, R., Serrano, M., & Abdelkefi, A. (2020). Fatigue in piezoelectric ceramic vibrational energy harvesting: A review. *Applied Energy, 270*, 115161. doi:https://doi.org/10.1016/j.apenergy.2020.115161

Sezer, N., & Koç, M. (2021). A comprehensive review on the state-of-the-art of piezoelectric energy harvesting. *Nano Energy, 80*, 105567. doi:https://doi.org/10.1016/j.nanoen.2020.105567

Shafer, M., & Garcia, E. (2013). The Power and Efficiency Limits of Piezoelectric Energy Harvesting. *Journal of Vibration and Acoustics, 136*, 021007. doi:10.1115/1.4025996

Shao, S. B., Xu, M. L., Chen, J., & Feng, B. (2014). Optimal design of the large stroke piezoelectric actuator using rhombic mechanism.

Shenck, N. S., & Paradiso, J. A. (2001). Energy scavenging with shoe-mounted piezoelectrics. *IEEE Micro, 21*(3), 30-42. doi:10.1109/40.928763

Shixin, Y. L., & Li, Q. (2001). DESIGN AND STUDY OF A MOONIE PZT MICROACTUATOR SLIDER DRIVEN DEVICE FOR HARD DISK DRIVES. *ITE Technical Report, 25.69*, 81-86. doi:10.11485/itetr.25.69.0_81

Siddique, A. R. M., Mahmud, S., & Heyst, B. V. (2015). A comprehensive review on vibration based micro power generators using electromagnetic and piezoelectric transducer mechanisms. *Energy Conversion and Management, 106*, 728-747. doi:https://doi.org/10.1016/j.enconman.2015.09.071

Sosnicki, O., Lhermet, N., & Claeyssen, F. (2006). *Vibration energy harvesting in aircraft using piezoelectric actuators*. Paper presented at the 10th international conference on new actuators, Bremen, Germany.

SparkFun Electronics. (2020). SparkFun Energy Harvester Breakout - LTC3588. Retrieved from https://www.sparkfun.com/products/9946

Sun, S., & Tse, P. W. (2019). Modeling of a horizontal asymmetric U-shaped vibration-based piezoelectric energy harvester (U-VPEH). *Mechanical Systems and Signal Processing, 114*, 467-485. doi:https://doi.org/10.1016/j.ymssp.2018.05.029

Tayahi, M. B., Johnson, B., Holtzman, M., & Cadet, G. (2005, 7-9 April 2005). *Piezoelectric materials for powering remote sensors.* Paper presented at the PCCC 2005. 24th IEEE International Performance, Computing, and Communications Conference, 2005.

Tolliver, L., Jiang, X., & Xu, T.-B. (2013). *Piezoelectric Actuators With Active and Passive Frames* (Vol. 1).

Tolliver, L., Xu, T.-B., & Jiang, X. (2013). Finite element analysis of the piezoelectric stacked-HYBATS transducer. *Smart Materials and Structures, 22*(3), 035015. doi:10.1088/0964-1726/22/3/035015

Tufekcioglu, E., & Dogan, A. (2014). A flextensional piezo-composite structure for energy harvesting applications. *Sensors and Actuators A: Physical, 216*, 355-363.

Ueda, J., Schultz, J. A., & Asada, H. H. (2017). 1 - Structure of cellular actuators. In J. Ueda, J. A. Schultz, & H. H. Asada (Eds.), *Cellular Actuators* (pp. 1-44): Butterworth-Heinemann.

Umeda, M., Nakamura, K., & Ueha, S. (1996). Analysis of the transformation of mechanical impact energy to electric energy using piezoelectric vibrator. *Japanese Journal of Applied Physics, 35*(5S), 3267.

Vázquez-Rodríguez, M., Jiménez, F. J., Pardo, L., Ochoa, P., González, A. M., & de Frutos, J. (2019). A New Prospect in Road Traffic Energy Harvesting Using Lead-Free Piezoceramics. *Materials, 12*(22), 3725.

Wang, L., Chen, S., Zhou, W., Xu, T.-B., & Zuo, L. (2016). Piezoelectric vibration energy harvester with two-stage force amplification. *Journal of Intelligent Material Systems and Structures, 28*(9), 1175-1187. doi:10.1177/1045389X16667551

Wang, X., & Shi, Z. (2017). Double piezoelectric energy harvesting cell: modeling and experimental verification. *Smart Materials and Structures, 26*(6), 065002. doi:10.1088/1361-665x/aa6cf9

Wang, X., Shi, Z., Wang, J., & Xiang, H. (2016). A stack-based flex-compressive piezoelectric energy harvesting cell for large quasi-static loads. *Smart Materials and Structures, 25*(5), 055005. doi:10.1088/0964-1726/25/5/055005

Wang, Y., Chen, W., & Guzman, P. (2016). Piezoelectric stack energy harvesting with a force amplification frame: Modeling and experiment. *Journal of Intelligent Material Systems and Structures, 27*(17), 2324-2332. doi:10.1177/1045389x16629568

Wei, H., Shirinzadeh, B., Li, W., Clark, L., Pinskier, J., & Wang, Y. (2017). *Development of Piezo-Driven Compliant Bridge Mechanisms: General Analytical Equations and Optimization of Displacement Amplification* (Vol. 8).

Wen, S., & Xu, Q. (2017, 19-21 Nov. 2017). *Design of a two-stage force amplification frame for piezoelectric energy harvesting.* Paper presented at the 2017 IEEE International Conference on Cybernetics and Intelligent Systems (CIS) and IEEE Conference on Robotics, Automation and Mechatronics (RAM).

Wen, S., & Xu, Q. (2019). Design of a Novel Piezoelectric Energy Harvester Based on Integrated Multistage Force Amplification Frame. *IEEE/ASME Transactions on Mechatronics, 24*(3), 1228-1237. doi:10.1109/TMECH.2019.2906999

Wen, S., Xu, Q., & Zi, B. (2018). Design of a New Piezoelectric Energy Harvester Based on Compound Two-Stage Force Amplification Frame. *IEEE Sensors Journal, 18*(10), 3989-4000. doi:10.1109/JSEN.2018.2820221

Wu, J., Chen, X., Chu, Z., Shi, W., Yu, Y., & Dong, S. (2016). A barbell-shaped high-temperature piezoelectric vibration energy harvester based on BiScO3-PbTiO3 ceramic. *Applied Physics Letters, 109*(17), 173901. doi:10.1063/1.4966125

Wu, L., Chure, M.-C., Wu, K.-K., & Tung, C.-C. (2014). Voltage Generated Characteristics of Piezoelectric Ceramics Cymbal Transducer. *Journal of*

*Materials Science and Chemical Engineering, 02*, 32-37. doi:10.4236/msce.2014.210005

Wu, N., Bao, B., & Wang, Q. (2021). Review on engineering structural designs for efficient piezoelectric energy harvesting to obtain high power output. *Engineering Structures, 235*, 112068. doi:https://doi.org/10.1016/j.engstruct.2021.112068

Wu, Z., & Xu, Q. (2019). Design and testing of a novel bidirectional energy harvester with single piezoelectric stack. *Mechanical Systems and Signal Processing, 122*, 139-151. doi:https://doi.org/10.1016/j.ymssp.2018.12.026

Xu, C., Ren, B., Di, W., Liang, Z., Jiao, J., Li, L., . . . Wang, D. (2012). Cantilever driving low frequency piezoelectric energy harvester using single crystal material 0.71Pb(Mg1/3Nb2/3)O3-0.29PbTiO3. *Applied Physics Letters, 101*(3), 033502. doi:10.1063/1.4737170

Xu, C., Ren, B., Liang, Z., Chen, J., Zhang, H., Yue, Q., . . . Luo, H. (2012). Nonlinear output properties of cantilever driving low frequency piezoelectric energy harvester. *Applied Physics Letters, 101*(22), 223503.

Xu, Q., & Li, Y. (2011). Analytical modeling, optimization and testing of a compound bridge-type compliant displacement amplifier. *Mechanism and Machine Theory, 46*(2), 183-200. doi:https://doi.org/10.1016/j.mechmachtheory.2010.09.007

Xu, T.-B. (2016). Energy harvesting using piezoelectric materials in aerospace structures *Structural Health Monitoring (SHM) in Aerospace Structures* (pp. 175-212): Elsevier.

Xu, T.-B., Jiang, X., & Su, J. (2011). A piezoelectric multilayer-stacked hybrid actuation/transduction system. *Applied Physics Letters, 98*(24), 243503. doi:10.1063/1.3600057

Xu, T.-B., Jiang, X.,Su, J.,Rehrig, P.W.,Hackenberger, W.S.,. (2008). US Patent No. 7,446,459 B2.

Xu, T.-B., Siochi, E. J., Kang, J. H., Zuo, L., Zhou, W., Tang, X., & Jiang, X. (2011). *A piezoelectric PZT ceramic multilayer stack for energy harvesting under dynamic forces*. Paper presented at the ASME 2011 International Design Engineering Technical Conferences and Computers and Information in Engineering Conference.

Xu, T.-B., Siochi, E. J., Kang, J. H., Zuo, L., Zhou, W., Tang, X., & Jiang, X. (2013). Energy harvesting using a PZT ceramic multilayer stack. *Smart Materials and Structures, 22*(6), 065015. doi:10.1088/0964-1726/22/6/065015

Xu, T. B. (2016). 7 - Energy harvesting using piezoelectric materials in aerospace structures. In F.-G. Yuan (Ed.), *Structural Health Monitoring (SHM) in Aerospace Structures* (pp. 175-212): Woodhead Publishing.

Yang, Z., Erturk, A., & Zu, J. (2017). On the efficiency of piezoelectric energy harvesters. *Extreme Mechanics Letters, 15*, 26-37. doi:https://doi.org/10.1016/j.eml.2017.05.002

Yang, Z., Wang, Y. Q., Zuo, L., & Zu, J. (2017). Introducing arc-shaped piezoelectric elements into energy harvesters. *Energy Conversion and Management, 148*, 260-266. doi:https://doi.org/10.1016/j.enconman.2017.05.073

Yang, Z., Zhou, S., Zu, J., & Inman, D. (2018). High-performance piezoelectric energy harvesters and their applications. *Joule, 2*(4), 642-697.

Yang, Z., Zhu, Y., & Zu, J. (2015). Theoretical and experimental investigation of a nonlinear compressive-mode energy harvester with high power output under weak excitations. *Smart Materials and Structures, 24*, 025028. doi:10.1088/0964-1726/24/2/025028

Yang, Z., & Zu, J. (2014). High-efficiency compressive-mode energy harvester enhanced by a multi-stage force amplification mechanism. *Energy Conversion and Management, 88*, 829-833. doi:https://doi.org/10.1016/j.enconman.2014.09.026

Yang, Z., Zu, J., Luo, J., & Peng, Y. (2016). Modeling and parametric study of a force-amplified compressive-mode piezoelectric energy harvester. *Journal of Intelligent Material Systems and Structures, 28*(3), 357-366. doi:10.1177/1045389X16642536

Yuan, J.-b., Shan, X.-b., Xie, T., & Chen, W.-s. (2009). Energy harvesting with a slotted-cymbal transducer. *Journal of Zhejiang University-SCIENCE A, 10*(8), 1187-1190.

Yuan, J., Shan, X., Xie, T., & Chen, W. (2010). Modeling and Improvement of a Cymbal Transducer in Energy Harvesting. *Journal of Intelligent Material Systems and Structures - J INTEL MAT SYST STRUCT, 21*, 765-771. doi:10.1177/1045389X10366318

Zhao, H., Ling, J., & Fu, P. (2013). A Review of Harvesting Green Energy from Road. *Advanced Materials Research, 723*, 559-566. doi:10.4028/www.scientific.net/AMR.723.559

Zhao, H., Ling, J., & Yu, J. (2012). A comparative analysis of piezoelectric transducers for harvesting energy from asphalt pavement. *Journal of the Ceramic Society of Japan, 120*, 317-323. doi:10.2109/jcersj2.120.317

Zhao, H., Qin, L., & Ling, J. (2015). Test and Analysis of Bridge Transducers for Harvesting Energy from Asphalt Pavement. *International Journal of Transportation Science and Technology, 4*(1), 17-28. doi:https://doi.org/10.1260/2046-0430.4.1.17

Zhao, H., Qin, L., & Ling, J. (2018). Synergistic performance of piezoelectric transducers and asphalt pavement. *International Journal of Pavement Research and Technology, 11*(4), 381-387. doi:https://doi.org/10.1016/j.ijprt.2017.09.008

Zhao, H., Yu, J., & Ling, J. (2010). Finite element analysis of Cymbal piezoelectric transducers for harvesting energy from asphalt pavement. *Journal of the Ceramic Society of Japan, 118*, 909-915. doi:10.2109/jcersj2.118.909

Zhao, J., Zheng, X., Zhou, L., Zhang, Y., Sun, J., Dong, W., . . . Peng, S. (2012). Investigation of ad15mode PZT-51 piezoelectric energy harvester with a series connection structure. *Smart Materials and Structures, 21*(10), 105006. doi:10.1088/0964-1726/21/10/105006

Zhou, H., & Henson, B. (2007). *Analysis of a diamond-shaped mechanical amplifier for a piezo actuator* (Vol. 32).

Zhou, S., Cao, J., Erturk, A., & Lin, J. (2013). Enhanced broadband piezoelectric energy harvesting using rotatable magnets. *Applied Physics Letters, 102*(17), 173901. doi:10.1063/1.4803445

Zhou, S., Chen, W., Malakooti, M., Cao, J., & Inman, D. (2016). Design and modeling of a flexible longitudinal zigzag structure for enhanced vibration energy harvesting. *Journal of Intelligent Material Systems and Structures, 28*. doi:10.1177/1045389X16645862

Zhou, W., & Zuo, L. (2013). *A Novel Piezoelectric Multilayer Stack Energy Harvester With Force Amplification* (Vol. 8).

Zhou, W. L., Zuo, L., & Asme. (2014). *A NOVEL PIEZOELECTRIC MULTILAYER STACK ENERGY HARVESTER WITH FORCE AMPLIFICATION*.

Zou, H.-X., Zhang, W.-M., Wei, K.-X., Li, W.-B., Peng, Z.-K., & Meng, G. (2016). A Compressive-Mode Wideband Vibration Energy Harvester Using a Combination of Bistable and Flextensional Mechanisms. *Journal of Applied Mechanics, 83*(12). doi:10.1115/1.4034563

Zou, H.-X., Zhang, W., Li, W.-B., Hu, K.-M., Wei, K.-x., Peng, Z., & Meng, G. (2017). *A broadband compressive-mode vibration energy harvester enhanced by magnetic force intervention approach* (Vol. 110).